Étude du retournement optique dépendant de l'hélicité dans des couches minces magnétiques

Charles-Henri Lambert

PhD Thesis

Université de Lorraine

Ecole doctorale EMMA

PhD in Physics

By :

Charles-Henri Lambert

Subject of the report :

All-Optical Helicity dependent switching effect in magnetic thin films

Committee :

Martin Aeschlimann, Professeur
Manfred Albrecht, Professeur
Eric Beaurepaire, Directeur de Recherche, Rapporteur
Eric Fullerton, Professeur
Bert Koopmans, Professeur
Jan Luning, Professeur, Rapporteur
Stéphane Mangin, Professeur, Directeur de Thèse

Institut Jean Lamour
UMR CNRS 7198 – Université de Lorraine, Nancy
Département de Physique de la Matière et des Matériaux
Equipe de Nanomagnétisme et Electronique de Spin

Contents

Introduction

The possibilities of manipulating magnetization without applied magnetic fields have attracted growing attention over the past fifteen years. Examples include the demonstration of spin-transfer-torque switching[103], the emerging potential of electric fields[150] to manipulate magnetic devices and magnetization switching using femto- or pico-second pulsed lasers[186,71,4]. The dynamic response of magnetic order to ultrafast external excitation is indeed a fascinating issue of modern physics[114,4]. Optical probing at the femtosecond timescale allows the investigation of ultrafast magnetization dynamics, including fundamental interactions between spins, electrons, and lattice degrees of freedom far from equilibrium[114,11,30,135]. The use of femtosecond laser pulses for magnetization switching is particularly interesting because such pulses are 1,000-10,000 times shorter than the shortest magnetic field pulses[199] or spin-polarized current[14] pulses needed to induce reversal. It further has the potential for new technologies such as heat-assisted magnetic recording (HAMR)[119,192]because of the low-power manipulation of magnetization, preferably at ultrashort timescales, that has become a fundamental challenge for future magnetic memory and data storage technologies. An important outcome of ultrafast dynamics studies of magnetic systems was the demonstration that circularly polarized light can directly switch magnetic domains in ferrimagnetic GdFeCo alloy films without an applied magnetic field[186]. This deterministic magnetization switching using circularly polarized laser pulses is referred to as all-optical helicity-dependent switching (AO-HDS). In the case of optical means, this process seems highly energy efficient; an energy lower than 10 fJ is expected to be sufficient to switch a 20×20 nm^2 area of magnetic material[176]. However, at the beginning of my PhD, observations of AO-HDS were only reported for a narrow composition range of the following amorphous RE-TM ferrimagnetic alloy films of GdFeCo[187], TbCo[71] and TbFe[79]. In all those cases, AO-HDS was observed for ferrimagnetic systems with two distinct sublattices that are antiferromagnetically exchange-coupled. Models for AO-HDS were based on the existence of an effective field created by the circular polarized light via the inverse Faraday effect[42,109] or by the transfer of angular momentum from the light to the magnetic system[187]. Some recent models focused on the formation of a transient ferromagnetic state[165] due to different demagnetization times for RE and TM sublattices where the light's helicity plays a secondary role[152,139,74]. There was also emerging evidence that laser-induced superdiffusive spin currents can flow in heterogeneous systems[74,200,201,9,131], potentially contributing to the AO-HDS process[74]. The goal of my PhD was to determine which material could exhibit AO-HDS. This material study should help the understanding of the fundamental mechanism of AO-HDS. Indeed an open question is whether AO-HDS is specific to a subset of ferrimagnetic materials or can be applied to ferromagnetic materials. Furthermore, can optical pulses also control technologically important high-anisotropy granular or patterned materials that are anticipated for future high-density magnetic recording[211] ?

This manuscript is divided into three parts. The first part consists in a state of the art both experimental and theoretical about magnetism leading to the description of all-optical helicity dependent

switching and the parameters currently debated in the understanding of the different existing models. The second part presents the samples studied during this thesis and the experimental setup used to measure their properties. An emphasize is put on the possible conclusions and particular difficulties than are inherent to our approach. Finally the third part is focusing on the optical observations done on the many different systems studied during this thesis. A model highlighting the role of temperature and demagnetizing energy is presented and is in very good agreement with the experiment data.

Chapter 1

Manipulation of the magnetization

1.1 Magnetization Dynamics

The aim of this section is to briefly remind the origin of magnetism and to describe the different interactions present in a magnetic material. The different way of manipulating magnetization are described and the influence of temperature is presented.

1.1.1 Origin of magnetism

A classical description is to use the Bohr model where the electrons are rotating around the nucleus at a given distance. A surface $\mathbf{S} = (\pi R^2)\,\mathbf{n}$ ($\mathbf{n}$ the unit vector perpendicular to the surface) can be thus defined as shown in Fig. 1.1.

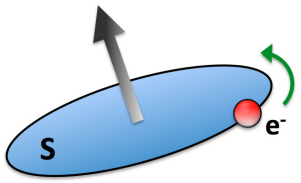

Figure 1.1: Trajectory of an electron around the nucleus.

This circulation of charge gives rise to a current loop I and can be considered as a magnetic dipole $\mathbf{M} = I\,\mathbf{S}$. Because of its mass, the electron shows an orbital angular momentum $\mathbf{L} = \mathbf{r} \times \mathbf{p}$, with $\mathbf{r}$ the position vector and $\mathbf{p} = m\mathbf{v}$ the linear momentum of the particle. This magnetic momentum is proportional to the angular moment such as $\mathbf{M} = \gamma\,\mathbf{L}$ where γ is the gyromagnetic constant. In order to understand magnetism a quantum approach is needed. In that case along with that orbital angular momentum, the existence of an intrinsic angular momentum for the electrons called the spin angular momentum has to be taken into account and was confirmed in 1922 by the Stern-Gerlach experiment. This momentum is quantized and can be written as:

$$\mathcal{M}_{sp} = -g_s \mu_B s \tag{1.1}$$

with $g_s \simeq 2$ the Landé factor of the electron spin, $\mu_B = \frac{\hbar e}{2m}$ is the Bohr magneton and $s = \pm\frac{1}{2}$ is the quantic spin number.

Besides, there is an interaction between these two contributions (orbital and spin angular momentum) called the spin-orbit coupling so that the total magnetic moment of an atom is calculated thanks

to the Hund rules. These rules imply that only the atoms with incomplete atomic shells are magnetic. This rules work well for isolated atoms, but the interactions with others atoms in solids modify the electronic structure. The few remaining solids with incomplete shell structure and that are magnetic can be classified in two main categories: the rare-earth ($4f$ shell incomplete) and the transition metals ($3d$ shell incomplete).

Considering spin and orbital angular momentum the magnetic moment held by one atom can be calculated, however in a material these individual contributions will add up and cancel out depending on their relative orientations. Therefore, it is usually easier to use the global magnetization $\mathbf{M} = \frac{1}{V}\sum_i \mathcal{M}_i$ considering the sum over all the atomic magnetic moments $\mathcal{M}_i$ of the system and V the volume of the magnetic material.

1.1.2 Magnetic interactions

To study the magnetic configuration in magnetic materials, it is necessary to understand the interactions that contribute to the magnetization orientation. These combined interactions determine in the end the amplitude, the orientation and the dynamic of the magnetization. All of them involve intrinsic parameters that are used for micromagnetic simulations for example. Furthermore for simplicity each interaction is model by an effective field that will then add up to determine the magnetization dynamics.

$$\mathbf{H_{eff}} = \sum_i \mathbf{H_i} \tag{1.2}$$

Exchange interaction

The exchange interaction originates from the Pauli exclusion principle and Coulomb interaction. Because of it, the energy between two interacting electrons is reduced or increased depending on the relative orientation of their spins. We can associate a particular exchange energy to this effect between two spins $\mathbf{S_1}$ and $\mathbf{S_2}$:

$$E_{ex} = J\,\mathbf{S_1}\cdot\mathbf{S_2} \tag{1.3}$$

This can then be generalized to the interactions between two magnetic moments :

$$E_{ex} = -\mu_0 A_{ex}\mathcal{M}_i\cdot\mathcal{M}_j \tag{1.4}$$

where $\mathcal{M}_i$,$\mathcal{M}_j$ represent the total magnetic moments held by two interacting atoms, and A_{ex} characterizes the nature of the exchange interaction and the intensity of the coupling between adjacent moments.

Regarding the sign of A_{ex}, two adjacent atomic magnetic moments will tend to be parallel — if $A_{ex} > 0$ as it is the case in ferromagnetic materials like iron, cobalt or Nickel — or antiparallel ($A_{ex} < 0$) as in antiferromagnetic materials like chromium. The only condition to observe such short-range order is to be below a critical temperature called Curie Temperature for ferromagnets and Néel Temperature for antiferromagnets. If the temperature is higher than that value, the magnetic moments are randomly oriented because of the thermal fluctuations and no particular macroscopic magnetization can be measured, the material is paramagnetic (see figure 1.2).

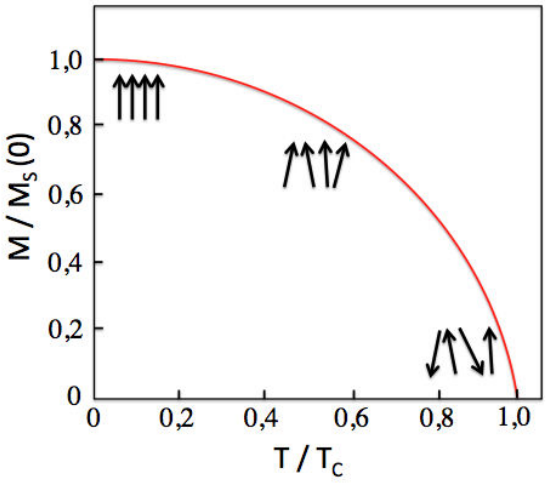

Figure 1.2: Magnetization versus temperature for a typical ferromagnetic material. T_C indicates the Curie temperature.

Zeeman Interaction

The Zeeman interaction describes the action of an external magnetic field applied on magnetic moments. The magnetization **M** of the material tends to minimize the Zeeman energy:

$$E_{zee} = -\mu_0 V \, \mathbf{M} \cdot \mathbf{H} \tag{1.5}$$

with V the volume of the magnetic material, **H** the external magnetic field.

As we can see in the expression 1.5, the energy is minimal when the magnetization is aligned with the external field. This interaction will then tend to drive the magnetization along the direction of the magnetic field.

Dipolar interaction

Contrary to the exchange interaction, the dipolar interaction is a long-range effect that occurs when we consider the dipolar magnetic field $\mathbf{H_{dip}}$ created by a magnetic moment **M** at a distance **r** from the dipole is given by the expression $\mathbf{H}_{dip} = \frac{1}{4\pi}[\frac{(\mathbf{M}-r)\cdot r}{r^5} - \frac{\mathbf{M}}{r^3}]$. The total dipolar field will be given by the sum of all individual dipolar fields. If we consider a small volume of magnetic material which as a magnetization **M** the dipolar energy will be given by :

$$E_{dip} = -\mu_0 V \, \mathbf{M} \cdot \mathbf{H}_{dip} \tag{1.6}$$

where V is the volume of the magnet.

This dipolar interaction shows two opposite contributions in order to minimize the energy E_{dip} : if the direction **r** is aligned with the direction of the magnetization of the first magnet, the second magnet will prefer to be aligned with the first one; and if the direction **r** is perpendicular to the direction of the magnetization of the first magnet, the second magnetization will prefer to be antiparallel (see Fig. 1.3).

Considering the influence of all the dipoles in a bulk material, it is often opposite to the direction of the global magnetization of the material. This interaction then tends to lower the magnetization and creates a local distribution of magnetic moments : for this reason it's also called the demagnetizing

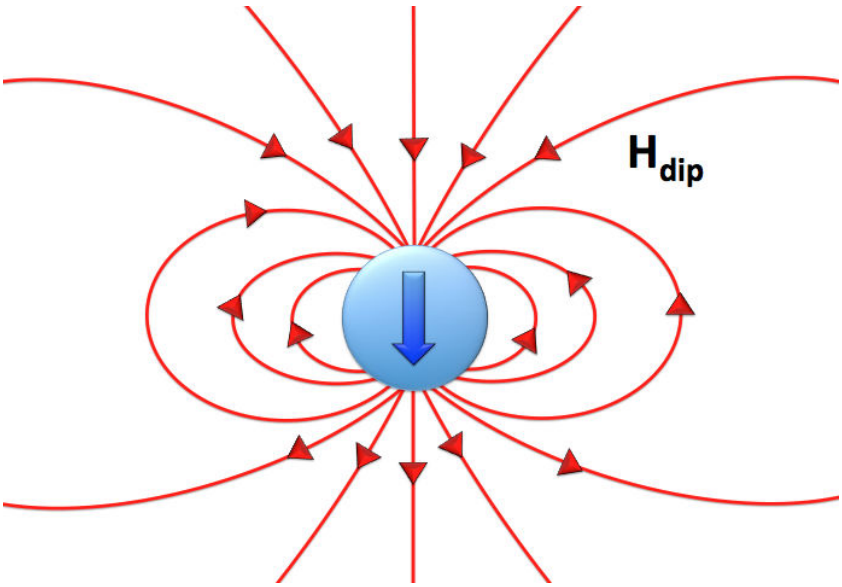

Figure 1.3: Dipolar field created by a magnetic material.

field. This field depends on the size and geometry of the sample and induces preferential orientations for the magnetization, this phenomenon is described as the shape anisotropy[47].

Shape anisotropy

The magnetization orientation tends to be sensitive to the shape of the object containing the magnetic material. This effect can be described considering magnetic charges left at the surfaces of the material that create an additional internal field called the demagnetization field H_{dem}. In general this field is neither uniform in direction nor in value inside the object. However for certain particular geometries (see fig 1.4) such as the ellipsoid when the magnetization is considered uniform some simplifications are possible. In this particular case, the mean demagnetization field can be calculated and has the following expression[38] :

$$\mathbf{H_{dem}} = -4\pi \begin{pmatrix} N_{xx} & 0 & 0 \\ 0 & N_{yy} & 0 \\ 0 & 0 & N_{zz} \end{pmatrix} \mathbf{M_S} \tag{1.7}$$

where $\mathbf{M_S}$ is the magnetization vector of the material and N_{xx}, N_{yy} and N_{zz} are the shape parameters of the mean demagnetization field that always verify the relation $N_{xx} + N_{yy} + N_{zz} = 1$. Depending on the shape of the object (see fig 1.4) they change and thus be responsible of the final orientation of H_{dem}.

The associated demagnetization energy E_{dem} for the system with a general ellipsoid shape will be :

$$E_{dem} = -\frac{1}{2}\mathbf{M_S} \cdot \mathbf{H_{dem}} = 2\pi(N_{xx}{M_x}^2 + N_{yy}{M_y}^2 + N_{zz}{M_z}^2) \tag{1.8}$$

where the M_i coefficients are the projection of $\mathbf{M_S}$ along the coordinate axis.

If this relation is rather simple, the situation can be much more complicated if a domain structure shows up in the object. In this case the determination of the N_{ii} coefficient becomes very hard and the magnetization response of the sample to a magnetic field becomes more complex. However the possibility to modulate the demagnetization field just by modifying the shape of an object is extremely

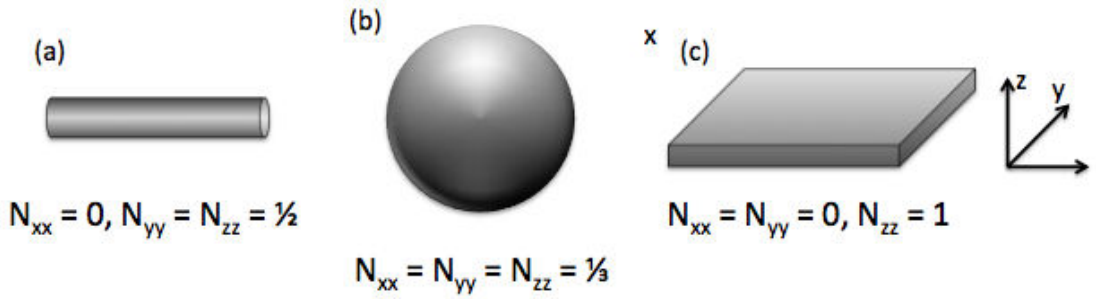

Figure 1.4: Shape parameters for (a) a long cylindrical rod, (b) a sphere, (c) a flat plate (equivalent to a thin film).

useful and will be developed in the following parts describing the kinds of systems used in this thesis.

In our case we will only be in the case of a thin film with a perpendicular magnetization, so the surface charges will only be present at the two surfaces of our material. The demagnetizing factors become $N_{xx} = N_{yy} = 0$ and it is easy to calculate the magnetostatic energy from Eq. 1.9 :

$$E_{dem} = 2\pi M_S^2 \tag{1.9}$$

where M_S is the projection of the magnetization along the preferential z axis.

Magnetocrystalline anisotropy

Because of spin-orbit coupling and crystal field, the crystalline structure of the magnetic atoms in a solid has an influence on the orientation of the magnetization. As the position of the electronic orbitals are constrained by the crystalline structure, the orbital magnetic moments highlight some preferential direction in the material : this is the magnetocrystalline anisotropy. This effect is related to a particular energy landscape for magnetization with axis where the magnetization prefers to lie (called easy axis) and some others that will be difficult to align with (hard axis) because of the relative high energy involved in this orientation.

Cubic anisotropy

For particles with low saturation magnetization the crystal structure usually dominates the magnetic energy. In such case, the crystallographic directions are creating so-called easy directions for the magnetization via the local minimum of magnetocrystalline energy. For crystals with a cubic structure the magnetocrystalline anisotropy energy E_{cub} is given by:

$$E_{cub} = V(K_1({\alpha_1}^2{\alpha_2}^2 + {\alpha_2}^2{\alpha_3}^2 + {\alpha_3}^2{\alpha_1}^2) + K_2({\alpha_1}^2{\alpha_2}^2{\alpha_3}^2) + \dots) \tag{1.10}$$

where α_i are the direction cosines with the crystallographic axes [100, 010, 001], and K_1 and K_2 are first and second order empirically determined anisotropy constants and V the volume of the particle. At room temperature, the second order term and other higher order terms can be mostly neglected, but they may become important at low temperature.

Figure 1.5 illustrates some of the different configurations allowed by the equation 1.10. In the case of fig 1.5 b) for example, the highest energy bulges are in directions perpendicular to the cubic faces ([001, 010, 100]) while the lowest energy dimples are along the body diagonals ([111]), it is typically

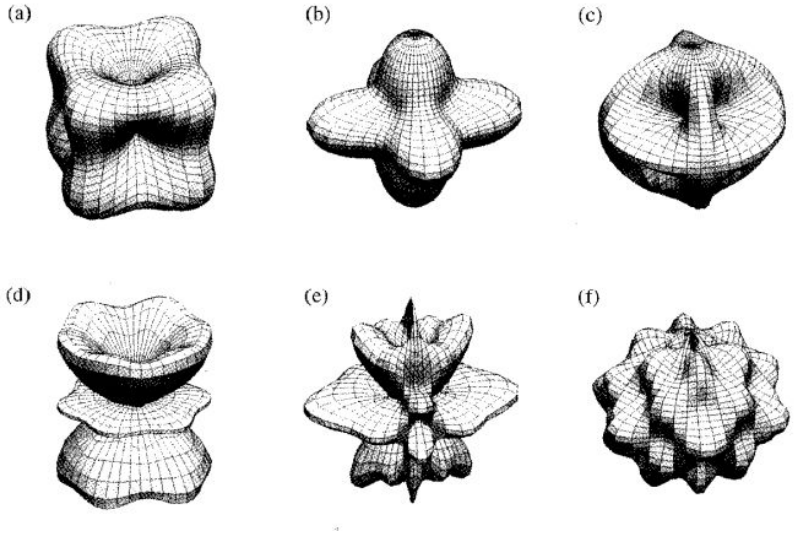

Figure 1.5: Energy surfaces for higher-order anisotropies: (a-c) cubic magnetic anisotropy (d-f) magnets with low symmetry. Figure extracted from *Skomski*[180].

the case for a bulk Nickel sample where $K_1 < 0$ and $K_2 = 0$. The figure 1.5 a) would be valid for Iron where $K_1 > 0$ and $K_2 = 0$.

A consequence of this magnetocrystalline anisotropy energy is the existence of energy barriers between easy magnetization directions. In order to go from one deep to another the magnetization has to go along the hard axis and thus requires an additional energy to reach this new state of magnetization.

Uniaxial anisotropy

Cubic symmetry is just one of many types of crystal symmetries. One other very important form is the uniaxial symmetry which can arise from crystal shape or structure. The associated energy for uniaxial magnetic anisotropy is:

$$E_{ani} = V(K_{u_1} \sin^2 \theta + K_{u_2} \sin^4 \theta + \dots) \tag{1.11}$$

where K_{u_1} and K_{u_2} are the first and second order anisotropy constant as in equation 1.11, V the volume of the magnetization.

In this equation if we neglect the second order term there is only two possibilities illustrated in fig 1.6 b) and c) : either an easy axis for the magnetization if $K_{u_1} < 0$ or an easy plane if $K_{u_1} > 0$ which means that the magnetization is constrained to lie perpendicular to the axis of symmetry. One has to notice that the K coefficient used in the cubic or uniaxial anisotropy are not fixed for each element but they vary with the material structure and shape.

Uniaxial anisotropy is often use because of its simplicity to foresee and simulate the magnetic behavior of materials. Furthermore in those kind of system there is a direct competition between the volume and surface anisotropy related to the demagnetizing and shape anisotropy.

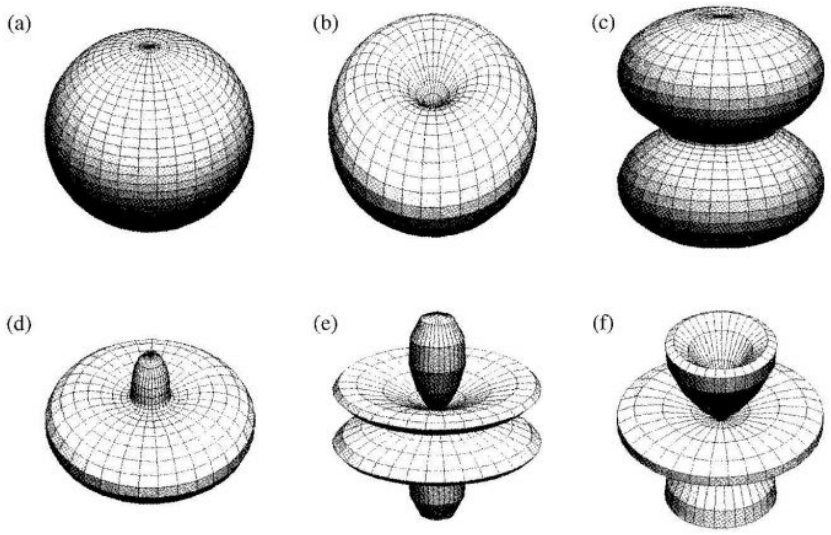

Figure 1.6: Uniaxial anisotropy-energy landscapes : (a) isotropic, (b) easy axis, (c) easy plane, (d) easy cone, and (e-f) sixth-order landscapes. Figure extracted from *Skomski*[180].

Effective Magnetic Field Representation

Finally, the effects of this interactions are always competing to orient the magnetization of a magnetic material. The final direction of spins will only be determined by minimizing all this contributions. A convenient way to represent and to introduce these effects in the equation of motion of the magnetization is to remember that they all can be described as the action of a magnetic field. As a result, everything behaves just as if the magnetization evolves in an effective magnetic field given by :

$$\mathbf{H}_{eff} = \mathbf{H} + \mathbf{H}_{dip} + \mathbf{H}_{dem} + \mathbf{H}_{ani} + \dots . \tag{1.12}$$

1.1.3 Competition between interactions

Perpendicularly magnetized thin films

Bulk materials usually show an in-plane magnetization but the out-of-plane component increases as the dimensions are shrunk down. The most important aspect of downsizing the sample is the evolution of the surface over volume ratio that can become extremely high in the nanoscale domain. So surface and interface effects become larger and bring some new phenomena.

In a ferromagnet two contributions are responsible of the global orientation of the magnetization: the bulk and the surface anisotropies. While the bulk anisotropy is directly fixed from the orientation of the atomic orbitals in the material, the second one varies with the geometry of the sample. Indeed the surface anisotropy is linked only to the atomic orbitals located at the interface (or surface). In fact Néel attributed this phenomenon to the symmetry breaking of the surface or interface[148]. In order to highlight the role of the two terms the following equation can be considered for numerous perpendicular systems:

$$K_{eff} = K_b + \frac{K_s}{t} - 2\pi M_s^2 \tag{1.13}$$

where K_{eff} is the perpendicular magnetic anisotropy, K_s and K_b respectively the intrinsic surface and bulk anisotropy term, t the thickness of the film and M_s the magnetization.

We can notice that the surface anisotropy term increases as the thickness of the thin film decreases and can become larger than the shape anisotropy created by the demagnetizing field[72]. In some materials, such as Fe/V systems grown and capped with MgO, this surface anisotropy is perpendicular and the balance between the two terms in the equation forces the magnetization to point out-of-plane for small thickness of iron[121] (see figure 1.8). In particular this perpendicular anisotropy is very sensitive to the quality of the sample and it requires a proper control of the surface roughness to guarantee the good orientation of the magnetization. This is confirmed by a study of the magnetic features of MBE-grown single-crystal MgO/V/Fe/MgO (001) and MgO/Cr/Fe/MgO (001) heterostructures done in our laboratory.

Shape Anisotropy in V/Fe/MgO systems

To reach this quality, the samples have be grown on single-crystal MgO (100) substrate using molecular beam epitaxy (MBE) with a base-pressure lower than 10^{-10} Torr. The V or Cr buffer layers are deposited at room temperature (RT) and then annealed at 600 °C. An Fe wedge was then grown on the V or Cr buffer layers and covered with a 6-monolayers (ML) (1.2nm) MgO(001) film. Fe was deposited at RT with no further annealing and capped with MgO also at room temperature. The epitaxial relationship, growth mode, number of deposited MLs, and surface flatness are controlled in situ using reflection high energy electron diffraction (RHEED). Figure 1.7 show RHEED intensity oscillations recorded during the growth of Fe on Cr and V, respectively. The oscillation period corresponds to 1 ML, which allows accurate control of t_{Fe} and demonstrates layer-by-layer growth and a low surface roughness. The RHEED patterns in the insets confirm the (001) crystalline order for the Cr and V buffer layers and Fe magnetic layers.

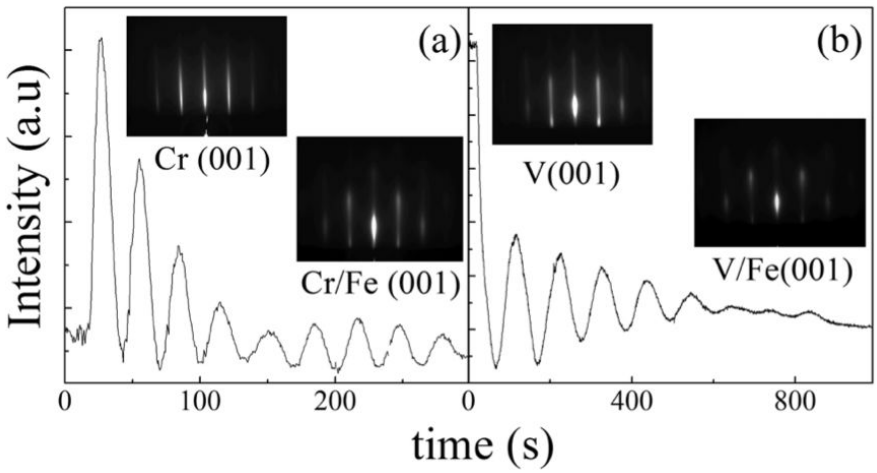

Figure 1.7: RHEED intensity oscillations recorded during the growth of Fe on Cr(001) (a) and V(001) (b), respectively. In inset, RHEED patterns of V and Cr (001) buffer layers are shown, as well as Cr/Fe(8 MLs) and V/Fe(8 MLs).

Magnetization and magnetic anisotropies were measured by different techniques including magneto-optic Kerr effect (MOKE), ferromagnetic resonance (FMR), and magnetometry for Fe thickness ranging from 5 to 12 monoatomic layers (MLs). Considering the contributions of the Fe magneto-crystalline and shape anisotropies, and the V-Fe, Cr-Fe and Fe-MgO interfaces anisotropies, we can quantify the Fe-MgO interface anisotropy and compare to existing experimental and theoretical results.

Figure 1.8a shows magnetization curves measured using a Quantum Design SQUID-VSM on both

V/Fe(5-7 MLs)/MgO and Cr/Fe(3-5 MLs)/MgO systems for both in-plane and out- of-plane applied magnetic fields. For the thinnest Fe layers, we observe square out-of-plane loops indicating a perpendicular magnetic anisotropy (PMA) for the system. For the V/Fe/MgO(001) wedge (Figs. 1.8a (a)-(c)), the preferential magnetization direction moves from out-of- plane to in-plane as Fe thickness increases from 5 to 7 MLs. In contrast for the Cr/Fe/MgO(001) wedge (Figs. 1.8a (d)-(f)), this transition occurs for 3-5 ML. Considering that the origin of the PMA in such thin Fe layers is thought to be primarily due to the Fe-MgO interface anisotropy, these results clearly show additional contributing factors.

The values of effective anisotropies K_{eff} extracted from SQUID-VSM, FMR, and MOKE experiments are plotted in Fig. 1.8b versus the active Fe thickness corrected from the dead layers at Fe/V interface. The unique linear variation confirms the good agreement between the results obtained from the different techniques. There are two contributions in Ks, one coming from the V-Fe or Cr-Fe interfaces, the other from the Fe-MgO one. Detailed analysis of magnetic properties (magnetization, effective anisotropy) and literature allows us to enlighten the origin of PMA in V/Fe/MgO(001) and Cr/Fe/MgO(001) epitaxial layers. As the V-Fe interface anisotropy is very small, this means that this Ks value comes from the Fe/ MgO interface. The Fe thickness limit for getting PMA is found to be different in both systems (below 6 MLs in V/Fe/ MgO and 4 MLs in Cr/Fe/MgO). This is explained by the occurrence of 2 MLs magnetic dead layers in Fe on V that does not exist on Cr. For a given Fe thickness, the shape anisotropy is thus smaller in V/Fe than in Cr/Fe whereas the Fe/MgO interface anisotropy is found to be similar for both systems. This study allows an accurate and robust determination of the Fe/MgO interface anisotropy $K_S = 1.0 \pm 0.1$ erg/ cm^2 (mJ/m^2) responsible for PMA.

PMA in multilayers

According to this conclusion it would be possible to observe perpendicular magnetization in very thin materials only. However an alternative exists to increase the volume perpendicularly magnetized: the multilayer systems. In those case two different materials — A and B — that have a perpendicular anisotropy at their interface are grown alternatively on a surface to create a bigger perpendicularly magnetized volume than it is individually possible. Each layer of A and B has to be thin enough for the perpendicular interface anisotropy of the bilayer A/B to balance its planar shape anisotropy. Each individual thickness of A and B will contribute to the global perpendicular magnetization and the global system can contain as many repetitions as desired.

The figure 1.9 sums up the idea of multilayer thin films that is already used in many laboratories. Not all materials appear perpendicular for small thickness but gathering of two transitions metals, such as [Co/Pd][29], [Co/Pt][26] or [Co/Ni][39] combinations, lead to perpendicular systems with a good control of the anisotropy value.

Domain formation in PMA systems

Up to now, we have consider that magnetization is uniform, however in this case this configuration generates a strong demagnetizing field (the field due to magnetic dipoles). In order to minimize its magnetostatic energy the magnetization orients in different directions. Typically, magnetic materials can be divided into many small regions with uniform magnetization, called magnetic domains and the region between two domains is named magnetic domain wall.

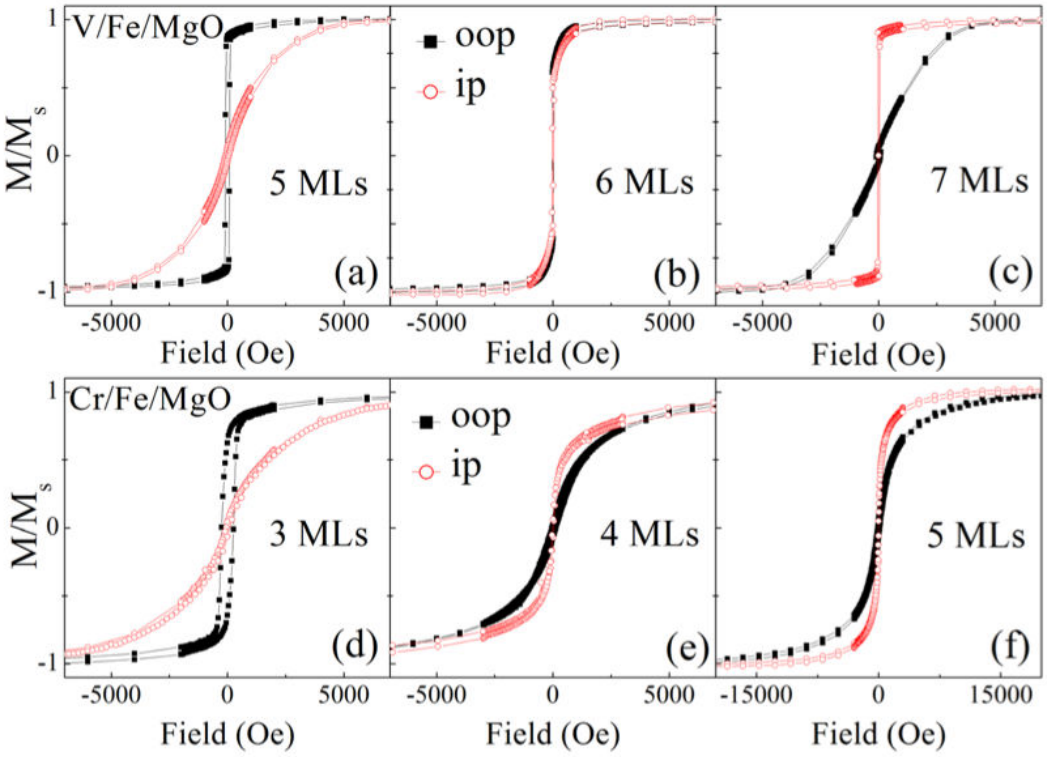

(a)

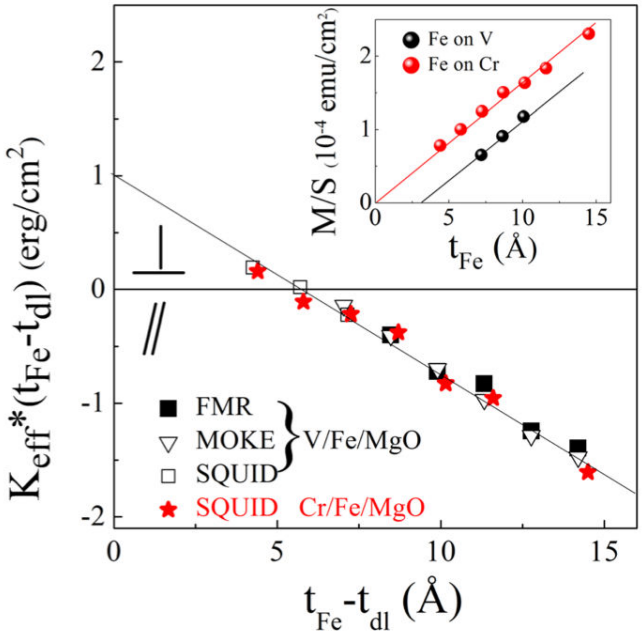

(b)

Figure 1.8: (top) Room temperature normalized magnetization as a function of magnetic field applied out-of-plane (OOP-black squares) and in the film plane (IP-red open circles), measured on $V/Fe/MgO$ sample with t_{Fe} set to (a) 5 MLs, (b) 6 MLs and (c) 7 MLs and on $Cr/Fe/MgO$ with t_{Fe} set to (d) 3 MLs, (e) 4 MLs and (f) 5 MLs. (bottom) Effective anisotropy constant K_{eff} times $t_{Fe} - t_{dl}$ as a function of $t_{Fe} - t_{dl}$ deduced from SQUID-VSM, FMR, and MOKE measurements at RT for both $V/Fe/MgO$ and $Cr/Fe/MgO$ systems. The line is a fit using Eq. 1.13. In inset are plotted the areal magnetization versus Fe thickness, showing that $t_{dl} = 0$ for Fe on Cr and $t_{dl} = 3$ Å for Fe on V. Figure extracted from *Lambert et al.*[121]

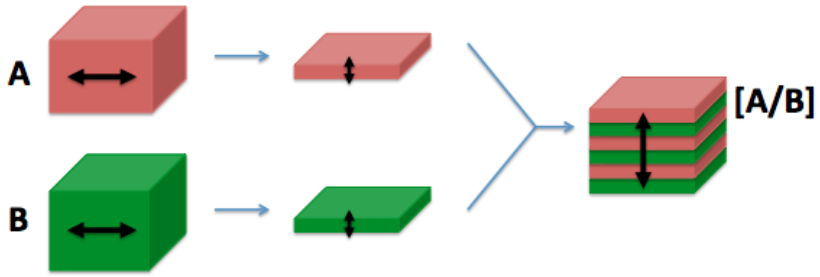

Figure 1.9: One of the process to obtain strong magnetization with out-of-plane orientation.

Magnetic domains exist in order to reduce the total energy of the system. A uniformly magnetized specimen as shown in figure 1.10 (a) is associated to a large magnetostatic energy. This is the result of the presence of magnetic charges at the surface of the specimen generating a demagnetizing field. Similarly a simple free magnetic dipole with a single perpendicular magnetic domain creates a surrounding magnetic field that is opposed to its own magnetization on its sides. The magnitude of the demagnetization field dependents on the geometry and magnetization of the specimen. In general if the sample has a high length to diameter ratio (and is magnetized in the long axis) then the demagnetization field and the magnetostatic energy will be low.

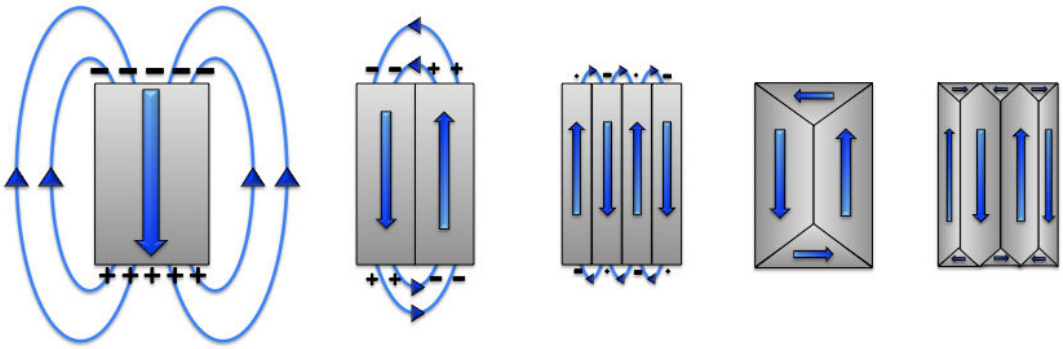

Figure 1.10: A variety of domain structures of a given particle. (+) and (-) represents the local magnetic charges. a) Uniformly magnetized (single domain). b) Two domains. c) Four domains in a lamellar pattern. d) Essentially two domains with two closure domains. (e) More complex domain structures.

The break up of the magnetization into two domains as illustrated in figure 1.10 (b) reduces the magnetostatic energy. Figure 1.10 (d) shows a closure domain structure where the magnetostatic energy is zero, however, this is only possible for materials that do not have a strong uniaxial anisotropy, and the neighboring domains do not have to be at 180º to each other.

The introduction of a domain raises the overall energy of the system, therefore the division into domains only continues while the reduction in magnetostatic energy is greater than the energy required to form the domain wall. The energy associated to a domain wall is proportional to its area. The schematic representation of the domain wall, shown in figure **??**, illustrates that the dipole moments of the atoms within the wall are not pointing in the easy direction of magnetization and hence are in a higher energy state. In addition, the atomic dipoles within the wall are not at 180º to each other and so the exchange energy is also raised within the wall. Therefore, the domain wall energy is an intrinsic property of a material depending on the value of the magnetocrystalline anisotropy and the strength of the exchange interaction between neighbouring atoms. The thickness of the wall will also

be a function of those parameters, as a strong magnetocrystalline anisotropy favors a narrow wall, whereas a strong exchange interaction facilitates a wider wall.

The size of this domain wall is determined by the configuration that minimize the two energies that are at stakes in this situation. The balance is ruled by the values of A_{ex} and K in the structure. For a given material the bigger the ratio A_{ex}/K is the wider the domain wall is, and if A_{ex}/K is small the domain wall will be thin. This can be explained by the relative predominance of one of the two interactions in each case. Furthermore the domain wall thickness δ and domain wall energy ϵ are proportional to the characteristic parameters of the system :

$$\delta \propto \sqrt{\frac{A_{ex}}{K}} \tag{1.14}$$

$$\epsilon \propto \sqrt{A_{ex}K} \tag{1.15}$$

$$\tag{1.16}$$

This description implicitly supposed that the magnetization is uniform apart from the domain wall. However parameters such as temperature, side effects, etc introduce some non-uniformity and need to be considered in simulations.

A minimum energy can therefore be reached with a specific number of domains within a specimen. This number of domains depends on the size and shape of the sample (which will affect the magnetostatic energy) and the intrinsic magnetic properties of the material (which will affect the magnetostatic energy and the domain wall energy).

Its quite common to find different possible ground states for the magnetization. The remanent state of non fully saturated sample is a good example of the competition between long range dipolar interaction and short range exchange ferromagnetic interaction. As it can be see on fig 1.12 a special domain pattern naturally nucleates and stabilizes in the remanent state in order to balance the energies involved. On fig 1.12 we can see the calculations of the energy of the two states that will finally be responsible of the regular domain size that can be observed on the fig 1.11.

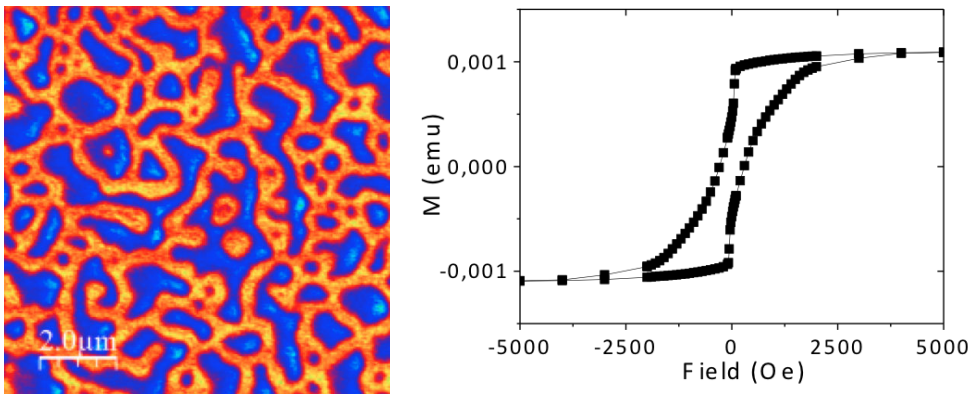

(a) (b)

Figure 1.11: (a) MFM image from the domain structure of perpendicular ($Tb_{10}Co_{90}$)(80 nm) alloy. The orange and blue colors corresponds to the up and down orientations for the magnetization. (b) Hysteresis loop associated with the MFM image at remanent state.

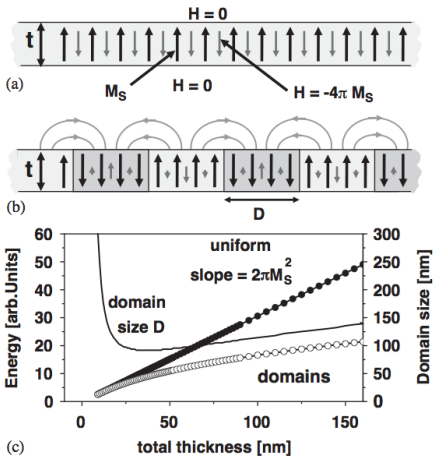

Figure 1.12: (a) Infinitely extended, uniformly magnetized (magnetization M_S, big black arrows), perpendicular thin film of thickness t. (b) Similar film split up into stripe domains of characteristic width D. For both cases the light arrows show the dipolar fields generated by the domain configuration. (c) Total magnetic energy (left axis) for both cases (a) and (b) and characteristic domain width D (right axis) for the domain state all plotted versus film thickness t. Figure extracted from *Hellwig et al.*[85]

Domain wall is just one of many different way for the magnetization to relax its inner magnetic frustration and lower its energy. Among the other it exists defects, vortices, dislocations and other singularities were special magnetic configuration usually merge. However in ferromagnets, the most important singularity is the domain wall.

Furthermore, the domain wall is a convenient way to relax the magnetic stress created by an external field for example. When external field is applied to a multi-domain ferromagnet, saturation magnetization can be achieved through the domain wall motion, which is energetically inexpensive, rather than through magnetization rotation, which carries large anisotropy energy penalty.

Domain Wall Structures

As mentioned above the domain walls are created to reduce the total magnetic energy of the system. Depending on the magnetic properties of the materials the magnetic domain boundaries have a certain width and shape. In general it exists two types of domain walls, the Bloch wall – in which spins rotate within the plane of the wall – and the Néel wall – where spins rotate in the plane perpendicular to the plane of the wall. In Fig. 1.13, the spin structures of Bloch and Néel walls are shown.

The choice between Bloch and Néel wall is more complex as the width and profile of the Néel wall are difficult to define. A more detailed description of the Néel wall profile can be found in the following references[91,90]. In the case of in-plane thin films one can consider that the Bloch wall is preferable for large thickness whereas the Néel walls become more favorable when the film thickness becomes smaller than the wall width as plotted on fig 1.14.

Besides many other kinds of domain walls exist. One of them is called the cross-tie wall, which is an intermediate state between Bloch and Neel walls, and is composed of a mixture of Bloch and Neel walls[140,196,91]. Therefore the domain wall is an intrinsic property of the material and depends on the shape and characteristics of it.

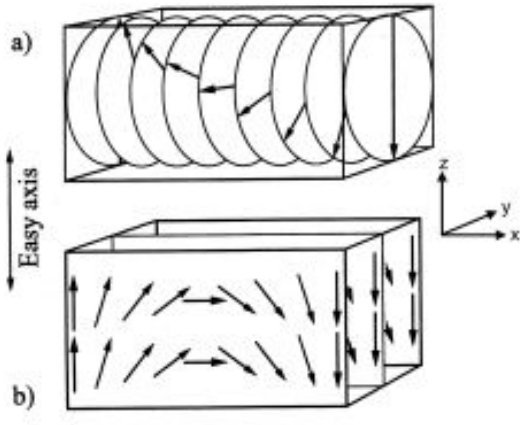

Figure 1.13: The rotation of the magnetization vector in a typical Bloch wall (a) and in a Néel wall (b). Figure extracted from *Fukumoto*[61].

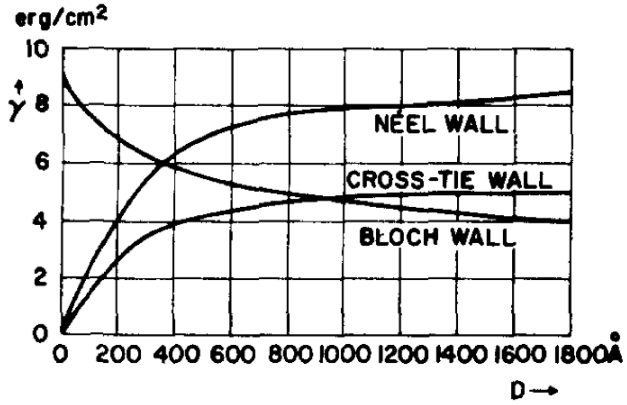

Figure 1.14: Energy per unit area of a Bloch wall, a Néel wall and a cross-tie wall as a function of the film thickness for an in-plane magnetized sample. $A = 10^{-6}\ ergs/cm$, $M_S = 800\ G$, and $K = 1000\ ergs/cm^3$. Figure extracted from *Middelhoek*[140].

1.2 Manipulation of the magnetization

Nanomagnetism is one of the most active areas in science that presents with a wide range of fundamental scientific problems. These include issues that are directly related to scaling down the dimensions such that finite size, interfacial and collective effects dominate the behavior. Examples include influence of surfaces and interface on magnetic behavior, magnetization reversal of single-domain magnets, cooperative effects in dense arrays and the broad field of spintronics which relies on manipulating the spin rather than the charge of the electron via spin injection, manipulation and detection. Magnetic materials and devices have played a major role in technology for the last half century, particularly in information storage. New discoveries in nanomagnetism are driving emerging technologies in information storage/memory/processing and biomedical applications that exploit the unique physics of spin-dynamics and spin-transport at the nanoscale.

While historically, magnetization was manipulated thru the application of magnetic fields, there is now diverse ways to control magnetization. Indeed magnetization and spin manipulation using excitations such as short-pulse or radiofrequence magnetic fields, electric fields, temperature pulses, polarized currents and polarized light are emerging. Each of these approaches couple to the magnetic system in a different way and are generally only applicable at the nanoscale. To simplify the description the dynamics and control of a nano-magnetic, one can start with the relation between the torques

applied on a system and its angular momentum variation: $\frac{d\mathbf{L}}{dt} = \mathbf{\Gamma}$. If we only consider the action of an effective magnetic field as the only torque acting on the magnetization, we obtain the following equation : $\frac{d\mathbf{L}}{dt} = \gamma \mathbf{m} \times \mathbf{H_{eff}}$ where $\mathbf{m}$ is magnetic moment and $\mathbf{H_{eff}} = \mathbf{H} + \mathbf{H_a} + \mathbf{H_{ex}} + \mathbf{H_{dis}}$ the effective magnetic field acting on the magnetization and is a combination of the applied field ($\mathbf{H}$), the anisotropy field ($\mathbf{H_a}$), the exchange field ($\mathbf{H_{ex}}$) and the dipolar field ($\mathbf{H_{dis}}$).This description ignores damping for the moment.

When manipulating magnetization with an applied magnetic field, one modifies $\mathbf{H_{eff}}$ by changing the first term $\mathbf{H}$. When electric fields are used (which also often induces strain)this results in changes Ha or m. These approaches are limited to nano devices because of the skin depth of electric fields in metals. When using polarized current via spin transfer torques one is modifying $\frac{d\mathbf{L}}{dt}$ via transfer of angular momentum from the electrons to the magnetic system. Since the electron spin is conserved only for distance close to the spin diffusion length these effect are also limited to the nanoscale. In the case of magnetic control with pulsed polarized laser light, it is more complex since light transfers both angular momentum and heat. Because of light polarization one modify dL/dt, and because of the large amount of heat transfer in a very short time it causes temperature change for spin, electron and lattice bath and it leads to change of $\mathbf{m}$, $\mathbf{H_{ani}}$, $\mathbf{H_{ex}}$, $\mathbf{H_{dip}}$, strong thermal gradients and possibly superdiffusive spin currents. More-over, like all those new approaches, optical control is limited to nanoscale systems via the optical skin depth and are not applicable to the macroscopic world.

The quantitative understanding of the role of spin-polarized currents on magnetization dynamics has emerged over the last 15 years and has enabled new technologies such as spin transfer torque - magnetic random access memory (STT-MRAM)[134]. The role of optical excitations on magnetic control is at a much earlier stage as our very recent paper on optical switching of ferromagnetic materials reported[120]. Understanding and controlling this phenomenon requires the combined effects of materials synthesis, nanofabrication, device physics and time-resolved experiments of systems driven from equilibrium.

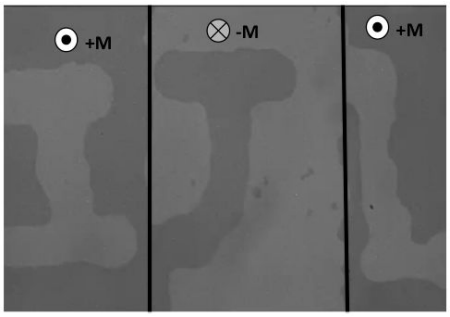

Figure 1.15: Magneto-optical image of IJL written in a magnetic film using a circularly polarized 100-fs laser pulses where the orientation of the magnetic domains were controlled by sweeping circular polarized light over the film. The whole image is approximately 300 μm wide.

We are particularly interested in building on our recent advances in the direct control of magnetization through the interaction with polarized light pulses. Shown in `http://www.youtube.com/watch?v=SaOkwR2dmpg` is a YouTube video where we are able to write "IJL" into a magnetic film using only circularly polarized light pulses (see Fig. 1.15). Following this path, further integrating magnetic nanostructures with photonic devices will provide unique opportunities to probe fundamental properties of magnetic materials with high spatial and temporal resolution. An important and exciting aspect of this domain of research is to integrate the materials in spintronic devices to probe the magnetization dynamic and extend studies of nano-scale magnetic materials into the femto-second

temporal range. Finally we will demonstrate spintronic devices where light can not only be used to change magnetization orientation and consequently write information but can also permit to read the information without any current injection. While the thesis is focused on the fundamental physical phenomena the low-power manipulation of magnetization, preferably at ultra-short time scales, has become a fundamental challenge with implications for future magnetic information memory and storage technologies.

1.2.1 Electric field

In the push for low-energy consumption memory and logic applications, the field of spintronics has focused on establishing control of a magnetization without the need of an external magnetic field applied[144,33,149,173,67]. The current technologies are focused on the use of large current densities in spin transfer torque-based devices[32,167,182] significant energy is lost especially through Joule heating which is responsible for a delay in the large range of applications already expected. Promising alternatives and a rich field of physics now reside in the use of correlated systems such as multiferroic magnetoelectrics[49,185]. In these materials an electric field can be applied to the multiferroic to alter its magnetic order[128,123,124].

Following this approach *Chiba et al.*[34] in Japan discovered in 2003 that some ferromagnetic semiconductors can have their magnetic properties tuned thanks to an electric field applied. Using a regular gated structure based on transistor technology on a ferromagnetic Mn-doped InAs, they were able to continuously modify the coercivity of the material through the application of an external electric field (see fig 1.16).

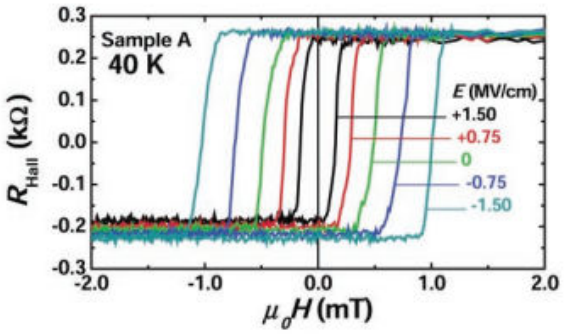

Figure 1.16: Electric-field dependence of the magnetic hysteresis curves measured by use of the anomalous Hall effect of a [(In,Mn)As] sample at 40 K. Figure extracted from *Chiba et al.*[34]

In this structure, the application of the electric field on the channel modifies the hole concentration and the transition temperature T_C of the material normally occurring around 50K. A negative or positive bias result respectively in an increase or a decrease of the T_C via the interaction of the localized spins of Mn with the holes in the channel. Thanks to this dependence of the switching field with the bias applied, the manipulation of the magnetization can now be electrically-assisted as shown in fig 1.17 where a demagnetization of the sample and the subsequent reversal using a very small applied field is shown.

In this particular material where low-density carriers are responsible for the ferromagnetic interaction they demonstrate that the magnetization reversal is assisted by making the system closer to or beyond its Curie temperature. It is particularly of interest as this kind of Curie point writing technics are currently investigated in magneto-optical memory disks for ultrahigh-density magnetic recording,

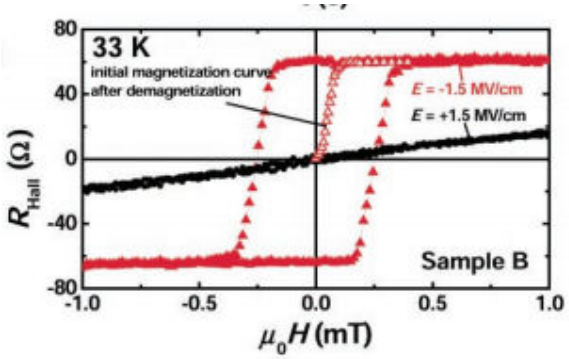

Figure 1.17: Electrical demagnetization of the channel layer by electric field in a [(In,Mn)As] channel structure. Figure extracted from *Chiba et al.*[34]

so instead of using a laser-light irradiation different solutions could be used.

In addition to fundamental interest in controlling order parameters by electric fields through gate voltage, such electric-field control of magnetism is technologically appealing because of its low power demands and potential for miniaturization.

1.2.2 Polarized currents

LLGS Equation

Considering a ferromagnet in the macrospin approximation with an injected current through it and an external magnetic field applied, the magnetization will be modified in different ways. We can describe the behavior of the magnetization with the Landau-Lipschitz-Gilbert- Slonczewski or LLGS equation[183]:

$$\frac{d\mathbf{m}}{dt} = -\gamma_0 \mathbf{m} \times H_{eff} + \alpha \mathbf{m} \times \frac{d\mathbf{m}}{dt} - \beta I \mathcal{G}(\theta) \mathbf{m} \times (\mathbf{m} \times \mathbf{p}) \tag{1.17}$$

where $\mathbf{m}$ (resp. $\mathbf{p}$) is the unitary vector in the direction of the free layer (resp. polarizer) magnetization. α the Gilbert damping parameter. γ_0 the Larmor precession frequency of the electron. β is equal to $\frac{h\gamma_0}{2\mu_0 M_s V e}$. and $\mathcal{G}(\theta)$ expresses the angular variation of the spin-transfer torque through the spin valve.

The LLGS equation show three terms corresponding to three different torques :

– The first term corresponds to the field torque leading to the precession of the magnetization around the direction of an effective magnetic field at the frequency $\gamma_0 \mathbf{H}_{eff}$. This effective magnetic field has been defined in section 1.1.2.

– The second term is the damping term. Indeed permanent precession is only possible considering the first conservative term. The magnetization dissipates energy ends up reaching its stable static equilibrium position parallel to the effective field. By adding the damping term, the magnetization will exhibit damped oscillations as long as the magnetization is misaligned with the effective field. The period of these oscillations is of the order of $\sim$ 100 picoseconds and the characteristic time of the damping is of the order of a few nanoseconds.

– The last term of the equation represents the spin-transfer torque that is acting on the magnetization. The spin transfer torque is parallel or antiparallel to the damping torque depending on the

sign of the term.

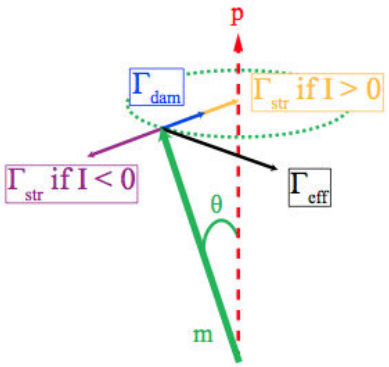

Figure 1.18: Torques ruling the free layer magnetization dynamics.

The figure 1.18 shows the three contribution and the effects they involve on the magnetization.

Qualitative Description of spin transfer

The spin transfer phenomenon appears as a polarized current flows through a magnetic layer with a preferred orientation. Electron spin entering in the magnetic layer is influenced by the local magnetization and precesses along the effective magnetic field and finally aligns with it. During the precession, the conduction electron (in our case) will transfer its transverse spin to the layer itself, in order to conserve the total spin angular momentum during the motion.

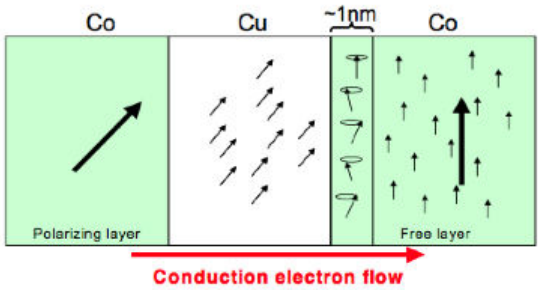

Figure 1.19: Representation of the spin transfer phenomenon through a spin valve. Figure extracted from *Herault et al.*[87]

If we consider a spin valve structure made of two ferromagnetic layers separated by a non magnetic layer, once the conduction electrons leave the polarizer (also called the hard layer), the spins keep their orientation as long as they don't interact with another magnetic layer (in reality, there is a typical spin diffusion length for each material that scatter the preferential orientation of the current after a certain distance). When the electrons reach the soft layer, the electrons flowing from one layer to the other can transfer angular momentum. This contribution will increase the precession of the magnetization of the soft layer and lead to a reversal if the current is large enough. The figure 1.20 shows the typical oscillations of the magnetization of the soft layer during the reversal.

Quantitative Description of spin transfer

It turns out that the spin transfer torque effect is an interface effect, so we need to consider the modification of the spin density near the interface. Several approaches exist even using a quantum

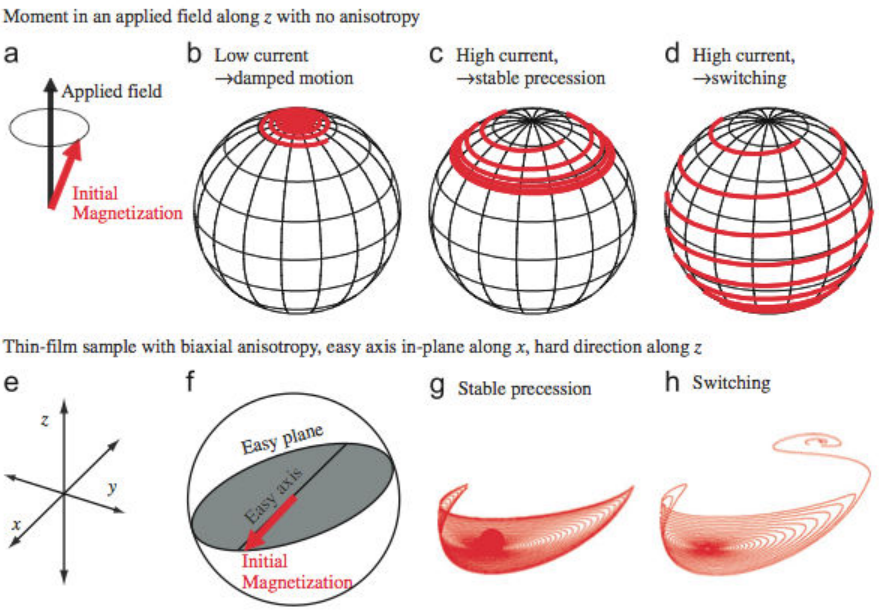

Figure 1.20: Trajectories of spin-torque-driven dynamics for the magnetization on a sample with no magnetic anisotropy (a-d) or with an easy axis (e-h). Figure extracted from *Ralpha et al.*[168]

description of this phenomenon. However the model developed by M. Stiles[168] and J. Miltat permits to give a good overview of the key aspects that are included in the phenomenon.

Let's consider the interface between a non-magnetic and a ferromagnetic layer (see figure 1.21). A spin current consists of spins moving. Since both spin and velocity are vectors, the spin current ($\mathbf{Q}$) is a tensor quantity.

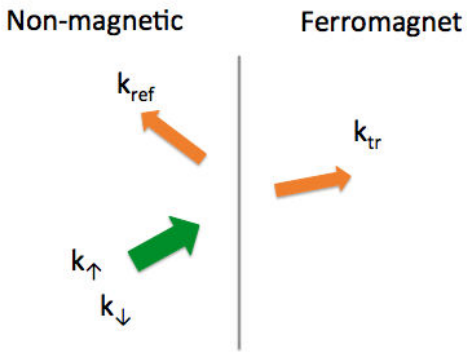

Figure 1.21: Illustration of the interaction of a spin current with a non-magnetic/magnetic interface. $k_{\uparrow}$,$k_{\downarrow}$, k_{ref} and k_{tr} are respectively the incident (up and down spins), reflected and transmitted wave vector of the spins.

Classically it is described as the outer product of the electron's spin ($\mathbf{S}$) and its velocity ($\mathbf{v}$):

$$\mathbf{Q} = \mathbf{S} \otimes \mathbf{v} \tag{1.18}$$

In the particular case of a one dimensional problem (as in a spin current flowing perpendicular to a nanopillar) the spin current for the whole electrons can be factored into the outer product. So it is possible to present the spin current into the outer product of a dimensionless direction $\hat{\mathbf{s}}$ and the number current $\mathbf{j}$ times the scalar polarization P:

$$\mathbf{Q} = \frac{\hbar}{2} P \ \hat{\mathbf{s}} \otimes \mathbf{j} \tag{1.19}$$

We can then consider the continuity equation at the interface.

$$\frac{\partial \mathbf{s}}{\partial t} = -\bigtriangledown \cdot \mathbf{Q} + \mathbf{n_{ext}} \tag{1.20}$$

with $\mathbf{n_{ext}}$ the external torque density due to the not commuting terms such as the Zeeman interaction or magnetocrystalline anisotropy.

Indeed when a ferromagnet has a spatially uniform magnetization and there is no applied current, the spin current carried by the up moving states exactly cancels the spin current carried by the down moving states (in a vertical nanopillar). But when a spin current is flowing through a magnetic material the imbalance in the populations of the states near the Fermi energy will polarize the current and creates a net spin current at the interface. For a uniform spin current incident from the non-magnet, the spin flux through the interface in the non-magnet has a contribution to the incident and the reflected spin current $(\mathbf{Q_{in}} + \mathbf{Q_{ref}}) \cdot (-\hat{\mathbf{z}})A$ (A the surface considered at the interface, $-\hat{\mathbf{z}}$ the interface normal). For the interface in the ferromagnet, the transmitted spin current is $\mathbf{Q_{tr}} \cdot \hat{\mathbf{z}} A$. The total change in the spin flux acts as like a torque on the magnetization:

$$\Gamma_c = (\mathbf{Q_{in}} + \mathbf{Q_{ref}} - \mathbf{Q_{tr}}) \cdot \hat{\mathbf{z}} \ A \approx \mathbf{Q_{\perp}^{in}} \cdot A \ \hat{\mathbf{z}} \tag{1.21}$$

The behavior of the spin currents at the interface is dominated by the spin dependent reflection of the electrons. The exchange interaction in the ferromagnet gives different properties to the electrons at the Fermi level depending on whether their moments are parallel or antiparallel to the magnetization. As a consequence the reflection amplitudes for electrons coming from a non-magnet and scattering at the interface with a ferromagnet depend on whether the electron's spin is parallel or antiparallel to the magnetization (respectively associated with $R_\uparrow$ and $R_\downarrow$ reflection coefficients). The transmission amplitudes, $T_\uparrow$ and $T_\downarrow$ are similarly spin dependent.

The reflection and transmission of electrons with spins at arbitrary angles to the magnetization determines the torque. In the $(|\uparrow\rangle \ , \ |\downarrow\rangle)$ basis, the state of an electron with a spin at a polar angle θ and azimuthal angle ϕ is a coherent superposition of the spin up state and the spin down state:

$$|\theta, \phi\rangle = \cos(\frac{\theta}{2}) e^{-i\phi/2} \, |\uparrow\rangle + \sin(\frac{\theta}{2}) e^{i\phi/2} \, |\downarrow\rangle \tag{1.22}$$

Thus when an electron starting in the non-magnet in the state $e^{ikz} \, \langle\theta, \phi|$ reflects, it comes back in a different state:

$$e^{-ikz} \left[R_\uparrow \cos(\frac{\theta}{2}) e^{-i\phi/2} \, |\uparrow\rangle + R_\downarrow \sin(\frac{\theta}{2}) e^{i\phi/2} \, |\downarrow\rangle \right] \tag{1.23}$$

The reflected electron is rotated with respect to the incident electron. Similar considerations apply to the transmitted electrons but with an additional complication. When electrons are in the ferromagnet, the different spin components have different wave vectors, $k_\uparrow$ and $k_\downarrow$. The consequence of this difference is that the phase between the up spin and down spin amplitudes, $e^{i(k_\uparrow - k_\downarrow)z}$ changes as the electron penetrates further into the ferromagnet. This changing is simply precession around the magnetization.

This model simply illustrates one of the ideas behind Slonczewski's original model for this effect. Here, a spin filter effect spatially separates the majority and minority spin currents from each other.

The transverse part of the incident spin current is being absorbed by the magnetization which implies a reaction torque on the magnetization. Even though this model is a simple approximation of the real phenomenon, the conclusions hold approximately for transition metal interfaces like Co/Cu for example. However this small presentation will be enough to the understanding of the physics in this report.

1.2.3 Polarized Light

An interesting and important outcome from studies of laser-induced ultra-fast dynamics of magnetic systems is the demonstration that light can directly switch magnetic domains using circularly polarized light without any applied magnetic field. In their pioneering work the T. Rasing group in Nijmegen showed in 2007 fully deterministic magnetization switching in a ferrimagnetic GdFeCo alloy film using single circularly polarized femtosecond laser pulses[186]. This remarkable phenomenon has been termed All Optical Switching (AOS) and occurs on a timescale of a few tens of picoseconds[109], about two orders of magnitude faster than anything feasible without using relativistic electron sources. Thus, AOS may lead to technological breakthroughs by using polarized light for ultrafast magnetization manipulation for a variety of applications. Moreover this process appears highly energy efficient since an energy lower than 10 fJ is expected to be sufficient to switch a 20 x 20 nm^2 area of magnetic material. Until recently observations of AOS were only reported for a narrow composition range of GdFeCo films which is an amorphous rare-earth transition-metal (RE-TM) ferrimagnetic alloy. During the last two years our group together in collaboration with T. U. Kaiserlautern and UC San Diego have demonstrated that AOS can be observed not only in GdFeCo alloy films but also in a much broader variety of materials, including RE-TM alloys, multilayers and heterostructures. Further more it was shown that RE-free Co-Ir-based synthetic ferrimagnetic heterostructures designed to mimic the magnetic properties of RE-TM alloys also exhibit AOS.

Spin Angular Momentum

Starting with the mere observation of the tails of comets by Kepler, the interest of scientists for the mechanical effects of light kept growing with time. If a qualitative description of the radiation pressure of light was developed very early, but a fully quantitative theory of such effects became possible only after the development of Maxwell's unified theory of electricity, magnetism and optics. However, although his treatise on electromagnetism contains a calculation of the radiation pressure at the earth's surface, there is little on the mechanical effects of light. Poynting[162] was the one that quantified the momentum and energy flux associated with an electromagnetic field. To do so he used a mechanical analogy to quantify this momentum that we will describe here.

Poynting was convinced that circularly polarized light must carry angular momentum so he proceeded by analogy with the wave motion associated with a line of dots marked on a rotating cylindrical shaft to demonstrate this effect. In his model, the expression for the orientation θ of any section of a shaft distant x from the origin, $\theta = 2\pi\lambda^{-1}(Ut - x)$, serves also as an expression for the orientation of the perturbation, whatever it's nature, constituting circularly polarized light.

For simplicity, let's consider a shaft consisting of a thin cylindrical tube with the given radius of a, the cross-section of the material s, the rigidity n, and the density ρ. Let the tube make N revolutions per seconds, and let it have such twist on it that the velocity of transmission of the spiral indicating the twist is the natural velocity $U_n = \sqrt{n/\rho}$.

Considering the strain energy per unit length is $1/2n\epsilon^2$ since $\epsilon = ad\theta/dx = -a\dot{\theta}/U_n$, the strain energy is $1/2na^2s\dot{\theta}^2/U_n^2 = 1/2\rho a^2 s\dot{\theta}^2$.

But the kinetic energy per unit length is also $1/2\rho a^2 s\dot{\theta}^2$, so that the total energy in length U_n is $\rho a^2 s\dot{\theta}^2 U_n$. The rate of working across a section is :

$$n\epsilon sa\dot{\theta} = \rho a^2 s\dot{\theta}^2 U_n \tag{1.24}$$

where the energy transferred across a section is the energy contained in length U_n.

If we put E for the energy in unit volume and Γ for the torque per unit area, we have $\Gamma s\dot{\theta} = EsU_n$, whence

$$\Gamma = EU_n/\dot{\theta} = EN\lambda\ 2\pi N = E\lambda/2\pi \tag{1.25}$$

The analogy between circularly polarized light and the mechanical model suggests that a similar relation between torque and energy may hold in a beam of such light incident normally on an absorbing surface. If so, a beam of wavelength λ containing energy E per unit volume will give up angular momentum $E\lambda/2\pi$ per second per unit area. But in the case of light waves $E = P$, where P is the pressure exerted. We may therefore put the angular momentum delivered to unit area per second as :

$$P\lambda/2\pi \tag{1.26}$$

This calculation shows that $E\lambda/2\pi$ is the angular momentum transmitted through a plan in unit time, per unit area, where E is Poynting's notation for the energy per unit volume and λ is the wavelength. When the energy of each photon crossing the surface is associated with $\hbar\omega$, we obtain the results that each circularly polarized photon carries $\hbar$ units of angular momentum.

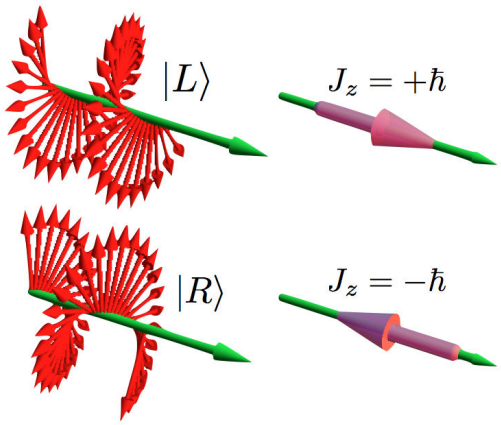

Figure 1.22: Left and right handed circular polarization, and their associated angular momenta. Figure extracted from *Karimi*[102]

The value of the spin angular momentum in any practical case is very small. Beth[15] made the first observation of the angular momentum of light following Poynting, who inferred from a mechanical analogy that circularly polarized light should exert a torque on a birefringent plate and that the ratio of angular to linear momentum is equal to $\lambda/2\pi$. In this experiment a half-wave plate was suspended by a fine quartz fiber. A beam of light, circularly polarized by a fixed quarter-wave plate, passed through the place which transformed right-handed circularly polarized light into left-handed circularly polarized light and transferred $2\hbar$ of spin angular momentum for each photon to the birefringent plate. It was found that the measured torque agreed in sign and magnitude with that predicted by both wave

and quantum theories of light. The ratio of the angular momentum of N photons in the beam, $J = \pm N\hbar$, to their energy, $W = N\hbar\omega$, is $\pm 1/\omega$ and Beth's measurements is sometimes referred to as the measurement of the spin angular momentum of the photon.

Orbital Angular Momentum

The modern study of optical angular momentum really started with the paper of *Allen et al.*[2]. This work showed that any beam with the amplitude distribution as followed $u(r, \phi, z) = u_0(r, z)\exp(il\phi)$ carried angular momentum about the beam axis.

The angular momentum density associated with the transverse electromagnetic field may be shown[94] to be:

$$M = \epsilon_0 r \times (E \times B) \tag{1.27}$$

while the total angular momentum of the field is :

$$J = \epsilon_0 \int r \times (E \times B) dr \tag{1.28}$$

In general two contribution for the total angular momentum can be separated, the spin S and orbital L angular momentum. However depending on the case, and especially in atomic physics, it can be difficult to distinguish both parts as physically observable parameters vector fields[37] :

$$J = L + S \tag{1.29}$$

Looking at the orientation of $E \times B$, it is clear that the linear momentum of a transverse wave lies directly along the propagation direction (z in our case). This is valid for an ideal transverse wave and implies that no angular moment $r \times (E \times B)$ can be transfer along the direction of propagation. However, In most of the case the fields of a laser modes TEM_{lmq} are not strictly transverse[122]. Because of this small dependence, a small contribution exists along z.

Let's consider a linearly polarized laser mode as expressed by *Haus et al.*[84] with a Lorentz gauge linked to the vector potential $A = u(x, y, z)e^{-ikz}$. In the paraxial approximation $u(x, y, z)$ is the complex scalar function describing the distribution of the field amplitude which satisfies the wave equation. The paraxial approximation we can that the second derivatives of E and B fields, and the products of the first derivatives, are ignored and $\partial u/\partial z$ is taken to be small compared with ku. Using the cylindrically symmetric solution $u(r, \phi, z)$ which describe Laguerre-Gaussian beams we have :

$$\begin{aligned} u(r, \phi, z) = \frac{C}{(1 + z^2/z_R^2)^1/2}\left(\frac{r\sqrt{2}}{w(z)}\right)L_p^l\left(\frac{2r^2}{w^2(z)}\right) \\ \times \exp\left(\frac{-r^2}{w^2(z)}\right)\exp\left(\frac{-ikr^2 z}{2(z^2 + z_R^2)}\right)\exp\left(-il\phi\right) \\ \times \exp\left(i(2p + l + 1)\tan^{-1}\frac{z}{z_R}\right) \end{aligned} \tag{1.30}$$

where z_R is the Rayleigh range, $w(z)$ is the radius of the beam, L_p^l is the associated Laguerre polynomial, C is a constant, and the beam waist is at $z = 0$.

Then we can calculate the linear momentum density for a beam of unit amplitude, which is basically

the time average of the real part of $\epsilon_0 \mathbf{E} \times \mathbf{B}$:

$$\frac{\epsilon_0}{2}(\mathbf{E}^* \times \mathbf{B} + \mathbf{E} \times \mathbf{B}^*) = i\omega\frac{\epsilon_0}{2}(u^*\nabla u - u\nabla u^*) + \omega k\epsilon_0|u|^2 z \tag{1.31}$$

Considering our linearly polarized light following a Laguerre-Gaussian distribution , the momentum density per unit power is found to be:

$$\mathcal{P} = \frac{1}{c}\left(\frac{rz}{(z^2 + z_R^2)}|u|^2 r + \frac{l}{kr}|u|^2\phi + |u|^2 z\right) \tag{1.32}$$

where r and ϕ are unit vectors and $|u|^2 = |u(r, \phi, z)|^2$.

Here the $\partial u/\partial z$ term has now been neglected. It may be seen that the Poynting vector, given by $c^2\mathcal{P}$, spirals along the direction of propagation, the chirality and rotation speed resulting from the value of l; see fig 1.23. The r components relates to the spread of the beam; the ϕ component gives rise to orbital angular momentum in the z direction and the z component relates to the linear momentum P in the direction of propagation.

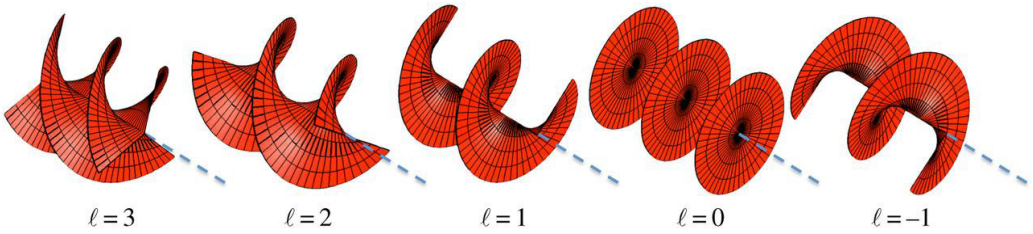

Figure 1.23: When laser beams have helical phasefronts, their energy and momentum twist around the beam axis, and the beam carries an orbital angular momentum of $l\hbar$ per photon. Figure extracted from *Padgett.*[154]

Calculation of the time averaged angular momentum density, $\epsilon_0 \mathbf{r} \times \langle \mathbf{E} \times \mathbf{B} \rangle$, per unit power yields:

$$\mathbf{M} = -\frac{l}{\omega}\frac{z}{r}|u|^2 r + \frac{r}{c}\left(\frac{z^2}{z^2 + z_R^2} - 1\right)|u|^2\phi + \frac{l}{\omega}|u|^2 z \tag{1.33}$$

The radial and azimuthal components are symmetric about the axis, so that integration over the beam profile leaves only the z component. The ratio of the flux of angular momentum to that of energy is $L/cP = l/\omega$, while the ratio of angular momentum to linear momentum is now $L/P = l(\lambda/2\pi)$. It proves that Laguerre-Gaussian beams possesses a well-defined orbital angular momentum due to the phasefront spatial evolution of the beam.

We have so far considered linearly polarized light but when the vector potential is generalized to arbitrary polarization we find:

$$\frac{\epsilon_0}{2}(\mathbf{E}^* \times \mathbf{B} + \mathbf{E} \times \mathbf{B}^*) = i\omega\frac{\epsilon_0}{2}(u^*\nabla u - u\nabla u^*) + \omega k\epsilon_0|u|^2 z + \omega\sigma_z\frac{\epsilon_0}{2}\frac{\partial|u|^2}{\partial r}\phi \tag{1.34}$$

where the first two terms are polarization independent and relate to orbital angular momentum and the final term is a polarization, or spin, part. These lead to a z component of total angular momentum density per unit power:

$$M_z = \frac{l}{\omega}|u|^2 + \frac{\sigma_z r}{2\omega}\frac{\partial|u|^2}{\partial r} \tag{1.35}$$

The ratio of the angular momentum flux to energy flux now becomes $J/cP = (l + \sigma_z)/\omega$ where $\sigma_z, = \pm 1$ for right-handed or left-handed circularly polarized light and $\sigma_z = 0$ for linearly polarized

light. We may note that in the paraxial approximation the spin-dependent part of angular momentum density depends upon the gradient of the intensity. Thus at a particular local point the z component of angular momentum flux divided by energy flux does not yield a simple value. However, when the total angular momentum flux is calculated, the integration across the beam profile leads to the simple result of the preceding paragraph.

In the Beth experiment right-handed circularly polarized light, $-\hbar$, was converted to left-handed circularly polarized light, $+\hbar$, so that $2\hbar$ of spin angular momentum per photon was imparted to the birefringent plate. In the same way the maximum transfer of orbital angular momentum would take place if a Laguerre-Gaussian beam possessing $l\hbar$ angular momentum per photon were converted into one with $-l\hbar$ per photon. The torque arising from the transfer of momentum must then be measured by an appropriate equivalent of the birefringent plate.

Ultrafast angular momentum transfer in metals

Exploration of relaxation mechanisms

Since the discovery of ultrafast demagnetization of a Ni film by *Beaurepaire et al.*[11] in 1996, the interactions of ultrafast light pulses with magnetism has been the subject of many fundamental discoveries. But if many aspects of this phenomenon have been explored through different approaches[11], the physics of manipulating and controlling magnetization with subpicoseconds pulses is still challenging the community. Along with the possibility of optically generated coherent magnetic precession[98,209], laser-induced spin reorientation[105,16], or even modification of the magnetic structure[97,195], the study of the fundamental mechanism leading to magnetization manipulation is obviously a great challenge. Moreover it could open access to new technologies of data storage and magnetic memories.

The effects of a ultrafast pulsed laser bring the magnetic system in a highly unstabled state due to heat and magneto-optics effects. If the conventional models developed for direct current or field inputs have difficulties to fit, it is however possible to look at the different magnetic interactions involved to analyze the results. One of the characteristic of magnetic interactions is the wide range of time scale existing for the mechanisms (see fig 1.24). As the system is recovering from the strong excitation of the pump laser, the interactions have consecutively a greater influence on the magnetism to end up in the final and sometimes metastable state. When exciting in the subpicosecond time domain, it is possible to probe all the different magnetic subsystems and the way they interact. From electron motion to charge and spin evolution, every contribution to the electronic structure is changing with time and the magnetic interactions resulting form their relative evolution, such as spin-orbit coupling or anisotropy, become time-dependent. All these issues seriously complicate a theoretical analysis of this problem.

If in a first approximation the heat introduced by the ultrafast pulse is only supposed to modify amplitude of the magnetic parameters, the demagnetization and subsequent controlled reorientation of the spin seems to need additional considerations to be explained. As described earlier the polarization and in some particular cases the wavefront of the light bring some angular momentum to the system. Such input can be critical for the determination of the final state of the magnetization however in order to predict such evolution it is necessary to understand the fundamental mechanisms responsible for the spin-flip in ferromagnetic metals. If many different hypothesis have been explored, three mechanisms are mainly used to illustrate the way an excited electron can flip its spin in a ferromagnetic metal. These are the Stoner excitation[193]; the inelastic electron-spin-wave scattering event[48,225]; and the spin-

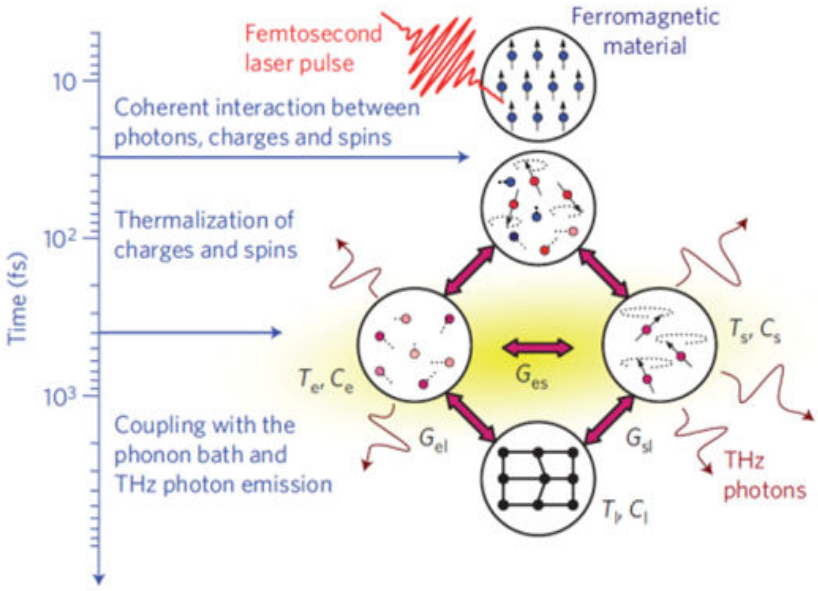

Figure 1.24: Sequence of mechanisms in ultrafast magnetization dynamics. A femtosecond laser pulse interacts with the charges and spins of a ferromagnet which consequently induces a demagnetization. This coherent step is followed by the thermalization of the charges and spins, which interact together with the lattice through coupled baths described by three temperatures T_e, T_s and T_l and coupling constants G_{es}, G_{el} and G_{sl}. Figure extracted from *Bigot.*[16]

flip scattering with impurities or phonons, also called the Elliott-Yafet mechanism[50,218]. A common interest of this path is the short time scale involved, which corresponds to the typical relaxation time observed in experiment.

In metals with itinerant electron system, the electron-electron interaction leads to a different energy dependence for the electron bands of spin up and spin down (see fig 1.25). Depending on the position of the Fermi level, the two channels will be filled unevenly which will be responsible for the total net polarization of the material. However the two spin-up and spin-down bands are not fully independent and an exchange-split at the Fermi level can occur leading to a transfer of an electron from the majority (lower-energy band) channel to the minority (higher-energy band) channel, called the Stoner excitation. The energy levels are not discrete, a probability then will be associated with each reversal event depending on the relative filling of the two bands, which will be responsible for a distribution of the Stoner excitation[142]. The electron-hole pair is usually described with a single parameter which is the net vector of the combination.

Due to the band structure of ferromagnet and its individual nature, Stoner excitation usually requires high energy to occur. On the opposite, many consecutive small chains of virtual recombinations implying small energy and small wave vector can end in a similar absorption of any additional momentum brought to the system. In this case, the collective magnetic excitation made of the coherent superposition of tilted state is called a spin wave and is dominant at low energy.

The last main mechanism existing in metals relates to the entanglement of states in metal. Because of the spin-orbit coupling an electronic state in a solid is always a mixture of the two spin states, e.g., a dominant spin-up contribution or vice-versa a small spin-down contribution, defining the total crystal wave function[189] as a linear combination of the two. Following the Elliott-Yafet theory[50,218] some of the incoming photon scattered by the electron of the system modifies this linear combination and thus changes the probability to find the electron in one of the two states. As a consequence the photon will transfer angular momentum through scattering. If a theoretical analysis is possible via

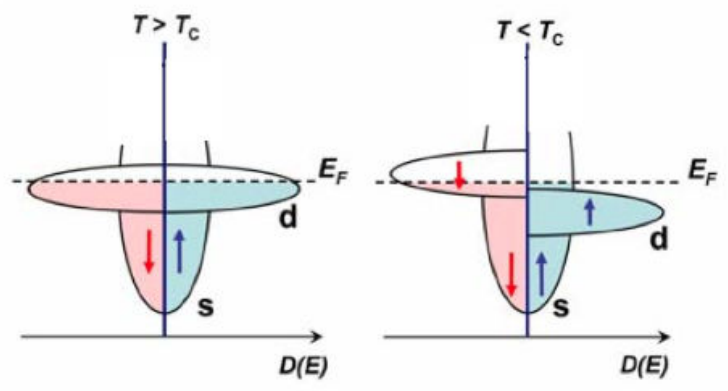

Figure 1.25: Energy band structure of material depending on the orientation of the electron spin for a ferromagnetic material (right) and a non-magnetic material (left). Figure extracted from *Bernard-Grander.*[55]

ab-initio calculations based on density functional theory for example, the experimental determination of such spin-mixing parameters happen to be much more complicated to discretize. In fact some calculations[189] already demonstrate very high value of spin-mixing in ferromagnetic transition metals (Co, Fe and Ni) compared to Cu only. This would support the idea that such mechanism could be of prime importance during ultrafast excitation with lasers. On the other side, the first attempts[113,115] to fit the experimental results are still debated in the field[215,166] and will probably require further investigations to conclude.

Inverse Faraday Effect

Apart from the direct investigation of the interaction with electrons it exists a more general phenomenological framework describing circularly polarized light : the Inverse Faraday Effect (IFE). Discovered in 1845 by Michael Faraday the Faraday effect corresponds to the rotation of the plane of polarization of an electromagnetic wave when interacting with a media subject to a magnetic field. The Faraday effect is a direct consequence of the circular birefringence that characterizes the relative speed of propagation of left and right circularly polarized waves in dielectric media. As a consequence the Inverse Faraday effect occurs when circularly polarized light incident on a non-absorbing crystal induces a magnetic moment in that material[106]. Then circularly polarized pulses can act on spins as an effective light-induced magnetic field pulse with a direction determined by the helicity of the light.

However the current theoretical and experimental descriptions of this effect is limited[220,66] and needs to be upgraded to take into account the recent advances in subpicoseconds laser pulses. In order to have an estimation of the magnetic field pulse parameters created in the material we can consider the phenomenological expression of IFE that is usually used for transparent material in thermodynamic equilibrium[160,156,157]:

$$\mathbf{H}_{IFE}(t,r) = \epsilon_0 \chi [\mathbf{E}(t,r) \times \mathbf{E}^*(t,r)] \tag{1.36}$$

where $\mathbf{H}_{IFE}$ is the induced opto-magnetic field, ϵ_0 is the vacuum permittivity, χ is the magneto-optical susceptibility and $\mathbf{E}(t,r)$ is the envelope of the electric field of light. A direct consequence of this expression is that in an isotropic material, the amplitude of $\mathbf{H}_{IFE}$ is determined solely by the helicity of the incident beam. Furthermore, the field is directed along the wavevector of light and the

sign of the transient magnetic field will be reverted if we revert the polarity of the light.

It is then possible to estimate the strength and duration of the magnetic field knowing the characteristics of the incident light pulse. $\mathbf{H}_{IFE}$ then becomes[109]:

$$\mathbf{H}_{IFE}(t,r) = \sigma \frac{2\chi F}{c\tau} f(t) e^{-\frac{r^2}{r_0^2}} \mathbf{n} \tag{1.37}$$

where c is the speed of light, n is the unit vector in the direction of the wavevector of light and r_0 characterizes the Gaussian spot size. F corresponds to the laser pulse fluence and τ is the pulse duration (full width half maximum). In this condition, $F/\tau \simeq c\epsilon_0/2|E_0|^2$. The coefficient σ gives the degree of circular polarization and is equal to ± 1 for a right- (σ^+), left-handed (σ^-) circularly polarized light and equal to 0 for a linearly polarized (π), respectively. The time-dependent function $f(t)$ and the space-dependent Gaussian function describe the temporal and spatial profiles of the effective field.

As a consequence, the spatial extend of the effective light-induced magnetic field is clearly limited by the spatial profile of the beam. When it comes to the temporal influence of the effective field, we have to consider the different interaction modes existing in the medium. If it is almost clear that $\mathbf{H}_{IFE}$ builds up with no delay with respect to the laser pulse electric field, the decay is proven to be longer than the real light pulse duration. The lower limit for the decay of the light-induced field could be set to the optical coherence time, which is well below 100 fs in metals[118,159]. As the origin of the IFE remains unclear, it is only possible to estimate the upper limit of the decay time. Some of the previous works[88,221,219] relate the emerging effective field to possible light-induced elliptical currents which would entail a picoseconds range for the life-time of such effect in metals. A very limited number of experiments[12,89] focused on the detection of such currents, but the emission of polarized THz radiation in the case of iron films subjected to 50 fs laser pulse excitation could be associated to IFE. The interpretation of this radiation in terms of solenoidal light induced currents would imply a decay time of a few picoseconds (3 ps for the iron studied in[89]). As a consequence the interaction of laser pulses with metals seems to be considerably longer than the light pulse duration.

Even if the IFE represents a tantalizing model to describe the first results obtain with helicity dependent magnetic switching, it is necessary to point out that it stem from a phenomenological representation. A deeper exploration of the limits of the effects still need to be done for example considering the non-absorbing framework initially used to calculate the effect. In addition, subpicosecond laser pulses are known to lead to a rapid increase of the electronic temperature in metals[11]. Therefore, an understanding of the role of the subsequent heat pulse and its relaxation is required and will be describe in the next section.

1.3 Temperature influence on a magnetic system

The LLGS equation described in the previous parts is based on the representation of the magnetic interaction without any thermal dependence. If the experiments can be performed in laboratories at very low temperature, most of the technologies based on magnetism are often used at room temperature. In this circumstances it is necessary to develop an approach of the system at finite temperature. We will first focus on the role of the temperature at longer time scale and its integration in the regular LLGS equation. In a second time, we will see what are the consequences of a very short heat pulse on the ultrafast dynamic of magnetic systems.

1.3.1 Temperature as static fluctuations of field

The temperature has two main influences on magnetism : First of all, most of the magnetic properties depends on temperature and such modifications must be considered to model properly real systems; additionally at a given working temperature, the magnetic system will fluctuate randomly and the stability of certain configurations can be strongly modified.

The main representation of the thermal fluctuation was developed by *Brown*[21] in 1955 and describes the temperature as a Langevin random magnetic field. This field will directly add up to the effective field split up earlier and is supposed to reproduce the fluctuations of the system. This field is related to the temperature with the following equation :

$$\mathbf{H_{L,i}} = \sqrt{\frac{2\alpha k_B T}{\gamma_0 M_s V}}\delta_i(t) \tag{1.38}$$

where T is the temperature of the system, $i \in \{x, y, z\}$ relates to the direction of the field and V is the volume of the magnetic layer. $\delta_i(t)$ is a gaussian random function of mean value $\langle\delta_i(t)\rangle = 0$ and of mean square root $\sqrt{\langle\delta_i^2(t)\rangle} = 1$. As a result, if we suppose that the spin-transfer torque does not modify the random Langevin field, the finite temperature LLGS equation becomes :

$$\frac{d\mathbf{m}}{dt} = -\gamma_0\mathbf{m}\times(\mathbf{H_{eff}} + \mathbf{H_L}) + \alpha\mathbf{m}\times\frac{d\mathbf{m}}{dt} - \beta I\mathcal{G}(\theta)\mathbf{m}\times(\mathbf{m}\times\mathbf{p}) \tag{1.39}$$

If the regular LLGS is usually in rather good agreement with the experiment, the introduction of a finite temperature in the model requires a different approach. In fact, the magnetization dynamics and the equilibrium states deduce from the new equation will depend on the value of the Langevin field. The analysis will then be stochastic and a statistical analysis will be needed to implement random fluctuations.

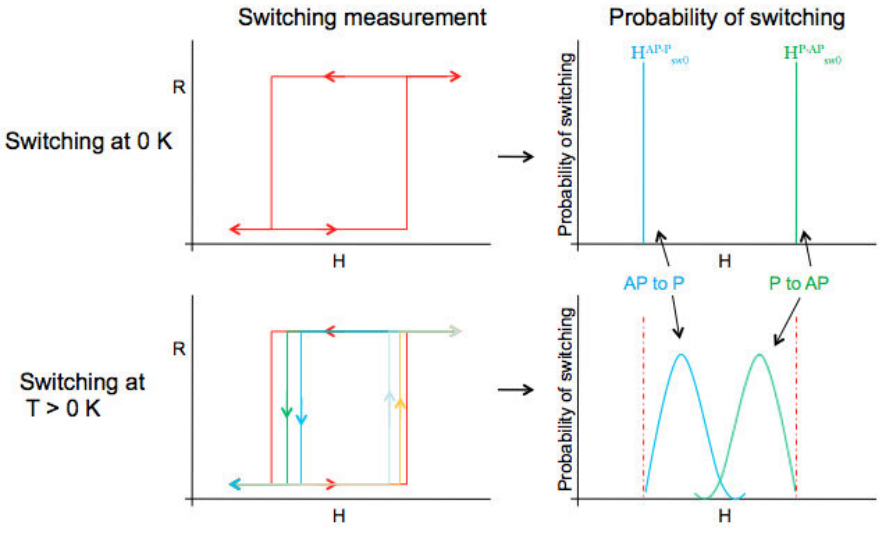

Figure 1.26: Thermal broadening of the switching field for non-zero temperature.

A direct consequence of the temperature is the broadening of the switching field for a regular spin valve (see fig 1.26). Each iteration of the equation will produce a different value for the reversal depending on the Langevin field. In the case of a ferromagnet with an uniaxial anisotropy and where the effective field and the polarizer are both collinear to its easy axis. At nonzero temperatures, there is a finite probability that magnetization reversal takes place by thermal activation over a field-dependent

energy barrier. Assuming thermal activation over a single energy barrier, at fixed temperatures and fields one can define a rate of escape as :

$$\Gamma(H) = \Gamma_0 e^{-\beta E(H)} \tag{1.40}$$

where Γ_0 is the attempt frequency, $\beta = 1/k_B T$ and k_B is Boltzmann's constant. In general, the form of the energy barrier $E(H)$ is :

$$E(H) = E_0(1 - H/H_{c0})^{\beta} \tag{1.41}$$

where $\beta \approx 3/2$[36], E_0 is the energy barrier at zero field, and H_{c0} is the zero-temperature coercive field.

The cumulative probability to remain in a metastable magnetization state under finite field, $\mu_0 H$, is given by :

$$\exp(\frac{1}{v}\int_0^H \Gamma(H')dH') \tag{1.42}$$

where v is the ramp rate of the magnetic field. This expression for the probability of not switching the magnetization at finite field has been attributed to Kurkijärvi for superconductors and fits very well to the shape of the distribution in our simple case[70] (see fig 1.27).

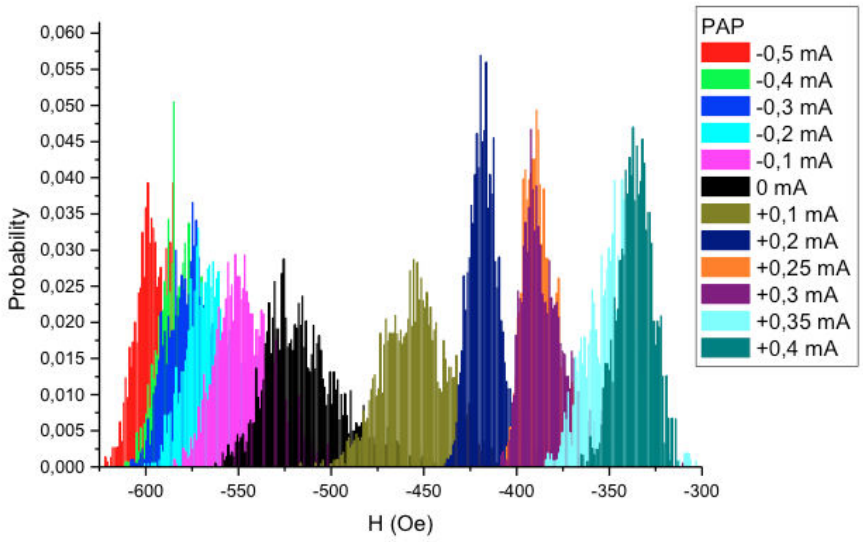

Figure 1.27: Evolution of the nucleation switching field distribution depending on the current applied for a parallel to antiparallel reversal in a 140 nm x 70 nm nanopillar spin valve.

This kind of models has been verified experimentally[70,125,204] in many cases involving magnetization reversal. However, it is valid only for quasi-static measurements because if short time current pulses are applied to the system the switching probability becomes determined by the spin angular momentum carried by the current pulse so that the switching probability is not a simple exponential anymore.

1.3.2 Temperature as a driving factor

As the interaction time and space becomes shorter and smaller, the effects will tend to divert from the quasi-static description described by the LLGS equation. In general the micromagnetic simulations

usually assume a fixed length of the magnetization vector along the trajectory. However a modeling using the LLGS equation cannot describe the processes in a magnetic system close to the Curie temperature, in general, and the phenomenon of ultrafast demagnetization, in particular. In this case, the magnetic properties (anisotropy strength and direction, damping...) are strongly modified and the magnetization magnitude is not constant in time[147].

Even if micromagnetic simulations have a hard describing the ultrafast laser excitation at very short timescale, its validity will increase as the system will recover to its stable final position. Using a comparison between time-resolved magneto-optical measurements of the laser induced magnetization dynamics and micromagnetic simulations based on the LLGS equation on Ni films[45] it was found possible to faithfully transpose the magnetization dynamics at timescale longer than 1 ps. Even if the model did not regard the details of the quenching and demagnetization directly after the excitation, it gives a good framework to describe the relaxation that comes out of it. Especially, the ultrafast excitation of the free electrons in the metal seems to dissipate using direct electron-phonon interaction after 1 ps. A large number of magnons are generated and the energy transfer "slowly" occurs via more complex magnon-magnon interaction. However this description is only valid at longer timescale and new models still need to be developed to deal with highly out-of-equilibrium systems.

Insight on atomistic simulations

Another approach to modeling ultrafast laser-induced spin dynamics in a metallic magnet is to use the LLGS equation on the atomic level[35,104,147]. Based on a quantum description of solids this approach would enable the study the dynamics of materials with complex magnetic ordering, such as ferri- and antiferromagnets, as the ones used in the rest of this thesis. Atomistic approach would also give access to the individual role of interacting electrons, spins and lattices systems that are usually connected during optically induced effects. Different dissipation processes (such as the ones presented in section 1.2.3) can be explored to understand magnetization dynamics in real systems.

The most accurate way to describe magnetic moments and exchange interactions using ab-initio considerations is based on density functional theory. But in order to unconvolute the different contributions an additional approximation is required, named the Born-Oppenheimer approximation, that make the difference between slow variables and much quicker ones. In our case, the electronic dynamics will respond almost instantaneously to the excitation whereas the spin system will be much slower. Different works[5,181] already confirm the validity of such approach and we will present here only a few steps leading to the atomistic representation of the LLGS equation but a more complete description can be found in ref[35].

In order to evaluate the dynamics of the spin system the idea is to look at the terms of the Kohn-Sham Hamiltonian[112] H_{KS} that commute with the spin operator $\hat{\mathbf{S}}$ in the equation :

$$\frac{\partial \hat{\mathbf{S}}}{\partial t} = \frac{1}{i\hbar}[\hat{\mathbf{S}}, H_{KS}] \tag{1.43}$$

In order to take into account for the current-induced effect, we have to define $\hat{j}$ the current operator and the associated spin-current operator $\hat{\mathbf{J}}$:

$$\hat{j} = \frac{\hbar}{i2m} \sum_{i}^{N} \nabla_i \delta(r - r_i) + \delta(r - r_i)\nabla_i \tag{1.44}$$

$$\hat{\mathbf{J}} \equiv \hat{\sigma} \otimes \hat{j} \tag{1.45}$$

N the individual electrons.

Furthermore, in the absence of spin-orbit coupling we separate the contribution of the magnetic field in H_{KS}, we see that $\hat{\mathbf{S}}$ commutes with all terms except for the kinetic energy expressed like that[25] :

$$-\frac{\hbar^2}{2m}\sum \nabla_{r_i}^2 \tag{1.46}$$

With this consideration, the equation 1.43 gives :

$$\frac{\partial \hat{\mathbf{S}}}{\partial t} = -\gamma_0 \hat{\mathbf{S}} \times \mathbf{H_{eff}} + \frac{1}{i\hbar}\Big[\hat{\mathbf{S}}, (-\sum_i^N \frac{\hbar^2 \nabla_{r_i}^2}{2m})\Big] = -\gamma_0 \hat{\mathbf{S}} \times \mathbf{H_{eff}} + \nabla \cdot \hat{\mathbf{J}} \tag{1.47}$$

where γ_0 is the Larmor precession frequency and H_{eff} is the effective magnetic field.

This equation would represent the motion of single isolated spins however in real systems many dissipation mechanisms exists and will influence the energy and angular momentum. The usual approach is to include a phenomenological term to the equation 1.47 take will represent the additional dampings[50,56,101,69]. Then if we use the Kohn-Sham ground state to directly represents the spin moment, the equation becomes :

$$\frac{\partial \mathbf{S}}{\partial t} = -\gamma_0 \mathbf{S} \times \mathbf{H_{eff}} + \nabla \cdot \mathbf{J} + \frac{\alpha}{m}\mathbf{S} \times \frac{\partial \mathbf{S}}{\partial t} \tag{1.48}$$

where S is the spin moments and α the damping coefficient, J the Kohn-Sham spin current.

Note that also alternative computational schemes for spin dynamics on an electronic level exist such as the time-dependent spin density functional theory[163] and time-dependent current density functional theory[214]. These approaches are promising but they are computationally much too time consuming for simulating larger systems.

Finally, we note that it is becoming more obvious that for a solution of the problem of ultrafast demagnetization a multiscale approach[109], combining ab-initio, atomistic, and micromagnetic simulations, should be developed.

Phenomenological three-temperature model

As demonstrated in the previous sections, in regular systems (i.e. based on magnetic field reversal) the dynamic of magnetism can be understood solely using magnetism interactions with a moment vector of constant amplitude. An increasing complexity is already brought by considering polarized current influence because of the non-zero temperature and angular momentum involved in the process. But the advent of ultrafast laser pulses as a magnetic probe overtakes the previous knowledge by challenging the timescale and entanglement of the whole parameters. If some of the considerations described in the LLGS equation are still valid at subpicosecond timescale, the temperature representation is a whole new issue.

The demagnetization process seems to be a continuous mechanism but in fact it is the consequence of the excitation and relaxation through the many parallel channels available in the system. Even if they are usually acting together, they start to be uncorrelated as the duration of the interaction becomes faster and faster. Usually the interactions in such a system can be qualitatively described

with the help of a single model that contains three separated but interacting reservoirs[1], namely, the electrons, lattice, and spins (see Fig. 1.28). And each of these subsystems can be seen as reservoirs for energy and angular momentum.

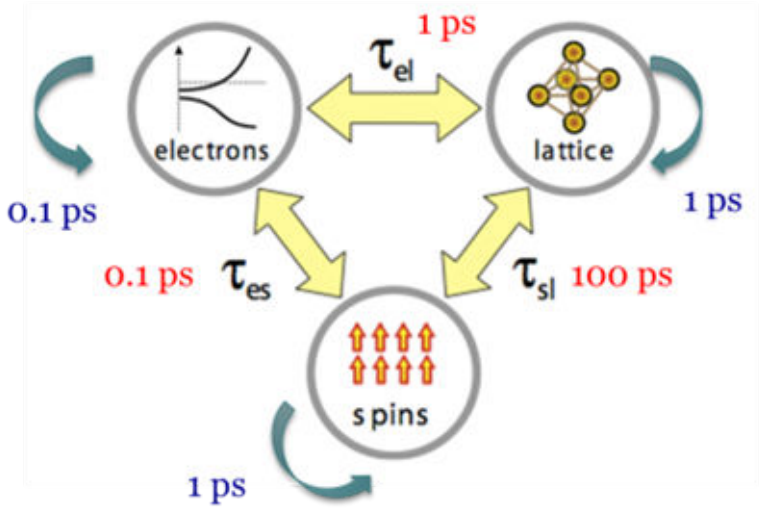

Figure 1.28: Interacting reservoirs (carriers, spins, and lattice) in the three-temperature model. Figure extracted from *Kirilyuk et al.*[109]

These three reservoirs are interconnected and will exchange heat during the recovery of the system after the ultrafast excitation. The reservoirs can be identified by their specific heat C_i and by the time constant associated with their interactions. If we consider the direct interaction between the reservoirs in quasi-equilibrium state, the following equations will be responsible for the temporal evolution of each temperature:

$$C_{el}\frac{dT_{el}}{dt} = -G_{el-la}(T_{el} - T_{la}) - G_{e-s}(T_{el} - T_{sp}) + P(t)) \tag{1.49}$$

$$C_{sp}\frac{dT_{sp}}{dt} = -G_{el-sp}(T_{sp} - T_{el}) - G_{sp-la}(T_{sp} - T_{la}) \tag{1.50}$$

$$C_{la}\frac{dT_{la}}{dt} = -G_{el-la}(T_{la} - T_{el}) - G_{sp-la}(T_{la} - T_{sp}) \tag{1.51}$$

where G_{i-j} represents the coupling between the reservoir i and$j$, T_i is the temperature of the i subsystem, and $P(t)$ is the optical pulse input.

As the coefficients G_{i-j} and C_i can be very different the temporal evolution of each subsystem is spread over different timescales. The typical response of the medium to ultrafast laser pulse can be separated in different steps. In a first time the electronic system is the only one able to react to the electromagnetic excitation.

As described in the section 1.2.3, the pulse instantaneously creates electron-hole pairs and since the electron heat capacity is typically much smaller than of the lattice, the associated temperature raises by several thousand Kelvin within the first tens of femtoseconds after excitation, while the lattice slowly increases to much lower values in a few picoseconds[58]. Following this rapid and separated increase of T_{el}, the electron-electron interaction tends to thermalize the electronic system within the first ∼50 to 500 femtoseconds. In the next 400 fs to 1 ps, the link with the lattice comes up via electron-phonon interaction. Due to the much higher heat capacity of the lattice its temperature rise is much lower and in experiments only a small static heating exists remains at longer timescale. The most

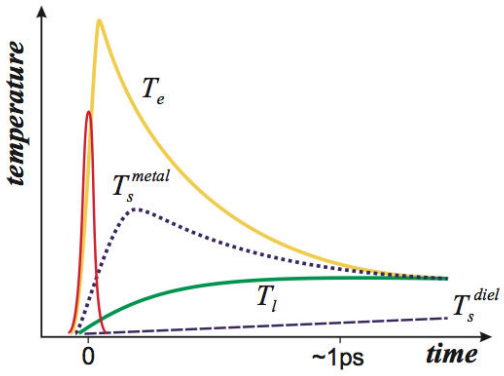

Figure 1.29: Temporal behavior of electron, lattice, and spin temperatures following excitation with a short laser pulse. The behavior of the spin temperature is shown for both strong coupling (metals) and weak coupling (dielectrics) cases. Figure extracted from *Kirilyuk et al.*[109]

questioned transfer is the one to the spin system. Originally foreseen to be on the order of hundreds of picoseconds[92], it appeared to be much faster in metals[11]. Even if the spin-lattice interaction energy is often compared to the one of the magnetocrystalline anisotropy ($\sim 100\ \mu eV$), recent works suggest a more direct coupling between photons and spins[16,117] or light coherence effects[213,127] to explain the timescale of the behaviors observed. In addition, any transfer of energy to or from the spin system must be accompagnied by a transfer of angular momentum.

The LLB equation

Using the phenomenological description of the three temperature model it is possible to have an insight of the temperature for the different subsystems during the cooling. Looking at those results, it seems clear that an ultrafast laser pulse can bring the system in a highly non-equilibrium state, in particular with an electron bath reaching thousands of Kelvin. However we mentioned earlier that the LLGS equation has a lack of validity for temperature in the vicinity of the Curie temperature. In order to extend the simulations to such temperature one can appeal for the Landau-Lipschitz-Bloch (LLB) equation. This framework basically interpolates the two aspects of the Landau-Lipschitz equation at low temperature and the Bloch equation[17] at high temperature. Thanks to this model both transverse and longitudinal relaxation terms typical from high temperature dynamics are represented.

Assuming the different heat reservoirs are acting separately due to the different timescale involved, it is possible to average out the temperature fluctuations by a stochastic magnetic field with noise correlation functions $\mathbf{H_{eff}}$. The LLB equation[62,3] obtained is :

$$\frac{\partial m}{\partial t} = -\gamma_0[m \times \mathbf{H_{eff}}] + \gamma_0\lambda_{\parallel}\frac{(m \cdot \mathbf{H_{eff}}) \cdot m}{m^2} - \gamma_0\lambda_{\perp}\frac{[m \times [m \times \mathbf{H_{eff}}]]}{m^2} \tag{1.52}$$

where γ_0 is the Larmor precession frequency and $\lambda_{\perp}$ and $\lambda_{\parallel}$ are dimensionless longitudinal and transverse damping parameters defined for temperature lower than the Curie Temperature T_{Curie} by :

$$\lambda_{\parallel} = \lambda\frac{2T}{3T_{Curie}} \tag{1.53}$$

$$\lambda_{\perp} = \lambda\left[1 - \frac{T}{3T_{Curie}}\right] \tag{1.54}$$

and for $T > T_{Curie}$, we will have $\lambda_{\perp} \Rightarrow \lambda_{\parallel}$.

Some of the aspects held by this formalism have already been investigated, such as the link between damping parameters and temperature or effective field [25,50], but in general the LLB equation is in rather good agreement with the more fundamental atomistic simulations. The main advantage is that it required a much lower calculation time and can be performed on micrometer-size systems.

1.4 Theoretical models

Helicity dependent behavior

Among the different studies based on the ultrafast demagnetization of magnetic material it is the work from Kimel et al.[106] published in 2005 that awaken magnetism society's curiosity about the role of helicity in the dynamic subsequent to an ultrafast laser pulse. On a DyFeO3 sample they observed that after the excitation the magnetization precesses with a different signature depending on the polarization used (see fig 1.30). For the first time an ultrafast and non-thermal effect of light was found in magnetism. In addition the interaction of the optical pulses with the magnetization were found equivalent to a magnetic field pulse with an amplitude of 0.3T and a temporal extend of 200 fs acting on the magnetization through the inverse Faraday effect.

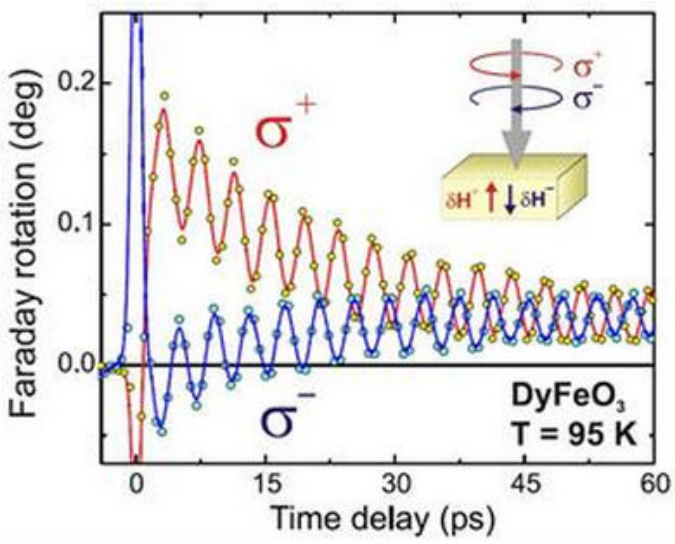

Figure 1.30: Laser induced spin oscillations in DyFeO3 probed by the magneto-optical Faraday effect. The circularly polarized pumps of opposite helicities excite spin oscillations of opposite phase. Inset shows the geometry of the experiment. Vectors $\partial H+$ and $\partial H-$ represent the effective magnetic fields induced by right-handed and left-handed circularly polarized pumps, respectively. Figure extracted from *Kimel et al.*[106]

The next milestone was obtained in the same group in 2007 by Stanciu et al. when then demonstrated the full stable switching of a GdFeCo thin film with a ultrafast laser with circular polarization[186]. Not only the switching was deterministic along with the helicity of the pulse but the reversal occurs with a single pulse of width of 40 fs at half maximum. On the one hand the linear polarization just demagnetizes the sample and leaves a multidomain pattern whatever the starting saturation. On the other hand the right (left) helicity create a domain of opposite magnetization for one (the other) of the two saturation. Very similarly to the process used nowadays in hard disk drives they swept the beam over the sample and depending on the helicity a controlled domain pattern of a dozen microm-

eter in size can be imprinted in the film (see fig 1.31). This so-called all-optical switching directly offered new perspectives for the magnetic recording industry with the possibility to get rid of any external magnetic field in emerging technology such as HAMR (see section 2.2.4).

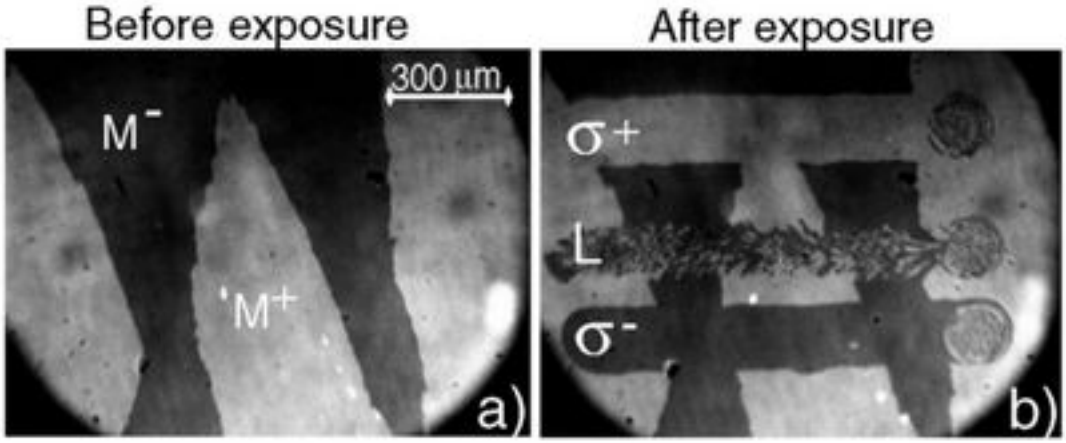

Figure 1.31: The effect of ultrashort polarized laser pulses on magnetic domains in $Gd_{22}Fe_{74,6}Co_{3,4}$. (a) Magneto-optical image of the initial magnetic state of the sample before laser exposure. White and black areas correspond to up (M^+) and down (M^-) magnetic domains, respectively. (b) Domain pattern obtained by sweeping at low speed ($\sim 30\ \mu m/s$) linear (L), right-handed (σ^+), and left-handed (σ^-) circularly polarized beams across the surface of the sample, with a laser fluence of about 11,4 mJ/cm^2. The central area of the remaining spots at the end of each scan line consists of small magnetic domains, where the ratio of up to down magnetic domains is close to 1. Figure extracted from *Stanciu et al.*[186]

Parallely some insight in the magnetic properties induced by ultrafast laser pulses were obtained for the GdFeCo samples. This work[187] emphasizes the role of the compensation temperature in such ferrimagnetic alloys and the possible link of angular momentum transfer especially with the previous observations done in the field. However if this paper was the first one trying to fill the gap between the microscopic observation of the all-optical phenomenon and the macroscopic properties of the materials involved there was still no direct explanation of the evolution of such kind of system.

In the following years the first simulations[208] of the phenomenon were focused on the key ingredients required for the all-optical switching in GeFeCo. It appeared that there is some similarities between a high electron temperature associated with an rapid magnetic field and the behavior observed during the experiment. The energy of the pulse first quenched the system to a low magnetization value near the Curie temperature after 500 fs then the effective magnetic field due to the inverse Faraday effect can switch the magnetization thanks to the tremendous value of up to 20T applied. Since the sign of the field only depends on the pulse chirality the effect is different for the two helicities. This reliable switching only occurs within a narrow range of parameters for the laser pulse (see fig 1.33) where the combination of high electronic temperature and the later rapid quenching is optimal. If the system is out of this window the magnetization just restores back to its initial state.

Even if this work gives a model that fits to the experiment available at this time, the exact role of the balance of angular momentum in the reversal needs to be understood and further work are required. In particular, it is generally agreed that the simple assumption of a direct spin transfer from photon spin to the magnetization is not the solution[116], suggesting that the atomic lattice may play a role.

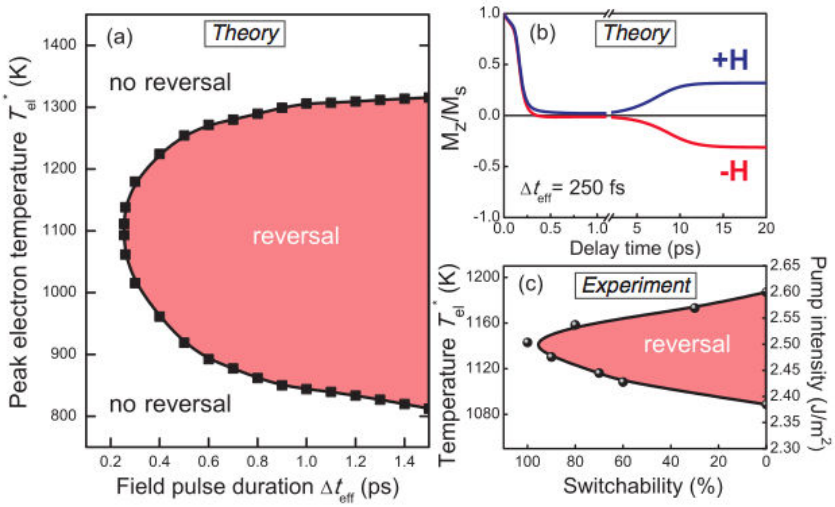

Figure 1.32: (a) Phase diagram showing the magnetic state of the (30 nm^3) volume achieved within 10 ps after the action of the optomagnetic pulse with parameters $H_{eff} = 20T$. (b) The averaged z components of the magnetization versus delay time as calculated for 250 fs magnetic field pulses $H_{eff} = 20T$ and $T_{el}^* = 1130K$. (c) Switchability versus the pump intensity for $Gd_{22}Fe_{68,2}Co_{9,8}$ at room temperature. Figure extracted from *Vahaplar et al.*[208].

Helicity independent behavior

Still working on the same GeFeCo alloy further experiments[165] permitted to probe the two different sublattices using X-Ray magnetic circular dichroism (XMCD) on an ultrafast timescale. Using linearly polarized pulses it turns out that the Gd and Fe atoms both demagnetize but with different time constant. If the final state occurs after several picoseconds and corresponds to the same antiferromagnetically coupled spin structure as before the pulse, the experiment reveals that during the reversal the two individual moments point for some time in the same direction. This particular state is related to the fact that the Fe moments are demagnetizing four time faster than the Gd moments ($\sim$ 100 fs compared to $\sim$ 430 fs). This so-called transient ferromagnetic-like state is even more surprising that the two sublattices are strongly exchange coupled in thermal equilibrium.

In 2012 a final experiment[152] was finally focusing much of the attention when the demonstration of a deterministic reversal was made possible using pulses with a linear polarization. Not only this results contradicts with the initial helicity dependence but in addition the switching was toggled by each consecutive pulse. Each time a pulse was applied the magnetization reverses (see fig. 1.34).

Three main different interpretations were reported to explain the switching occurring in this experiment : the first one is directly derived from the previous optomagnetic model developed by Vahaplar et al.[208,207], the second one is based on the multi-sublattices structure[139] of the ferrimagnetic GdFeCo, while the last one find out an origin directly in the magnetic dichroism[175] of the material. The first one only relates to the maximum electronic temperature reached by the system and characterizes the reversal by its fast recovery and a nearly quenched state. On the contrary Mensink et al. links the reversal to the exchange between the two sublattices that will under certain out-of-equilibrium circumstances favor a switching of the two sublattices. Using a different approach Khorsand et al. describe that the switching can occur for any polarization as long as the amount of energy actually absorbed by the material is sufficient to switch the magnetization (see fig 1.35).

Even if different interpretations are still debated in the field the most important question that still needs to be addressed is the origin of the lever driving the switching phenomenon. The separation or

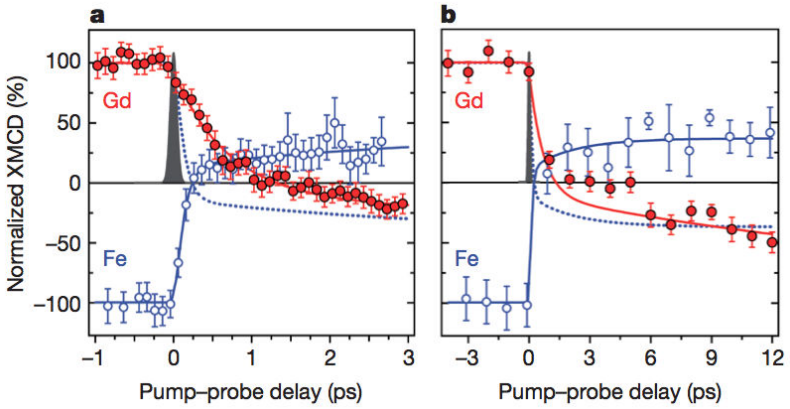

Figure 1.33: Element-resolved dynamics of the Fe and Gd magnetic moments measured by time-resolved XMCD with femtosecond time-resolution. a, Transient dynamics of the Fe (open circles) and Gd (filled circles) magnetic moments measured within the first 3 ps. b, As a but on a 12 ps timescale. Error bars of the experimental data represent the statistical standard error. The measurements were performed at a sample temperature of 83 K for an incident laser fluence of 4.4 mJ/cm^2. Experimental time resolution of 100 fs is depicted by the solid Gaussian profile. The solid lines are fits according to a double exponential fit function. The dashed line in both panels depicts the magnetization of the Fe sublattice taken with the opposite sign. Figure extracted from *Radu et al.*[165]

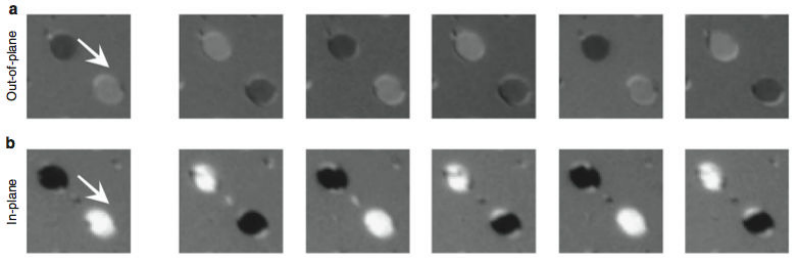

Figure 1.34: XMCD images at Fe L3 edge of 2 μm wide $Gd_{25}Fe_{65.6}Co_{9.4}$structures. (a) Images of microstructures with out-of-plane anisotropy, magnetized perpendicular to the sample plane. The first image in (a) shows the initial state of the microstructures where the magnetization of the darker structure points down while the magnetization of the brighter one points up. The next image is taken after excitation with a single linearly polarized laser pulse and shows that the magnetizations of both elements are reversed. This reversal occurs after every laser pulse, as can be seen in the subsequent images in (a). (b) Images of microstructures with in-plane anisotropy. The bright and dark areas correspond to magnetization directions in the plane of the sample pointing parallel or anti-parallel to the X-ray direction. The subsequent images are taken after each excitation with a single linearly polarized laser pulse demonstrating the reversal of the magnetization. The X-ray direction is indicated by an arrow and the structures have a size of 2 micrometers. Figure extracted from *Ostler et al.*[152]

universality of the all-optical phenomena probably rely on the origin of the laser-magnetism interaction so further investigation are required and will enter the scope of this thesis. Interestingly non of those model attempt to make some predictions about the limitations of the effect and they all seem to be focused on the original GeFeCo structure or slightly extend to the associated ferrimagnets (TbFe, TbCo...). In contrary Mentink et al.[139] suggests that a similar behavior could even occur in ferromagnets with multiple sublattices in the case of a sudden decrease of the electron temperature. Such kind of perspectives were ideal for the type of study that was foreseen in this thesis.

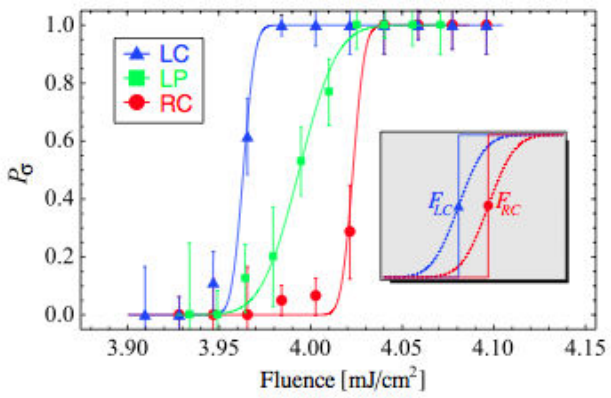

Figure 1.35: Switching probability P_σ as a function of the fluence at $\lambda = 700$ nm for three different polarizations. Inset: illustration of the switching probabilities in case of zero (solid) and non-zero (dashed) laser fluctuations. Figure extracted from *Khorsand et al.*[175].

Chapter 2

Samples and Experimental Set-Up

Introduction

As discussed in chapter one the possibility to switch magnetization using light is very interesting both for experimental and theoretical investigations and for potential applications. The mechanism underlying the AO-HDS is still largely unknown and new approaches and study of the phenomenon are needed. The situation at the beginning of my PhD work was that a very small number of material presented all-optical switching signature. Only a few GdFeCo ferrimagnetic alloys had shown AO-HDS we then decided to start a material study to determine which material have the same kind of effects.

Thanks to the possibilities of the laboratories visited during this thesis I was able to grow and characterize thin films of different types. For this study we have first covered a whole range of ferrimagnetic materials, starting from the original GdFeCo alloys to more exotic rare-earth transition metal alloys. We further manage to obtain synthetic ferrimagnetic synthetic multilayers mimicking the properties of intrinsic ferrimagnets but without the rare earth-base of it. To achieve a full overview of the fundamental bricks of magnetism we even oriented our prospects to some ferromagnetic materials available. The last step corresponds to the investigation of state-of-the-art granular media that are structurally much different from the previous research done. In a second time we will describe the ultrafast laser setup used to study the AO-HDS. A particular emphasize will be put on the pulse build-up stage and the imaging system that once combined define the range of observations that can be performed on our samples. Due to the complexity of the possible observations a careful description of the main behaviors and drawbacks of the setup will be highlighted. The main goal of this study is to help understand the mechanism behind AO-HDS. Indeed in changing the RE materials we are tuning the complex AO-HDS phenomenon and probe its limits.

2.1 Thin Films Deposition

With the increasing development of nanotechnologies the need for tailored film deposition is growing every day. Among the many different ways to deposit materials such as metals, ceramics or plastics onto a surface (in our case a substrate) the sputtering method has become one of the leading technology to grow thin films. Sputtering is a physical vapor deposition (PVD) process that deposits materials by ejecting atoms from a target of the pure element and condenses them back onto a substrate. As the deposition process requires the formation of a plasma the whole method is done in a high vacuum environment. during my PhD I have grown more than 1000 samples using this technics. I used a first AJA sputtering system at UCSD and I thereafter installed a new one in Nancy to continue the

development of this project.

2.1.1 Basics on Sputtering Deposition

Even if the actual mechanisms at play during the deposition via sputtering is rather complex, the basic idea of operation can be described in a few intuitive steps. The first idea is to create a gaseous plasma (typically made of inert gas ions such as Argon Ar^+) and then to accelerate the ions into some source material desired to be deposited (also called "target"). To do so electrically neutral Argon atoms are introduced into a vacuum chamber at a pressure of 1 to 10 mTorr. A DC voltage is placed between the target and substrate which ionizes Argon atoms and creates a plasma, hot gas-like phase consisting of ions and electrons, in the chamber. This plasma is also known as a glow discharge due to the light emitted. These Argon ions are now charged and are accelerated to the anode target. The forceful collision of these ions onto the target ejects atoms in the form of neutral particles - either individual atoms, clusters of atoms or molecules into the vacuum space. As these neutral particles are ejected they will travel in a straight line unless they come into contact with nearby surface and start to condense into a film. As more and more atoms associate on the substrate, they begin to bind to each other at the molecular level, forming a tightly bound atomic layer. In addition electrons released during Argon ionization are accelerated to the anode substrate, subsequently colliding with additional Argon atoms, creating more ions and free electrons in the process, continuing the cycle. One or more layers of such target atoms can be created at will depending on the sputtering time, allowing for coating of precise layered thin-film structures.

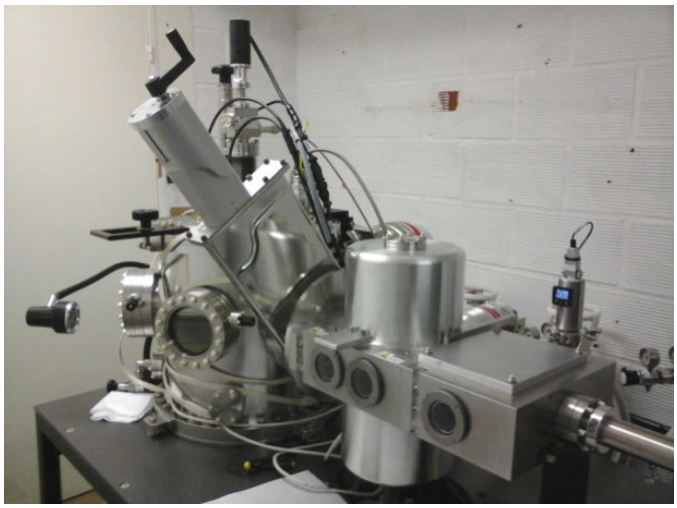

Figure 2.1: Picture of the AJA Orion system used for the deposition at the IJL and CMRR

Magnetron Sputtering

Among the different ways to enhance the sputtering process, the magnetron sputtering was the one chosen for most of the thin films deposition achieved during this thesis. The main difference between this one and a basic DC sputtering system described above is the addition of a specific magnetic field configuration near the target area. In order to increase the ion density in the vicinity of the target, the system is equipped with two permanent magnets of opposite polarity located below the target (see fig 2.35). They create a magnetic field B parallel to the target surface and orthogonal to the electric field E used to ionize the argon. The combination of these two fields gives rise to field lines that

trap the secondary electrons. The Lorentz force induced causes a helical movement of the electrons. The advantage of this is that the plasma is confined to an area near the target, without causing damages to the thin film being formed. Also, electrons travel for a longer distance, increasing the probability of further ionizing Argon atoms. This tends to generate a stable plasma with high density of ions. More ions mean more ejected atoms from the target, therefore, increasing the efficiency of the sputtering process. The magnetron allows to maintain the discharge for lower working pressure, therefore improving the quality of coatings.

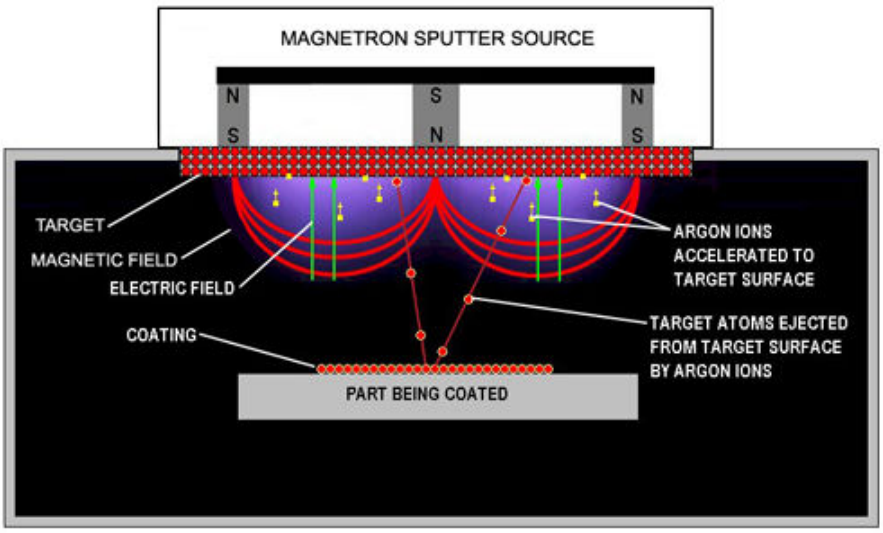

Figure 2.2: Scheme of a magnetron sputtering system. Figure extracted from Strand et al.[184]

Orion Sputtering Systems

Most of the films presented in this thesis have been deposited using the sputtering technology. To do so two Orion System built by AJA International with the same characteristics have been used. A brief overview of the capabilities of this system will be presented here.

The system is a 8-target sputtering system using planar magnetron sources improvement. The particular configuration of the sources enclosed in a chimney with narrow source shutter gap minimizes the cross contamination between sources. Both RF, DC and DC-pulsed regime can be used to generate the plasma and the several power supply allow the co-deposition of material. The system can handle substrates up to 4 inches in diameter and the substrate holder allow simultaneous, rotation, heating, RF bias (for in-situ substrate pre-cleaning) and deposition at up to 850 °C in suitable sputtering environment (600 °C in a pure Oxygen environment). Stability is to within ± 1 degree C, Deposition uniformity over 4" is better than ±2 % and temperature uniformity is better than ±1 %. A load lock chamber and cassette allows the samples to be removed and changed without venting the chamber. The cassette can hold up to 6 substrates holders and up to 4" wafer sizes can be accommodated in the system. . Pumping of the main chamber are thanks to a turbo-pump (capable of pumping O2) achieving below 5.10^{-8} Torr ultimate base pressure. A VAT gate valve is used for process pressure control independent of gas flow. Flow rates are controlled with standard mass flow controllers. Argon is used for the sputter gases, with N_2 and O_2 used for reactive sputtering. The system is recipe driven and computer controlled for reproducible results.

2.1.2 Properties measurements

Magnetic measurements are essential in characterizing the magnetic properties of materials used for various modern applications. However the technique that is best suited to any given application depends critically on the materials that are being measured, the parameter space (field, temperature, orientation of the field with respect to the sample) over which measurements are to be performed, as well as practical considerations (sensitivity, measurement speed). During this thesis we mostly used two characterization tools that allow for a quick but useful insight on the properties of our materials : VSM and MOKE magnetometry. The principles of the two will be qualitatively described here. This account is not intended to be complete and rigorous, but to provide an overview for the reader.

Vibrating Sample Magnetometry

The Vibrating Sample Magnetometry (VSM),originally developed by Foner[60], is based on vibrating a sample within a uniform magnetic field, inducing an electric current in suitably placed sensing coils. The resulting voltage induced in the sensing coils is directly proportional to the magnetization of the sample. The magnetic field may be generated using conventional electromagnets for field strengths of $\sim$ 3 T as well as systems employing superconducting magnets to produce fields to 16 T. In general VSM's are widely used in laboratories since magnetic properties can be measured for a diverse range of sample sizes and configurations, i.e., powders, solids, single crystals, thin films, and liquids, and because they are particularly well suited to allow precise and quick measurements in different configuration and depending on the temperatures. During this thesis two different equipments where used : a 3 T Versalab system and a 7T Magnetic Properties Measurement System (MPMS©3) equipment, both developed by the Quantum Design company (see Fig. 2.3 (a) and (b)).

The Versalab is based on regular sensing coils so is limited by a noise floor of typically 10^{-6} emu which corresponds to a sufficient sensitivity for most if the magnetic materials measured during this thesis. On the other side the MPMS©3 employes a superconducting quantum interference device (SQuID) sensor that measures the magnetic properties of materials using quantum mechanical effects with a set of superconducting detection coil circuitry. Theoretically, SQUID-based VSM are capable of achieving sensitivities of 10^{-12} emu, but practically they are limited to 10^{-8} emu, because SQUIDs also pick up environmental noise.

Finally the VSM is an "open loop" measurement in that the sample and field source do not constitute a closed flux line loop. Hence the measured parameters must be corrected for demagnetization effects to yield the true intrinsic material parameters most often of interest for magnetic materials. In addition all the hysteresis loops plotted in this thesis always correspond to the data corrected from the intrinsic diamagnetism of the substrates used.

MOKE Magnetometry

Magneto Optical effects in magnetic materials arise due to the anisotropy of the optical properties in the materials. The source of this optical anisotropy relates to the local magnetization that alters the state of linearly polarized light which is reflected off the magnetic surface. This makes it particularly useful in the study of surface magnetism since it is highly sensitive to the magnetization within the skin depth region, typically 10-20nm in most metals[153]. These effects which were first described by John Kerr in 1887 are analogous to the Faraday effect where the polarization of the light is rotated through a transparent material subjected to a magnetic field and that will be presented in a following

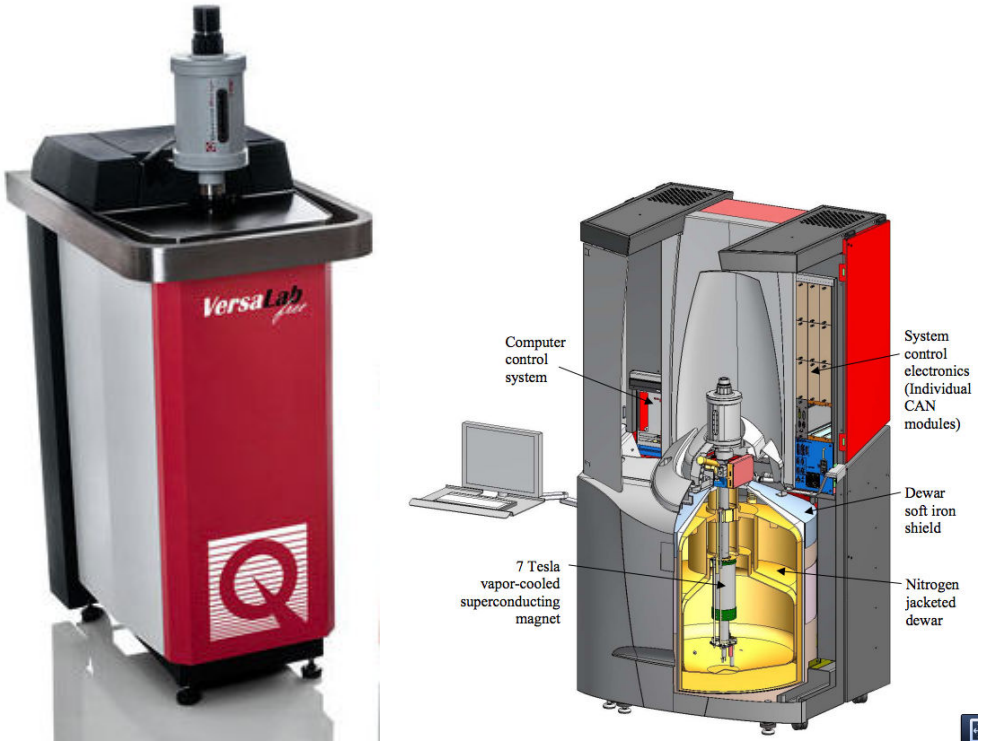

(a) (b)

Figure 2.3: VSM magnetometer used during this thesis : (a) 3 T Versalab system. (b) 7T MPMS©3 using a SQUID system for magnetization measurements.

section. The effect has been utilized for a long time to obtain hysteresis loops or domain images and is a relatively simple technique to implement.

During this thesis we used a commercially available MOKE system which allow for an automation of the measurement in the case of sample of big dimensions. Light was provided by an He-Ne laser (λ = 633 nm) in a polar configuration. The polarization of the beam was controlled by a linear polarizer prior to the sample surface and the reflected beam light was analyzed using an analogue polarizer coupled to a photodiode where the reflected intensity was measured. In most of the case the thickness of our films is small enough to consider that the MOKE magnetometer is sensing the whole magnetism of our samples. This type of measurement was done as an additional characterization of our films especially for the search of the compensation composition, but as it does not give access to the quantitative saturation magnetization we preferred the VSM measurements when available.

2.2 Magnetic properties of thin films

Most of the pioneer work from Stanciu et al.[188] on the all-optical helicity-dependent switching were obtained on a GdFeCo alloy with a very specific composition. One of the possibilities to probe even further the underlying mechanism corresponds to make the link between the magnetic properties of a wide range of materials and how they behave under ultrafast pulses. To do so we will quickly remind some of the properties of interest for the four different types of materials explored during this thesis (see Fig. 2.4) : the rare earth-transition metal combination, the synthetic ferrimagnets, the Co-Pd/Pt/Ni multilayers and the $FePt$-L_0^1 granular media. The study of those many different materials gives us a wide range of tunability of the magnetic properties and especially the perpendicular anisotropy to probe the all-optical switching limits.

Deposition conditions

All Samples were prepared on glass substrates using dc-powered sources from pure elemental targets of 2" diameter. The chamber was evacuated with a set of rotary and turbopump to below 1 x 10^{-7} Torr prior to sputtering and the Ar gas pressure during sputtering was typically 3x10^{-3} Torr. The thickness and uniformity of each layers were controlled by the deposition rate (0.5-2 A/s) previously calibrated and the rotation speed ($\sim$ 40 rpm) of the substrate. Magnetic properties were studied by a vibrating sample magnetometer that has been described in the previous sections.

2.2.1 RE-TM based thin films

Rare earth (RE) transition metal (TM) systems often act as a model system in magnetism because of the wide tunability of their magnetic properties[132,75,76]. In addition to a favored out-of-plane anisotropy RE-TM alloys also show good magneto-optical properties[93] that promote them as a good candidates for ultrafast optics studies. In particular this kind of systems have been widely explored in that past decades by the magnetic recording industry with the initial goal to develop magneto-optical recording technologies[197,75,76,151,31].

Origin of magnetism in RE-TM alloys

RE-TM final magnetization originates from the microscopic interaction between its individual components.

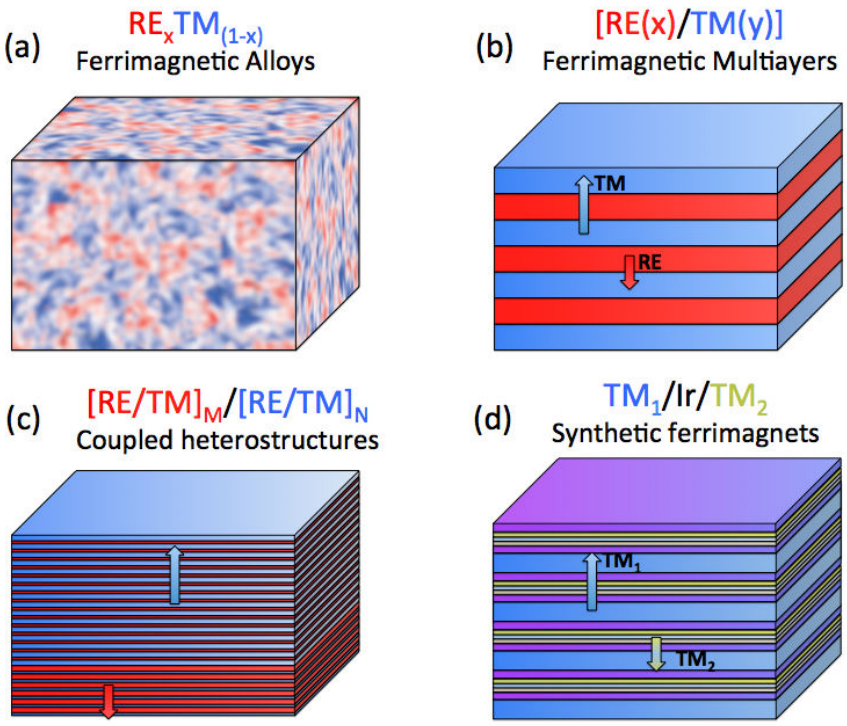

Figure 2.4: Schematic of the four types of ferrimagnetic samples that have been studied and exhibit AO-HDS. (a), Thin-film RE-TM alloys. (b), $[RE/TM]_N$ multilayers. (c), Exchange-coupled $[RE/TM]_N$ /$[RE/TM]_M$ heterostructures. (d), SFI made of two TM layers antiferromagnetically coupled through 0.4 nm Ir interlayers. Each type of magnetic structure has shown either AO-HDS or thermal demagnetization depending on the thickness, layer structure and/or atomic concentration of the sample.

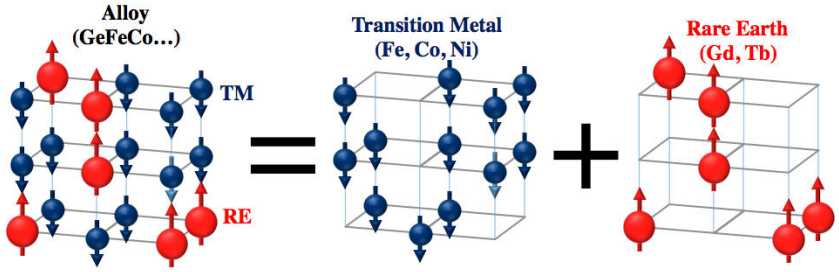

Figure 2.5: In the case of heavy rare-earth such as Gd and Tb, the net magnetization of a RE-TM alloy can be decomposed as the RE and the TM counterpart with opposite directions.

RE-TM alloys consist of two coupled magnetic sublattices, namely the RE and TM sublattice that add up to form the net magnetization of the material. The first building block consists of a ferromagnetic transition metal such as Co, Fe or Ni that is inter alia characterized by a high Curie temperature and a magnetism originating from the 3d shell. The second element is picked in the lanthanide family. The latter can be subdivided into two parts that are called the light RE and the heavy RE depending on the filling level of their 4f-shell. If this 4f-shell is less than half filled (e.g. for Sm, Pr, Nd and Eu) the element is a light RE that tends to link with TM through a ferromagnetic coupling. In the contrary a typical antiferromagnetic coupling is occurring for heavy RE (e.g. Gd, Tb, Dy, Ho, Er and Tm)[202,111] which are above the half-filling threshold. During this thesis we investigated only Gd- and Tb-based systems so the coupling can always be considered antiferromagnetic in the ground state.

RE and TM belong to two different class of magnetic materials thanks to the origin of their magnetism. On the one side in TM the magnetic moment is only carried by the 3-d electrons and its a direct exchange interaction that creates the ferromagnetic coupling[193]. On the other side the RE have both a contribution from the 4f and the 5d electrons. However the 4f-electrons are usually attributed most of the weight of magnetism as they approximately account for 90 % of the absolute value of this type atom. In alloys the atomic environment is slightly modifying this structure but the final state can be as a raw approximation considered the same in alloys and pure elements[202].

The microscopic coupling in RE-TM alloys is a superimposition of three main contributions. The TM-TM coupling due to the itinerant magnetism in 3d metals that creates a rather strong coupling. The direct antiferromagnetic coupling between 5d RE and 3d TM electrons assisted by the indirect coupling between 4f RE et 3d TM that account for the intersublattice connection between RE and TM[75,76,24,59]. And the final RE-RE coupling that is weaker than in 3d TM but is still responsible for the ferromagnetism in RE. It is generally possible to make the following statement regarding the intensity of the different coupling even if it will depend on the combination of elements[151,198] :

$$J_{TM-TM} > J_{TM-RE} > J_{RE-RE} \tag{2.1}$$

Compensation of sublattices

The heavy RE-TM ferrimagnets contain two distinct sublattices whose individual moments are coupled antiparallel to each other. As a consequence the total magnetization will be the algebric sum of the two magnetic subunits. Besides the magnetization of RE and TM evolve differently with the temperature, so the total magnetization will have the same nature. As the magnitude of the two sublattices moments is modified the net magnetization is changing too. An interesting feature is for certain composition the existence of a characteristic temperature, called T_{Comp}, where the net magnetization of the alloy moments cancel out. In this circumstances the individual RE and TM atoms will be magnetized but the global system will have a zero total magnetization (see fig 2.6) because of the temperature dependence of the magnetization of the two sublattices.

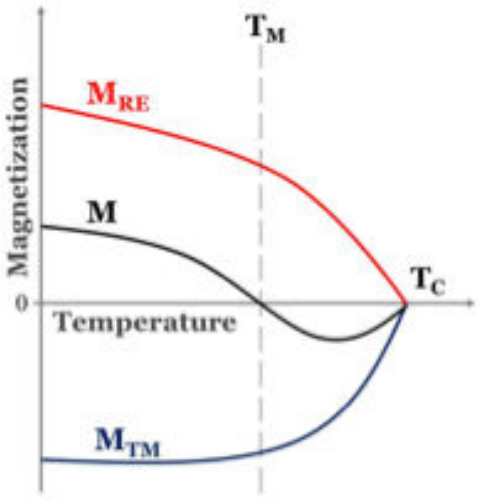

Figure 2.6: Temperature-dependence of the sublattice magnetizations M_{RE} and M_{TM}, and the net magnetization M. The magnetic compensation temperature T_M occurs when the two different sublattices compensate.

On both sides of the compensation temperature there is an unbalance between the two sublattices

(see fig 2.8). In this two configurations an external magnetic field is always orienting the stronger subsystem and the other one just has to stick to the opposite direction due to the antiferromagnetic coupling. Usually the RE has a stronger magnitude at lower temperature than the TM, and it is the contrary for temperatures higher than the compensation temperature so it gives the following situations:

$$T > T_{Comp} \rightarrow M_{TM} > M_{RE} \rightarrow M_{tot} \sim M_{TM} \tag{2.2}$$

$$T = T_{Comp} \rightarrow M_{TM} \sim M_{RE} \rightarrow M_{tot} = 0 \tag{2.3}$$

$$T < T_{Comp} \rightarrow M_{TM} < M_{RE} \rightarrow M_{tot} \sim M_{RE} \tag{2.4}$$

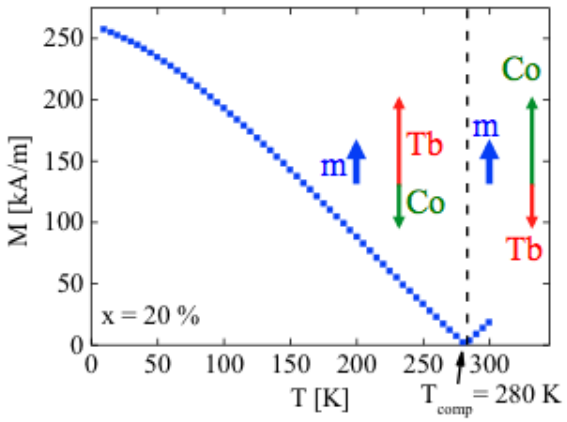

Figure 2.7: Figure showing the compensation temperature (around 280K) for a typical CoTb sample. In inset we can see the dominating sublattice on both side of the compensation.

The net magnetization is not the only parameter that depends on the interaction of the two sublattices. Indeed a ferrimagnets structure is responsible for a particular behavior of its intrinsic angular momentum. As the angular momentum A_i of each of the two sublattices is proportional to the magnetization $\mathbf{M_i}$ by the following formula[193] :

$$|\mathbf{M_i}| = -g_i \frac{\mu_B}{\hbar} A_i \tag{2.5}$$

where the i coefficient stands for either the RE or the TM atoms, μ_B the Bohr magneton and $\hbar$ the Planck's constant. The g-factor depends on the spin (S) and orbital momentum (L) quantum number of each type of atoms. In general the angular momentum compensation is slightly ($\sim$ 50 K) lower than the net magnetization compensation. We will come back to the optical behavior in the last section of this thesis.

Another consequence of this vanishing magnetization in the vicinity of the compensation temperature is the divergence of the coercive field. Indeed a very low total magnetization means that only a very small torque $\mathbf{\Gamma}$ can be created upon the application of an external field H following the equation :

$$\mathbf{\Gamma} = \mathbf{M} \times \mathbf{H} \tag{2.6}$$

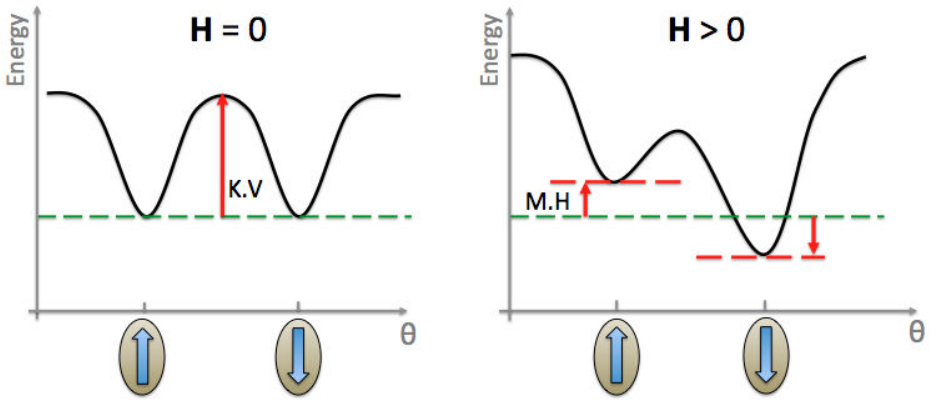

Figure 2.8: Modification of the energy landscape upon addition of an external magnetic field for a magnetic particle with uniaxial anisotropy.

Influence of composition

As the origin of the net magnetization in RE-TM alloys mostly stems for the balance between the two different types of atoms it is obvious that the magnetic properties of this kind of alloys will depend on the composition. By changing the composition many parameters can be explored ranging from the net magnetization, the compensation temperature, the damping parameter, the individual amplitude of the moments for the RE and TM to the Curie temperature. Some of them where already explored[109,138,71] before the beginning of this thesis, for example some correlation between the temperature dependence of the magnetization and the effects observed after laser excitation were highlighted. Therefore we decided to focus on the material and try to correlate their magnetic properties with AO-HDS.

In Fig. 2.9 (a) we can see the typical hysteresis loops obtained varying the Gd concentration in the GdFeCo samples while keeping the ratio between Fe and Co equal to 2. As this measurements were obtained using a MOKE setup with an He-Ne illumination we can consider that this curves mainly represent the TM response because of the position of the Fermi level for both RE and TM elements. As a consequence we observe the typically inversion of the hysteresis while passing through the composition where the two sublattices compensate at room temperature. On Fig. 2.9 (b) we summarized the evolution of the coercitive field with the composition with an emphasize put on the divergence of the value that is characteristic for the compensation composition as described above.

Since the antiferromagnetic coupling is strong between the RE and the TM the reversal of one magnetic sublattice leads to the reversal of the other as can be seen using element specific technic such as XMCD.

Variation of thicknesses

Even if the magnetic properties are mainly due to the choice of the RE-TM combinations the role of thicknesses and stacking could not be exclude either. In particular we explored the contribution of the buffer and capping layers and the influence of the magnetic layer thickness for the GdFeCo series (see Fig. 2.11).

It might be hard to compare the level of saturation of the samples as MOKE measurements mostly give qualitative values, but it is still possible to compare the value of the coercitive fields. As expected

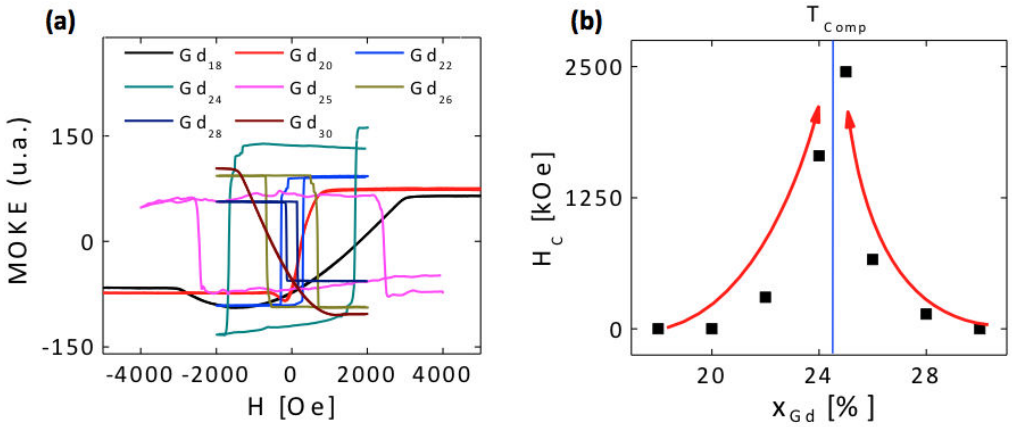

Figure 2.9: (a) Hysteresis loops of the GdFeCo samples with various composition used during this thesis measured by MOKE. (b) Composition compensation at room temperature deduced by the divergence of the coercive field ($\sim$ 25 %).

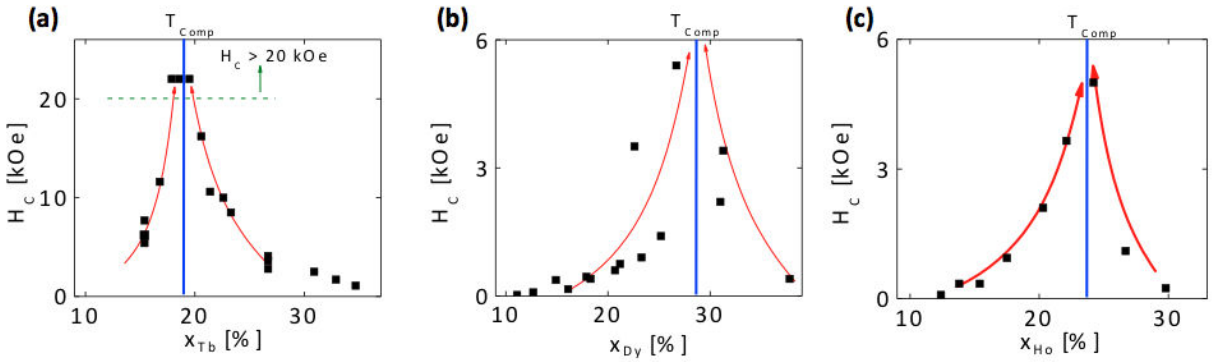

Figure 2.10: Different measurements of the coercive field varying the composition of RE-TM alloys (a) Tb, (b) Dy, (c) Ho. The approximate compensation temperature is indicated with T_{Comp}.

the change in the thickness of the capping layer is not changing a lot the material properties of the sample compared to a change in the buffer layer. Indeed the underlayers are partially responsible for the crystal orientation of the magnetic layer so depending on its thickness the disorder and phases induced can change and can be seen on the modification of the coercive field. Furthermore we can see that the thickness of the GdFeCo layers is responsible for part of the properties too. However we can see that for the range of thickness explored the coercive field stabilizes so in all cases we will try to stay in this constant part in order to avoid any variability out of the material composition.

Magnetic Properties of RE-TM multilayers

In order to extend our study to the influence of the structural ordering of the samples we decided to create some multilayers with the same compositions as previous alloys. Indeed in this kind of structures the segregation of atoms will affect the magnetic properties such as the exchange coupling, anisotropy and magnetization. From the isotropic structure of the alloy to the anisotropy of the mutilayers the exchange coupling will go from uniform to non-uniform.

In the case of GdFeCo multilayers shown in Fig. 2.12 we separated only the RE and the TM part without any special care to the structure of Fe and Co. On the figure we can see that the properties vary a lot with the relative thickness of the layers. Even if they have the same global composition important changes occur in the magnetic properties. Especially we see that there seems to be a

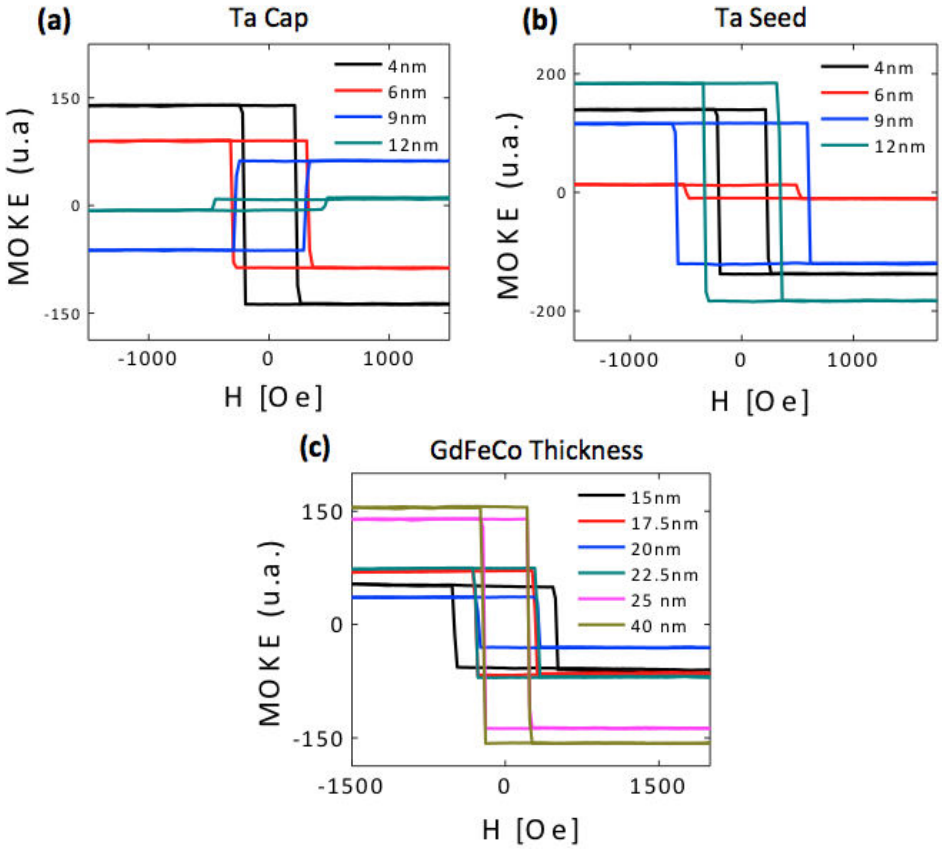

Figure 2.11: Influence of the different layer thicknesses on the reversal properties measured by MOKE technic. Effect of (a) the Ta capping layer, (b) the Ta seed layer, (c) the thickness of the magnetic layer.

maximum thickness for the Gd or the FeCo above which the perpendicular magnetization disappears illustrated by the flat result for the hysteresis loop performed on the [Gd(9,15)/FeCo(10)] sample. Additionally we can notice that the hysteresis that is sometime inverted meaning that the samples are bouncing from RE- to TM-rich for the net magnetization. In our case this would mean that depending on the layer structure the compensation temperature is sometimes higher than the room temperature and sometimes lower. If we did not manage to directly find the relation between T_{Comp} and the layout of the sample, we could still use this observation as a way to have the same number of atoms of each type and observe the influence of the position of the T_{Comp} on the laser excitation.

Besides we used the same approach on the TbCo samples but with the idea in mind that Tb is know to induce much stronger perpendicular anisotropy than Gd due to its high orbital angular momentum. In this context it is possible to grow much thicker layers for the same multilayer structure[53] and still maintain the perpendicular orientation. In Fig. 2.14 perpendicular anisotropy is maintained for films as thick as $\sim$ 25-30 Å. In order to check the layer structure of our sample we performed X-Ray Diffraction (XRD) measurements that are reported on the left part of Fig. 2.14 with the same sample composition but with an higher number of repeats. We clearly observe the superlattice peaks that confirm that the interdiffusion between the layer is small and that we are not anymore measuring a simple alloy. On the righthand side of Fig. 2.14 we also colored the hysteresis depending on the results of our Faraday measurements with a green color for AO-HDS cases and a red one for pure thermal demagnetization (this results will be detailed in section 3.1).

In the Fig. 2.13 we summarize the value of the coercive field for most of the CoTb multilayers

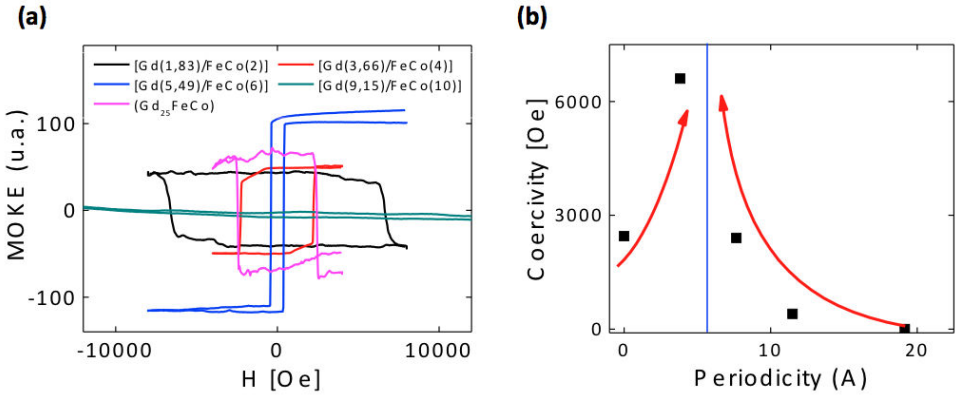

Figure 2.12: (a) Hysteresis observed for the GdFeCo multilayers deposited during this thesis and (b) their associated coercive field at room temperature. All thickness are expressed in Å. The periodicity represents the thickness of the unitary [Gd/FeCo] bilayer.

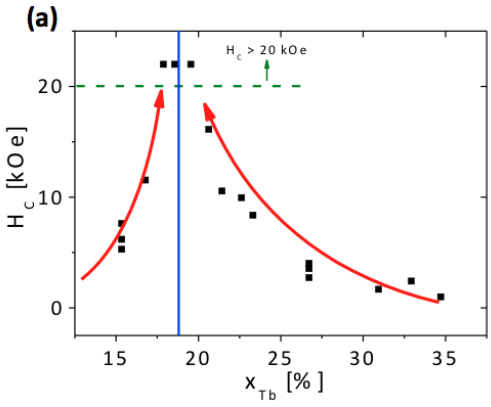

Figure 2.13: Coercive field of TbCo multilayers for compositions around the compensation.

deposited with the same convention as for Fig. **??**. In particular there is a slight shift between the divergence of the coercive fields and the division between AO-HDS and TD normally expected on each side of the curve, but this can be explained considering that out of the net magnetization compensation it exists an angular momentum compensation of the two sublattices.

On the Fig. 2.15 a detailed plot of the different hysteresis curves for each series of thickness is presented. In each of them we can highlight the inversion of the hysteresis due to the compensation. If we compare the ratio of atoms of each composition compensation with the series of CoTb alloys presented above, there is a small shift (from 18 % to 19 % between multilayers and alloys) but the trend is similar.

Finally looking at multilayers gives us access to a new degree of freedom by probing the structural dependence of the AO-HDS phenomenon.

2.2.2 Synthetic Ferrimagnets

The RE-TM systems offer a wide tunability in the magnetic parameters and perfectly suit to the need of our Faraday microscope measurements that will be described later on. However in the many samples studied the magnetic characteristics always come for interaction of the RE and TM atoms. A RE and TM sublattices as well as a antiferromagnetic coupling between them are always present. In order to probe the influence of the individual sublattices and determine more precisely the origin of the all-optical phenomena it seemed necessary to develop rare-earth free materials. The material

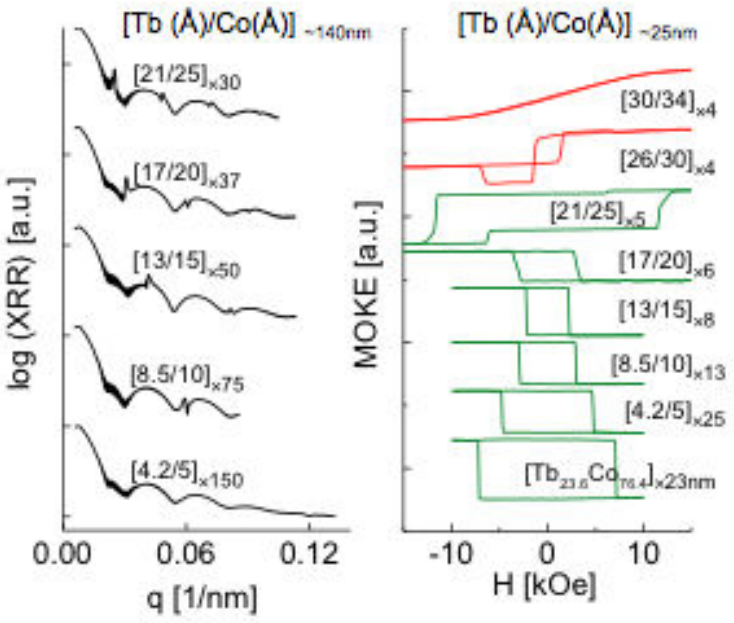

Figure 2.14: (a) X-ray reflectivity (small angle diffraction) curves for Tb/Co multilayers showing clear super-structure peaks that confirm the distinct layers and periodic nature of the multilayer samples, (b) their associated MOKE hysteresis showing the inversion of the hysteresis cycle.

would then be mimicing the behavior of a ferrimagnetic material without any rare earth element. The requirements for our synthetic ferrimagnets would be the following : a perpendicular anisotropy, an antiferromagnetic coupling between two different subsystems and a different evolution of the magnetization with the temperature for those two.

RKKY coupling

Apart from the direct exchange coupling responsible for the exchange interaction in magnetic materials such as ferromagnets and ferrimagnets an additional long-range interaction can be taken into account in multilayer stacks. Indeed in the case of two ferromagnetic layers separated by a thin layer of a nonmagnetic transition metals such as Cr, Ru, Cu or Ir an oscillatory indirect magnetic exchange is created, called the Ruderman-Kittel-Kasuya-Yosida interaction[18,110] (RKKY). In RKKY models[170]

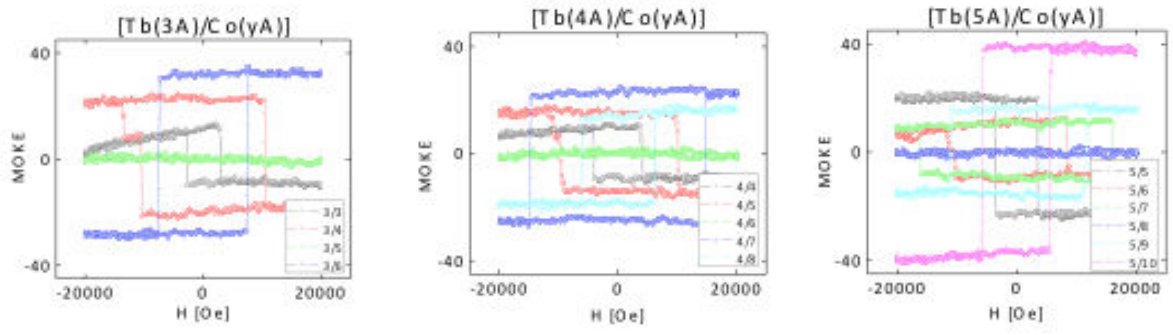

(a) (b) (c)

Figure 2.15: Hysteresis loops for 3 different series of CoTb multilayers. In each graph the thickness of Co is changed gradually.

used to account for the properties of such alloys, the conduction electrons become spin polarized in the immediate neighborhood of a magnetic particle. The spin polarization, and consequently the coupling to nearby magnetic moments, decays with increasing distance from the first magnetic particle in an oscillatory manner.

Ruderman and Kittel[170] were the first to propose that oscillations in the spin density coupled magnetic impurities in normal metals. This theory was expanded to explain magnetic coupling between ferromagnetic layers separated by normal metal layers[22,191,83]. Indeed in metals the Fermi surface marks a sharp cut-off between occupied and unoccupied states at 0 K. This results in spatial oscillations of the electrons in response to a localized perturbation[22,191,83]. In the case of a magnetic perturbation in a normal metal, the oscillations will be in the electron spin density of the material[191]. the magnetic perturbation in the normal metal is the result of coupling between the ferromagnet and the normal metal at the interface through the s-d Hamiltonian[83,179]:

$$\mathcal{H}_{sd} = -J_{sd}\mathbf{m}_{FM} \cdot \mathbf{m}_{NM} \tag{2.7}$$

where J_{sd} is the effective exchange coupling, $\mathbf{m_{FM}}$ is the magnetic moment in the ferromagnetic layer, $\mathbf{m_{NM}}$ is the magnetic moment in the normal metal layer. From Equation 2.7 positive values of J_{sd} favor ferromagnetic alignment between $\mathbf{m_{FM}}$ and $\mathbf{m_{NM}}$ at the FM/NM interfaces. Away from the FM/NM interfaces, the induced moments in the NM oscillate across the spacer layer. Depending on the phase of the oscillations this will impose either ferromagnetic coupling, shown with positive values in figure 2.16, or antiferromagnetic coupling if the value is negative.

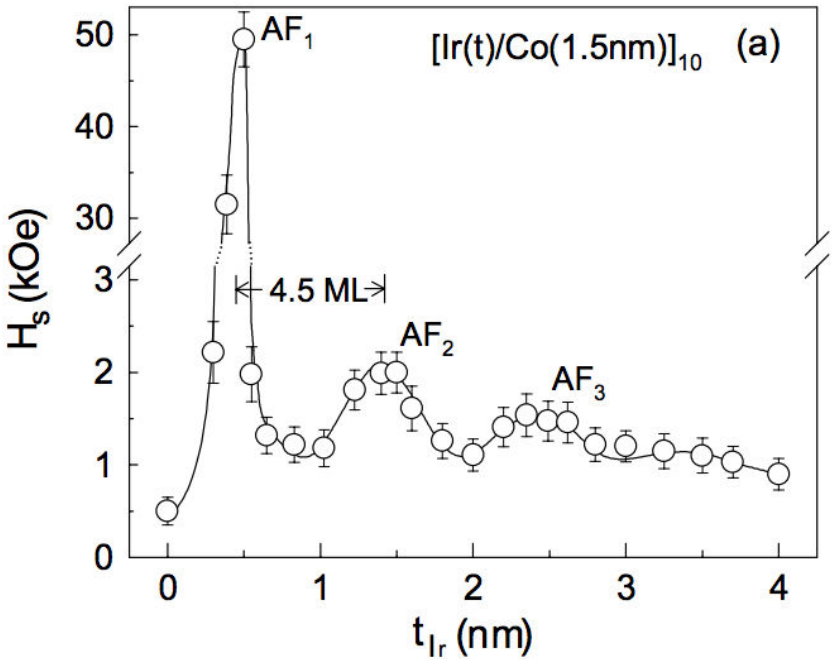

Figure 2.16: Thickness-dependent saturation field H_s, showing an oscillatory and decaying behavior. Figure extracted from *Luo et al.*[129]

Magnetic properties of Co/Ir-based ferrimagnets

Thanks to the RKKY interaction we were able to mimic the ferrimagnetic structure naturally occurring in RE-TM systems. A careful engineering of the multilayer stack gives access to a control of most

of the magnetic parameters. In our structures, FM/NM interfaces are between the Co magnetic layers and the Ir spacer layer. As we are interested in large antiferromagnetic coupling between RE and TM we explored only a very narrow range of Ir thicknesses around 4.5 monolayers Å where the antiferromagnetic coupling is the largest.

Perpendicular anisotropy

Ir is known to promote perpendicular magnetic anisotropy[155] and simultaneously is responsible for a RKKY coupling when inserted between ferromagnetic layers, so it seems to be the perfect candidate for our needs. Our imaging setup is limited to transmission images on perpendicular samples, so the first parameter that needs to be tuned is the anisotropy induced by the Ir depending on the Co thickness used.

In Fig. 2.17 is shown half the hysteresis curves used to characterize the coercive field of the film depending on the Co thickness using VSM measurement. For that we chose an Ir thickness responsible for a ferromagnetic coupling (typically 1 nm) in order to directly add up the contribution of all the Co layers. Than we vary the Co thickness to see what is the optimal thickness. We even use 5 repeats of this combination in order to increase the magnetic signal for the measurement.

As we can see that the anisotropy is directly perpendicular but for thick layers of Co a deformation of the reversal slope is appearing. This limitations is intrinsic to the nature of RKKY coupling that depends on the conduction electrons at the interface between the magnetic and non-magnetic materials. In order to increase the distance of the coupling it could be possible to change the spacer layer but the perpendicular anisotropy might vanish so Ir is the best compromise for our needs. Looking at the curve it seems that the maximum of coercive field arises around $\sim$ 10 Å so we decided to stay in this range for the next step of the building up.

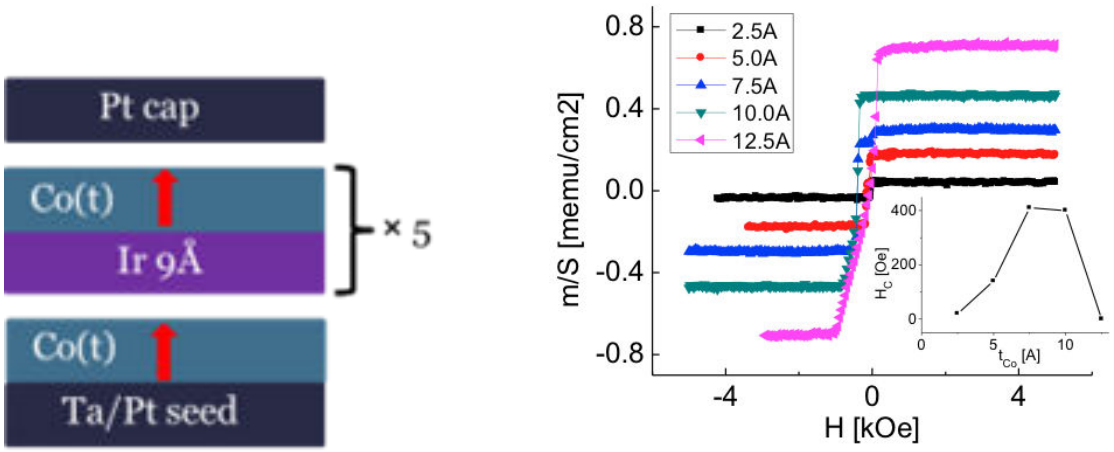

(a) (b)

Figure 2.17: (a) Schematic of the perpendicularly magnetized samples measured in (b).

Antiferromagnetic coupling

In a second time we wanted to switch to the synthetic ferrimagnetic configuration so we just changed the Ir thickness to promote antiferromagnetic (AF) coupling. In our case we used 5 Å layers of Ir to

position ourselves along one of the maxima of AF-coupling for our system. In this configuration the net magnetization stands for the sum of the two opposite contribution from the two magnetic layers apart from the Ir spacer. As pointed out before we used the same mechanism to enhance the VSM signal of our sample by repeating several times the same sequence of materials (see Fig. 2.18a). We can notice that this approach is still valid in our case because the alternating AF-coupling will directly add up the thicker and thinner layer together (for the case of the two ferromagnetic materials having different thickness), as seen on Fig. 2.18.

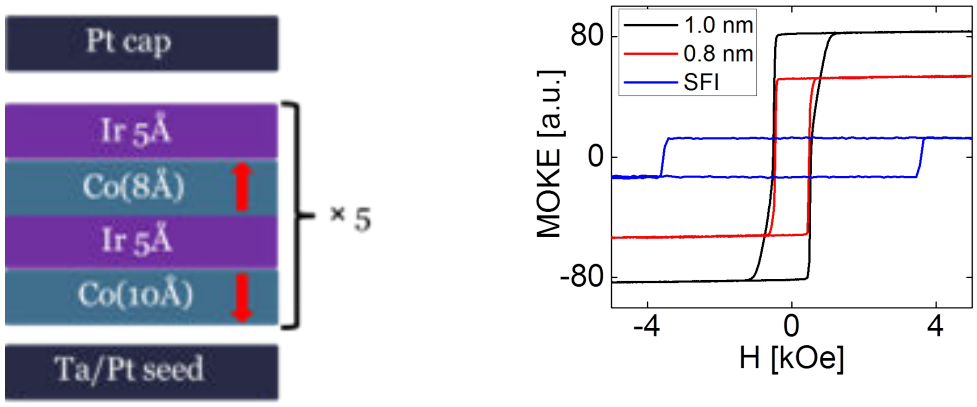

(a) (b)

Figure 2.18: (a) Schematic of the perpendicularly magnetized samples measured in (b). The red and black curves represent the individual Co layers measured separately while the blue curve corresponds to the full stack with the antiferromagnetic coupling acting.

Compensation temperature engineering

At this point we have a structure with a perpendicular anisotropy with two sublattices made of the same material (a pure Co layer) that are antiferromagnetically coupled. Depending on the relative thickness of the two magnetic layers the net magnetization will be lying in zero external field along the sublattice with the highest absolute magnetization. The last step to reproduce the magnetization of a RE-TM alloy is to build up a compensation temperature for the system. To do so we need to have a differente evolution with temperature of the two sublattices. Indeed this relative change of magnitude will create an unbalance with the temperature that can end up in a zero net magnetization of the system for one specific temperature. Because of the limitations of our VSM magnetometer it is required that the transition occurs below 400K to be measured. Furthermore our optical study of RE-TM study is focused on the modification of the excitation below and above room temperature so at least one of our system should have a compensation above 300K to fulfill our needs.

As described in the literature[77] the introduction of elements with different properties is the best way to tune the Curie temperature of a magnetic system. In our case, the idea is to split our pure Co layer into a multilayer with the proper temperature dependence (see Fig. 2.19). In addition we make sure that the Co atoms are always bonded with the Ir in order to keep a coupling constant approximately. Thanks to this stacking the global structure and the associated perpendicular anisotropy are not strongly modified while we still have a control of the Curie temperature.

In our case, this modification is achieved using Ni and Pt layers that were selected for their lower

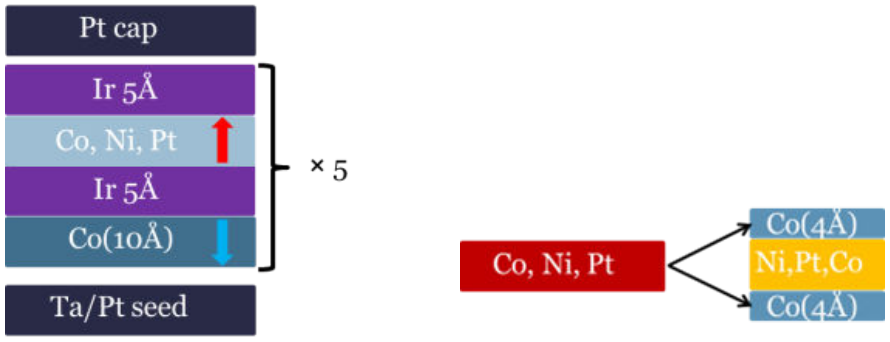

(a) (b)

Figure 2.19: Schematic representation of the synthetic ferrimagnets with a defined compensation temperature.

Curie temperature for Ni and for its ability to induce some PMA in the Co for the Pt. As you can see on Fig. 2.20 a mere modulation of the Pt thickness is shifting the compensation temperature of the sublattice that directly echoes on the divergence of coercive field as in RE-TM systems.

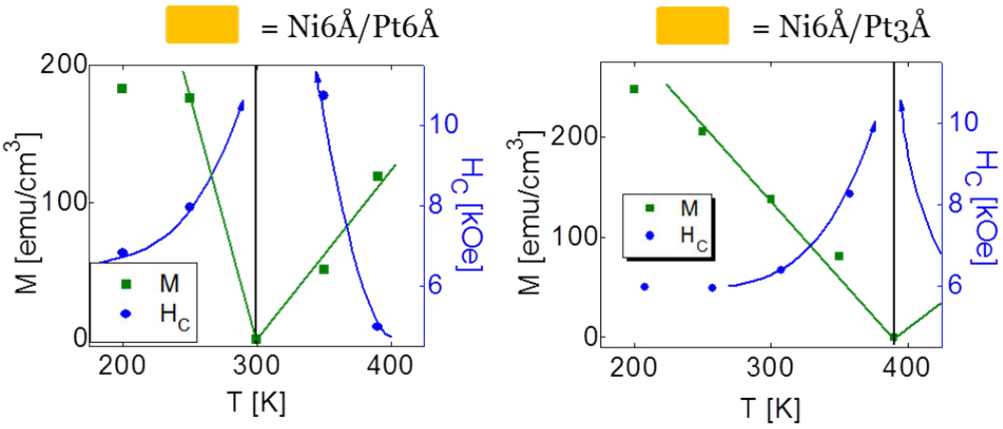

Figure 2.20: Compensation temperature measurements of two different samples where the Pt thickness is varied to modify the Curie temperature of one of the two sublattices.

Thanks to the careful layer engineering it is possible to mimic the magnetic properties of a typical RE-TM system.

2.2.3 Ferromagnetic Multilayers

Ferromagnetic materials form the basis of magnetic materials due to there early use and their infinite extend in terms of properties and applications. With the increasing need for higher density media the perpendicularly magnetized media have become the spearhead of current materials research. Many possibilities exist to favor perpendicular anisotropy but as shown in section 1.1.3 thin films correspond to the best opportunity for large effects. Among the different solutions the [Co/Pt]- and [Co/Pd]-based multilayers are known for their tunable parameters. As these systems have been extensively studied in the literature, we will only quickly describe the main characteristics of [Co/Pt] and [Co/Pd] films in this section to have a general overview of the systems we used for our study.

CoPt and CoPd multilayers

Originally CoPt alloys were known for permanent magnets and for their high figures of merits such as the one reported[95] for 50 at% Co-Pt alloy. But this type of alloys quickly suffered from the discovery of GdCo properties[31] that were much more attractive for magneto-optical applications. However in 1983 Bushow et al.[23] found out that certain alloys containing 3d transition metal atoms are expected to demonstrate good magneto-optical effects especially at shorter wavelength too. So combined with the better corrosion resistance they offer compared to rare earth compounds new perspectives were possible. In 1985 Garcia et al.[64] reported for the first time that sputtered Co/Pd multilayers with thin Co layers layers exhibited perpendicular magnetic anisotropy due to interfacial anisotropy, and in 1987 they discussed[28] perpendicular magnetic anisotropy in Co/Pt multilayers. Since then both systems are used in a variety of experiments and structures.

Co/Pd[64,46,40] and Co/Pt[63] multilayers have very similar magnetic properties: They both show perpendicular magnetic anisotropy and both Pd[46] and Pt[177] are magnetically polarized by Co. However the enhancement in Kerr rotation due to this polarization is larger for [Co/Pt], and therefore historically they have attracted more research attention than Co/Pd. In our case we mostly concentrated on [Co/Pt] systems but [Co/Pd] were responding very similarly to all the experiments performed on both combinations. However when necessary we will separate the two systems in order to correspond as much as possible.

Magnetic Properties

In multilayers a strong perpendicular magnetic anisotropy (PMA) in thin films appears for only a limited number of combinations of magnetic and nonmagnetic metals and for a particular crystal orientation, such as [Co/Pd](111) and [Co/Pt](111)[26,73,27,51,20]. Different studies[65,216] indicate the important role of nonmagnetic metals as well as the band structure in producing PMA. Experimental[52,13] and theoretical[203,223] studies have been reported that highlight the interfacial hybridization between magnetic and nonmagnetic metals concerning overlayer-induced anomalous PMA in ultrathin Co films. However since magnetic anisotropy is thought to originate mainly from the spin-orbit interaction, the orbital magnetic moment which usually makes a small contribution to magnetism in 3d transition metals, is also suspected to play an important role in PMA[146,217].

Fig. 2.21 shows the hysteresis loops of sputtered [Co/Pt] films as a function of the number of repeats for a $[\text{Co}(0.4\text{ nm})/\text{Pt}(0.7\text{ nm})]_{\text{N}}$ system where N is varied from 3 to 20. We can see that these multilayers exhibit large PMA and a low deformation at higher repeats number for the range of thickness explored.

In comparison it was found that the magnetic hysteresis of these multilayers can be strongly affected by the total film thickness. A perfect squareness of the loop, namely a single domain structure even in the remanent magnetization state, is achieved below a certain film thickness, which depends upon the modulation periodicity of the films and decreases roughly with increasing Co content. Fig. 2.22 shows the variation of the perpendicular magnetic anisotropy energy K_u, with the film thickness for thicker but similar [Co/Pt] composition systems.

However it is to mention that the thickness dependence of K_u also changes due to the existence of a buffer layer. The effects of buffer layers are often attributed to an increase in K_u, originating from an improvement in the crystalline quality and crystallographic orientation of the films.

In Fig. 2.24 are shown some of the hysteresis loops obtained for different buffer layers. As a proof,

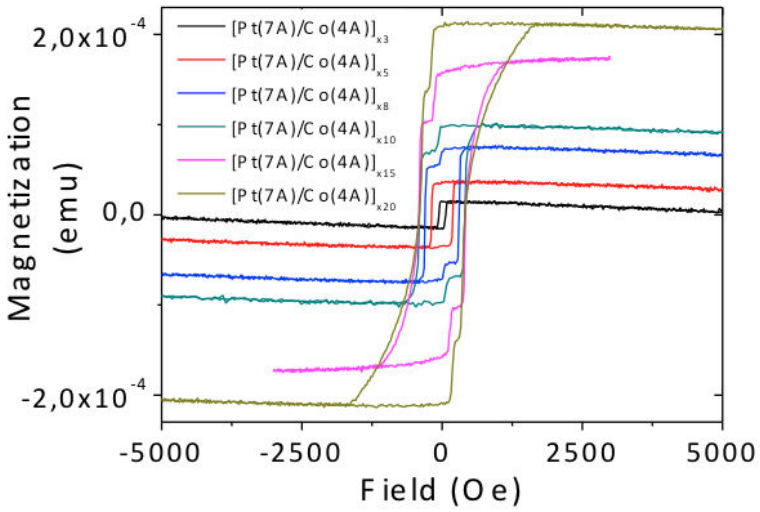

Figure 2.21: Typical magnetization versus magnetic field hysteresis loops of sputtered Co/Pt multilayers depending on the number of repeats. The kinks around zero field are just artifact of the measurement.

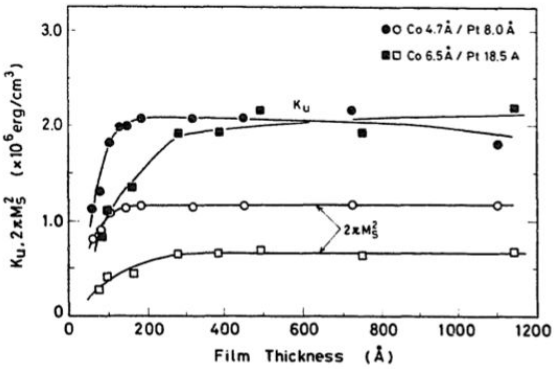

Figure 2.22: Perpendicular magnetic anisotropy energy K_u and demagnetization energy $2\pi M_S^2$ of Co/Pt films depending on the film thickness for two different [Co/Pt] systems. Figure extracted from *Hashimoto et al.*[78].

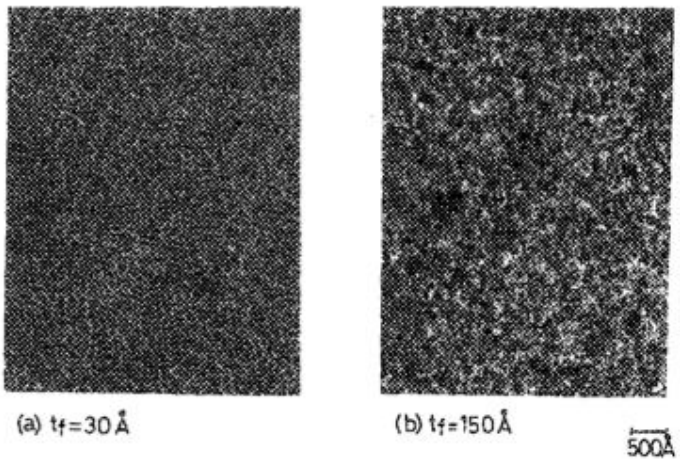

Figure 2.23: TEM photograph in Co(4.7 Å)/Pt(8.0 Å). films with (a) $t_f = 30$ Å and (b) $t_f = 150$ Å. The films were directly deposited onto Cu mesh sample holder. Figure extracted from *Hashimoto et al.*[78].

the film morphology was for example examined by TEM observation[78] as shown in Fig. 2.23. For the thinner film with a thickness (t_f = 3 nm), a distinct island structure is observed. On the contrary, a 15 nm-thick film has a continuous structure which is formed of very fine crystalline grains with a grain size below 10 nm in diameter. However the precise microstructure of continuous films does not seem to affect directly the results in our AO-HDS experiments so this particular parameter will not be discussed further here.

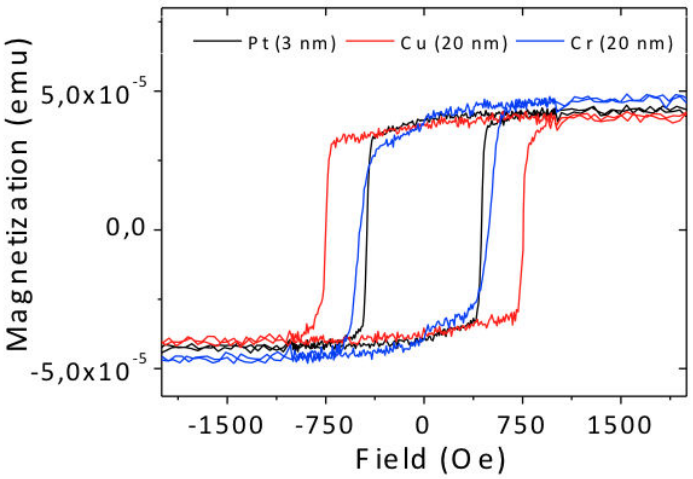

Figure 2.24: Hysteresis curves of a constant [Co(0.4 nm)/Pt(0.7 nm)]$_3$ magnetic layer deposited on three different underlayers.

Besides in the case of [Co/Pt] multilayers it has been confirmed that the mean domain size is considerably increasing for a low number of repeats equivalent to a low thickness. Figure 2.25 shows the evolution of the mean domain size d with the total film thickness t for a series of Si/SiO_2/Pt/[Co/Pt]$_n$ multilayers, with n ranging from 4 to 20.

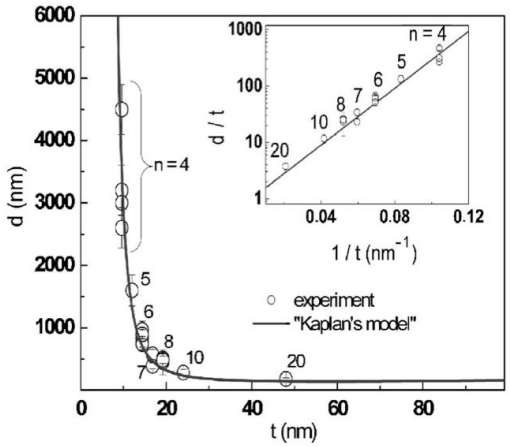

Figure 2.25: Evolution of the mean equilibrium domain size d with the film thickness t for Si/SiO_2/Pt/[Co/Pt]$_n$ multilayers in the demagnetized state. The inset shows the evolution of d/t as a function of $1/t$ in a semilogarithmic scale. Figure extracted from *Baltz et al.*[8].

Magneto-optical properties

As mentioned above [Co/Pt] and [Co/Pd] multilayers have been prospected for their magneto-optical properties in the last decades so some of the parameters of interests during light exposure

have already been studied and will be highlighted here. In particular the interaction with ultrafast laser is supposed to bring two main elements to the system : heat and angular momentum. Even if the temperature will contribute differently to the different heat reservoirs during the heating/cooling process, its final absorption by the media will certainly be dependent on the static properties of it. As a consequence the way the system absorbs the angular momentum and is modified through this interaction might be related to the value of its Curie temperature. The closer and the longer the system stays near the ordering temperature the smaller the amplitude of the effect to manipulate the magnetization is required.

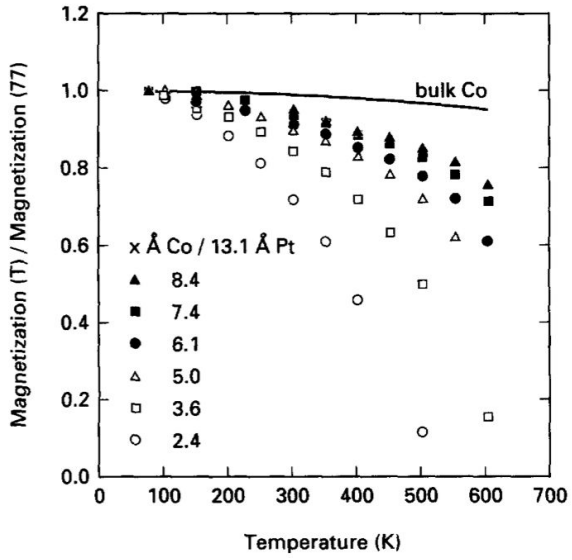

Figure 2.26: Temperature dependence of the magnetization of [Co/Pt] multilayers (60 bilayers) with varying Co thicknesses. The magnetizations are normalized to those at 77 K. Figure extracted from *van Kesteren et al.*[210].

In figure 2.26 we can see that varying the Co thickness in multilayers diminish drastically the Curie temperature. Even if the values are still quite high for this multilayers, our systems are usually much thinner (less than 20 bilayers and even thinner for AO-HDS) so we can expect a lower value in our case. This decrease of T_C is at least partly attributed to the intermixing of Co and Pt(Pd) that form a solid solution[210].

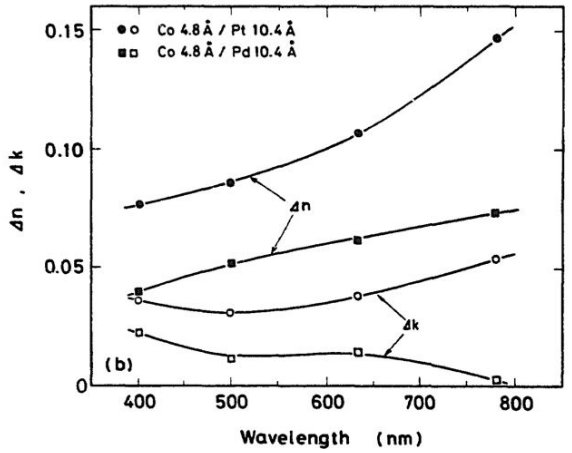

Figure 2.27: Complex refractive indices n, k and δ_n, δ_k of [Co/Pt] muitilayers at 633 nm, compared with those of the alloy films. Figure extracted from *Hashimoto et al.*[78].

Another interesting parameter regarding the current theories debated on AO-HDS is the dichroism in [Co/Pt] and [Co/Pd] multilayers. As we can see on figure 2.27 the differential refractive index between left and right circularly polarized light is plotted. As presented in the work from Khorsand et al.[175] one of the two helicity is absorbed more than the other. Considering the assumption that this criteria is a sufficient condition for AO-HDS this particular films of 2000 Å should present AO-HDS which is not the case (as presented in the last chapter). Furthermore we can see that in the case of our [Co(0.4 nm)/Pt(0.7 nm)] the dichroic effect is very small as the content of Pt is significant. This observation would tend to demonstrate than additional parameters need to be combined to complete the achieve the right effect.

Modification of CoPt properties with Ni

During this thesis one of the idea was to disentangle as much as possible the influence of the different magnetic properties on the optical properties of the materials. In the case of [Co/Pt] multilayers, one of the possibilities was to add some elements to the Co layer. As demonstrated in figure 2.29 this change permits to continuously modify properties such as the Curie temperature, the saturation magnetization or the anisotropy. One of our main concern was to maintain the perpendicular anisotropy required for the observation with our Faraday setup. In our case we were able to add as much as 60 % of Nickel content but only 20-30 % of Fe while keeping the right orientation (see Fig. 2.28). The platinum thickness is fixed at 7 Å and the number of repeats is 3.

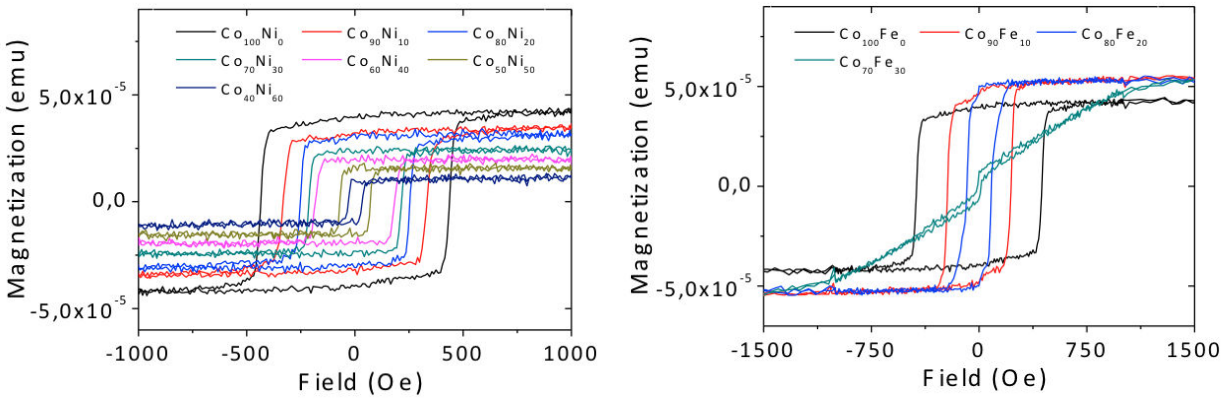

(a) (b)

Figure 2.28: Magnetization versus magnetic field for samples with an increasing content of Ni (a) and Fe (b)

As we can see on figure 2.29, Ni and Fe maintain a relatively large K_u, and a stable interfacial structure as described by X-Ray diffraction[77] even when the volume of additional elements is high. The deterioration of the Q factor (here $Q > 1$ means a perpendicular anisotropy) for (CoFe)-based multilayers is confirmed with this plot and is due to the large saturation magnetization induced in this case. Not shown here is the fact that the intensity of the (111) peak in x-ray diffraction for (Co,Ni)/Pt films is strengthened with increasing Ni content. These results indicate that the addition of Ni atoms to the Co layer scarcely changes the crystalline quality and interfacial structure, and improves the (111) orientation, possibly because Ni has a fcc crystal structure. From the above results, we can say that the Ni atom is suitable to be added to control magneto-optical properties without causing a

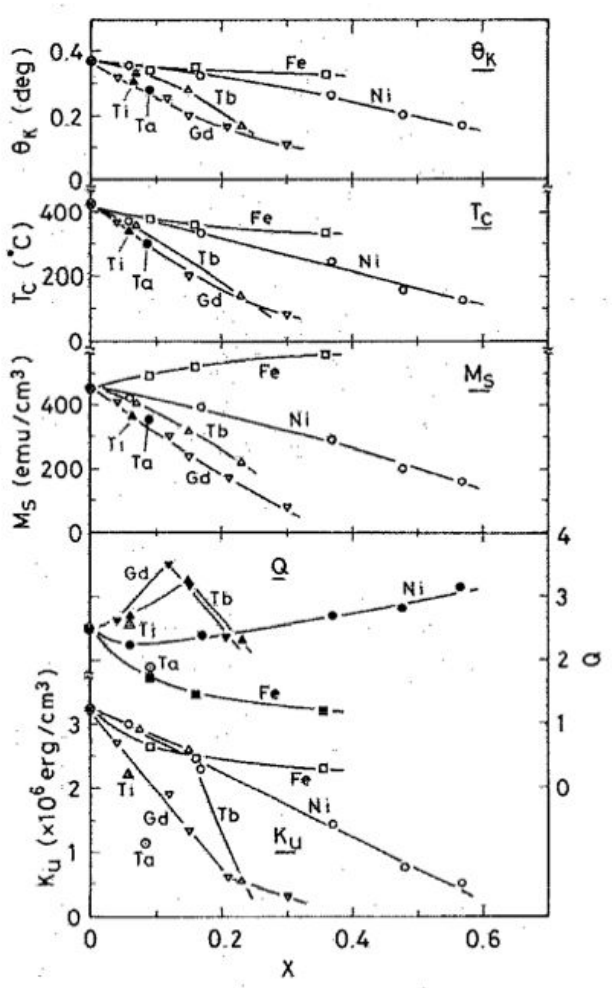

Figure 2.29: Change in magneto-optical properties of $(Co_{1-x}M_x)$(0.45 nm)/Pt(1 nm) multilayers with increase of X for M = Fe, Ni, Tb, and Cd. Figure extracted from *Hashimoto*[77].

variation in effective perpendicular magnetic anisotropy and crystallographic character.

Besides we explored the role of the Pt in the stacks to separate the influence of non-magnetic layers compared to the ones contributing directly to the magnetism. In our case we slightly increase the Pt thickness up to 15 Å in order to maintain a strong ferromagnetic coupling of the Co layers, as an anti-ferromagnetic coupling can appear for higher thicknesses[126]. This study (presented in the last chapter) can be compared with the study of Hashimoto et al.[77] highlighting the relative Curie Temperature evolution between a CoNi/Pt multilayer and a regular CoPt multilayer with an increasing Pt thickness.

Figure 2.30 shows T_C, and K_u of (Co,Ni)/Pt and Co/Pt films as a function of M_S. The Co or (Co,Ni) layer thickness was fixed at 0.45 nm, which showed the highest perpendicular magnetic anisotropy in the multilayers prepared by sputtering in this particular study. For (Co,Ni)/Pt films, the Ni content in the Co layer was varied while keeping the Pt layer thickness at 1 nm, and for Co/Pt films the Pt layer thickness was changed. As shown in the figure, the (Co,Ni)/Pt films have lower T_C, than Co/Pt films with same M_S. K_u of (Co,Ni)/Pt films is smaller than that of Co/Pt but is two to three times larger than the demagnetization energy $2\pi M_S$. In our case we can see that the small change of Pt thickness is only responsible for a minor decrease of the T_C while the large variation of Ni content is strongly decreasing this specific temperature, so we might expect a strong change in the optical behavior (impacting the power threshold in our case) with the addition of Ni in the multilayers

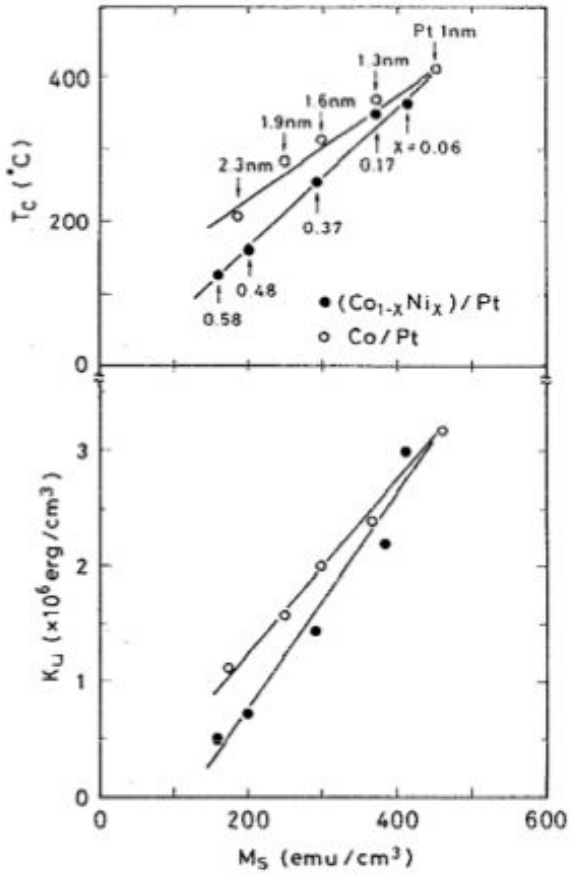

Figure 2.30: Curie temperature r, and perpendicular magnetic anisotropy energy K_u, of (Co,Ni,)(0.45 nm)/Pt(1 nm) and Co(0.45 nm)/Pt films with saturation magnetization M_S. The additional content X for (Co,Ni)/Pt and the Pt layer thickness for Co/Pt were varied. Figure extracted from *Hashimoto*[77].

compared to a mere Pt modification.

Finally it is to mentioned that most of the figures coming from the literature were measured on thick multilayers, so we might expect a variation of this value with our experiments. However it is very likely that the trends for the evolution of the parameter might remain the same. So this description can be very helpful to understand the evolution of our optical parameters that will be presented in the last chapter.

Co/Ni multilayers As mentioned in some theoretical works[139] the existence of two antiferromagnetically coupled sublattices could be the driving parameter of AO-HDS. If the study of [Co/Pt] multilayers is yet supposed to clarify the need for two different sublattices, it might be interesting to explore the case where two elements are ferromagnetically coupled in a sample. This configuration has already been considered in the same work but the conditions required for its achievement remains very similar to those of regular RE-TM compounds. In our case we studied some [Co/Ni] multilayers where the magnetization arises form the interfacial coupling of the two species. The structure seems similar to the (CoNi) alloys previously presented but the ratio of the two atoms is very different as the Ni is the major ingredient in this case.

Furthermore this compounds has the advantage to get rid of the Pt layers that is usually used to

promote the perpendicular anisotropy. Indeed the Pt is very useful for the magnetization but on the contrary it carries a very strong spin orbit coupling. In our research for the parameters required to obtain AO-HDS we decided to determine if this spin orbit coupling is necessary. As [Co/Ni] multilayers are grown and capped with Cu it offers a perfect situation for this study.

As [Co/Ni] were mostly deposited for there optical properties, we did not proceed for a full characterization of their magnetic properties so a complete description could be find in the following articles[39,10,41,145].

2.2.4 Granular media

Hard disk drive storage basics

Hard disk drive (HDD) technology is based on the long-term storage of information on tiny magnetized area on the surface of a disks. It is the orientation of the local magnetization, either positive or negative that represents a single "bit" of information. The tiny area are closely-packed onto the surface of the HDD to form circular tracks and the rotation of the disk ensure for the right addressing of the information. The needs for storage is constantly increasing so millions of bits are required and thousands of tracks covers the surface of the disks. In particular the total storage capacity of a HDD directly depends on the size of the individual bits: the smaller the bits the greater the capacity.

Magnetic recording quadrilemna

The most frequent way to monitor the improvements in the field of magnetic recording is to look at the area density growth. Basically this factor measures the rate of advance of the technology by determining how much bits can be store per unit area and thus indirectly probe the individual size of bits. The growth rate progressed with almost a constant pace since the advent of the magnetic recording however in recent years it started slowing down because of some intrinsic limits of magnetic recording. Indeed one of the consequences of the decrease in the bit size is the apparition of a spontaneous magnetization reversal due to thermal fluctuations called the superparamagnetic limit. This phenomenon exists in any magnetic material as presented in section 1.3.1 but it becomes critical as the size decreases because it relies on the height of the energy barrier between the two stable state of magnetization. In the case of a grain with a large uniaxial anisotropy constant K_u the energy barrier E_B can be expressed as follow :

$$E_B = K_u V \tag{2.8}$$

where V is the volume of the grain.

Then the grain magnetization flipping is a thermal activation process occuring at zero field governed by the Neel-Arrhenius law given by the time constant Γ. which is of the order of 10^9 to 10^{12} Hz usually.

Because of the distribution of the grain shapes and sizes, each bit written on the disk is stored on several grains to ensure that the information is reliably stored. Unfortunately the increase of the area density pushes always forward the size of the grains to store more informations but there is a lower limit. Below this limit, there is a risk that the magnetization may spontaneously reverse just due to excitation by the thermal energy that is universally present in the environment, even at room temperature.

The superparamagentic quadrilemna involves grain size, media anisotropy, the write-element magnetic field and the signal to noise (SNR) ratio required to store durably the information. In order

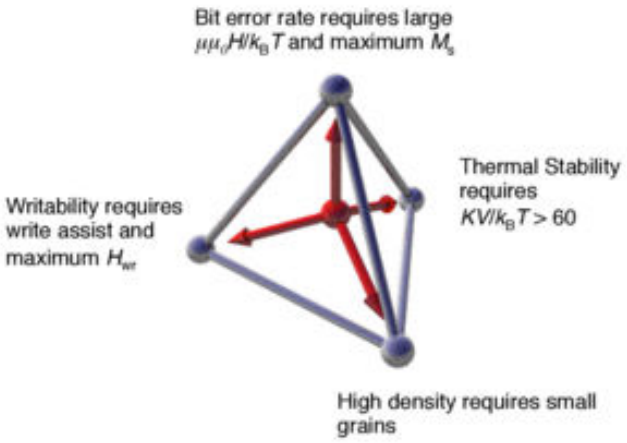

Figure 2.31: Schematic of the "quadrilemma" of magnetic recording. The decrease of grain volume requires an increase in the anisotropy constant K for thermal stability and also maximization of the saturation magnetization M_s to ensure thermal writability. Figure extracted from *Evans et al.*[54]

to assure stored information does not vanish through spontaneous magnetization reversal, magnetic media with sufficiently large E_B is required. In addition to maintain adequate media SNR with smaller bits, smaller grains are necessary. This implies that there must be a concomitant increase in media anisotropy to prevent superparamagentic data loss. Thus, in order to purposely reverse grain magnetizations during the write process, larger head fields are required, typically about the coercive field H_K. In order to ensure the stability of recorded transitions it is estimated that the parameter $K_u V/k_B T$ should be greater than about 60 to operate HDD at temperatures of about 340 K. This then defines a interlocked relationship between grain size and the media anisotropy, as illustrated in Fig. 2.31.

Granular Media characteristics

As longitudinal configuration, with out-of-plane magnetization, approaches its lower limit for thermally stable bit size, new ways are required to continue the development of the magnetic recording industry. The common approach that directly focus on the needs for high anisotropy materials has been at least partially found in the recourse to granular media. Instead of using directly full films this totally new field takes advantage of the very high magnetocrystalline anisotropy of small epitaxial grains separated by an oxide grain-boundary segregant. The current media structure then comprised magnetic alloys containing Cobalt, Chromium and Platinum (CoCrPt) that form nanosized columnar grains with a strong [0001] fiber texture. Thanks to this preferential direction the CoCrPt alloys exhibit a strong perpendicular magnetic anisotropy. In addition each grain is magnetically decoupled because of the SiO_2 grain boundary. With the current technology based on a 1 $Tbit/in^2$ area density the associated bit size is on the order of 25 nm^2, corresponding to more than 10 ferromagnetic grains for a sufficient SNR ratio (see Fig. 2.32).

In order to go beyond this density the grains must be smaller than 4 nm laterally which is currently non-compatible with the maximum uniaxial anisotropy possible for CoCrPt systems. This means that ferromagnetic materials with very high magnetocrystalline anisotropy such as $L1_0$- FePt, $L1_0$-CoPt, $Nd_2Fe_{14}B$, and $SmCo_5$ where the magnetic volume can be smaller must be used for high density recording. As the media require long-term endurance, the rare-earth compounds are unlikely to be selected as they are very susceptible to corrosion. As a result, $L1_0$-FePt phase is currently considered to be most promising material for next generation media.

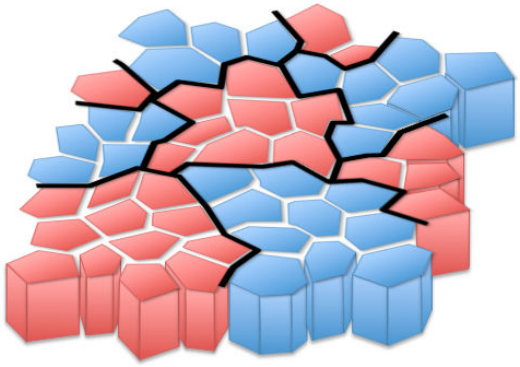

Figure 2.32: Picture of a granular recording media. Each of the bits (blue or red connected area) is formed of multiple grains to increase the SNR for read head.

Although the K_u of CoCrPt alloys is 0.3 MJ/m^3, the $L1_0$-ordered FePt has an order of magnitude larger magnetocrystalline anisotropy of 6.6 MJ/m^3, which makes the minimum size of stable ferromagnetic particles 4 nm for spheres and 2.4 nm for cylinders. A direct consequence of the quadrilemna corresponds to the fact that the associated switching field for such kind of media is higher than 3T whereas the highest magnetic field available in write head (for a $Fe_{65}Co_{35}$ soft ferromagnet) is about 1.5T. Thus the regular technology is not suitable for the needs of granular media.

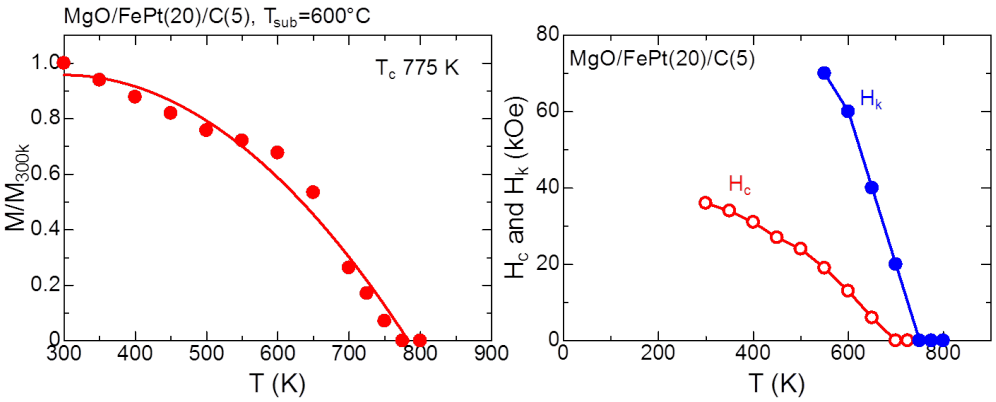

Figure 2.33: (a) Magnetization versus temperature measured for a typical granular media used in the last section. (b) Coercive and anisotropy field measured for the same sample versus temperature.

To break out the quadrilemna one of the possibilities is to assist the magnetization switching with a second element, the heat of a laser spot. Indeed the thermal evolution of granular media is responsible for a smaller coercitive field at higher temperature (see Fig. 2.34). As temperature increases the magnetocrystalline anisotropy is reduced to a point where regular write field are sufficient again. As the system cools down after writing the anisosotropy backs up and the K_u value is restored to its original value required for permanent recording. In experiments this technology is made possible using the combination of a well-focused laser beam and a regular write head (see Fig. 2.34). This new technology is called Heat-Assisted Magnetic Recording (HAMR).

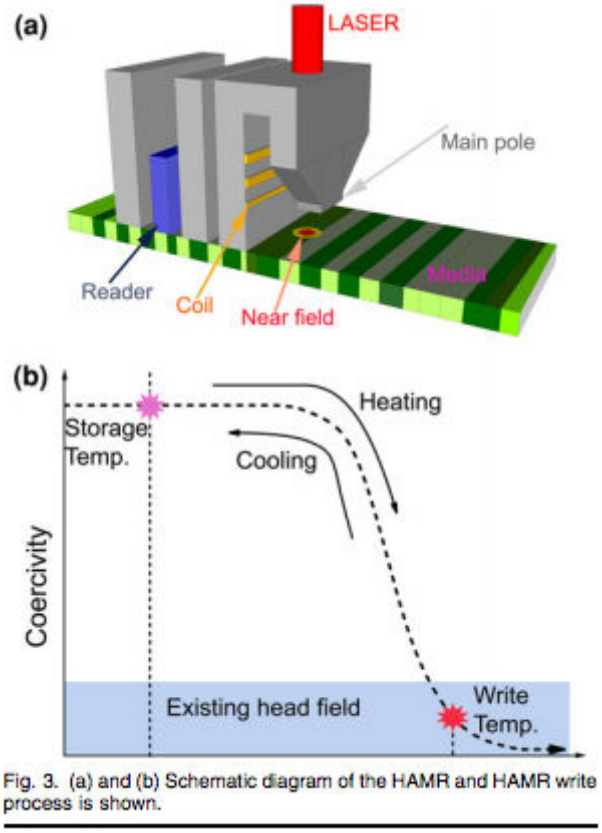

Figure 2.34: Schematic of an HAMR read/write head with a laser spot and a regular electromagnet to write the bits. Figure extracted from *Varaprasad et al.*[212]

FePt-$L1_0$ Granular media microscopic structure

The key parameters that need to be controlled to achieve the magnetic recording required are the following : A high coercivity about four times larger than that of the current recording media corresponding to 3T ; a dense columnar structure with a grain size of 4 to 6 nm ; and this need to be done on commercially viable substrate such as glass. As the magnetic characteristics can differ from grain to grain the best care as to be taken for the small size and switching field distribution of the FePt. In reality those variations are mostly induced by a mixing of the different phases of the FePt, so it is crucial to understand the steps responsible for the $L1_0$ phase.

[001] texture

As for previous recording technology HAMR requires that the magnetic easy axis of the films must be aligned normal to the film plane. However, in the case of FePt thin films deposited on amorphous substrates it is the conventional [111] that is favored due to its lower surface energy. The usual procedure is to have recourse to a seed layer that induces the transformation upon a further heating of the sample. Among various seed layers[44,224,96], MgO has a natural tendency to develop a strong [001] texture during a regular sputtering deposition and FePt possibly tend to grow epitaxially on the top of it with the following orientation crystalline relationship : (001)MgO//(001)FePt, [001]MgO//[011]FePt . Thus, strong [001] texture and its associated high magnetocrystalline anisotropy develops with FePt magnetic layers on [001] textured MgO. This technic has the advantage of being compatible with the sputtering deposition that might be the only suitable deposition technology for mass production of

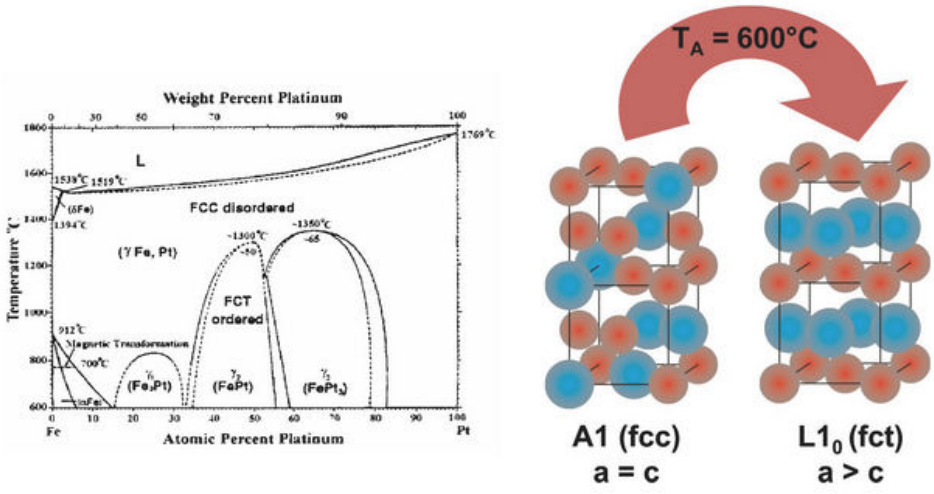

Figure 2.35: Phase diagram of Fe und Pt. Cubic FCC ordered $Fe_{50}Pt_{50}$ changes under annealing temperatures of around 600°C to the tetragonal $L1_0$ phase which is ferromagnetic[206].

HDD.

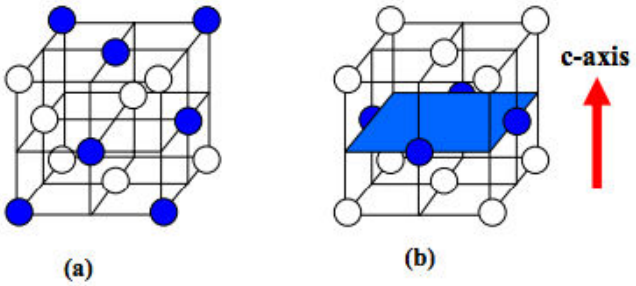

Figure 2.36: Schematic figure of the disordered (a) and ordered (b) FePt superlattices.

As mentioned above an additional temperature ingredient is necessary to strengthen the magnetic properties and narrow the distribution of shape and switching field. Indeed the choice of an MgO underlayer only allows the system to create the $L1_0$ phase but the disorder A1-phase would still represent most of the structure if the film are deposited in room temperature conditions. In fact FePt films sputter-deposited below 550°C are disordered to the A1 phase because of the kinetic constraint even if the $L1_0$ structure reaches thermally equilibrium below 1300°C. Upon static heating, the melting temperature of equiatomic FePt alloy is about 1830 K which means that any temperature below 915 K will not allow much of atomic diffusion. The best solution to overcome this issue is to add a third element in the structure that is why the Ag and C compounds where added to our samples.

(FePt)Ag-C and (FePt)C

All the FePt-$L1_0$ samples measured in this thesis were prepared in the group of Hono at NIMS in Japan. The main solution[158] developed in their lab was to co-sputter Fe, Pt, C (and Ag depending on the sample) on a heated MgO substrate. In addition the layers were deposited as slowly as possible in order to ease the atomic transport by surface diffusion at elevated temperature. In this condition the [001] texture nucleates from the underlayer. While the $L1_0$ ordering propagates during the growth the carbon is rejected from FePt and forms a thin barrier of amorphous C that will bound the final grains. This process guarantees a much lower growth temperature than that required for the post

deposition annealing presented above. The role of Ag was first described by Platt et al.[161] and Zhang et al.[222] finally demonstrated that the kinetic ordering temperature can be reduced in alloys containing Ag. The (FePt)0.9Ag0.1- 40 vol.%C film had the highest grade of particle dispersion and crystal alignment of $L1_0$-FePt particles. Figure 2.37 (a) and (b) shows the in-plane transmission electron microscope (TEM) image, and a particle size histogram.

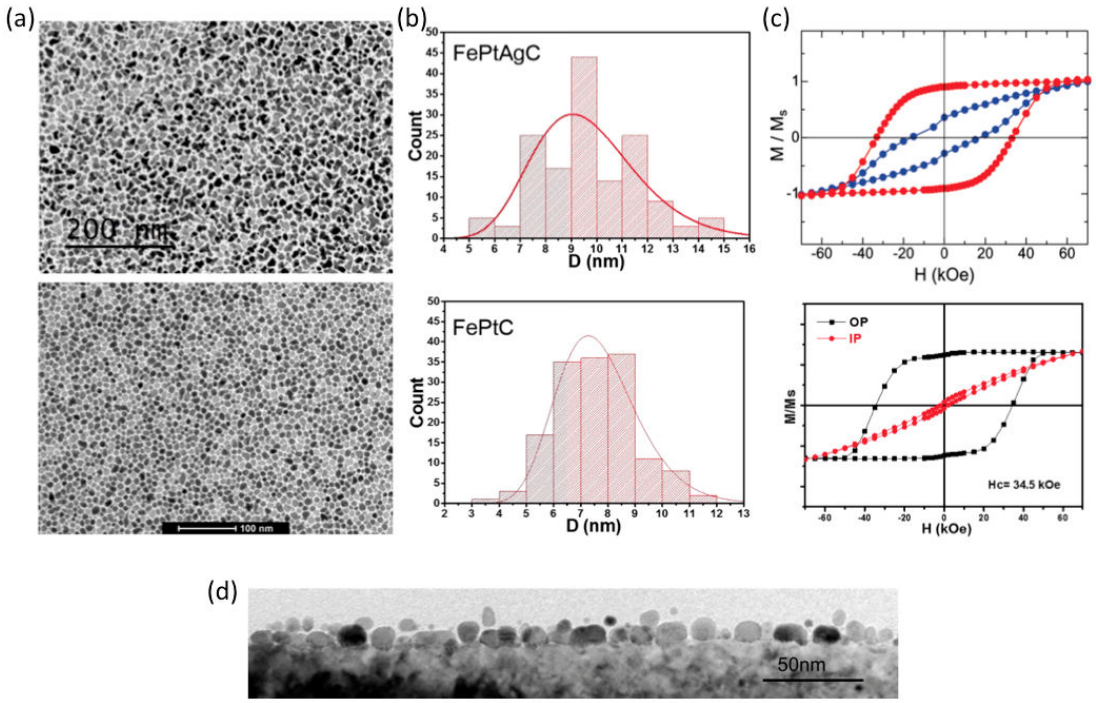

Figure 2.37: Structural and magnetic characterization of two FePt-$L1_0$ granular thin films grown on an MgO underlayer on a thermally oxidized Si substrate used during this thesis. The top row corresponds to an $(FePt)_{0.9}Ag_{0.1}$-40 vol.%C and the bottom row to a full FePt-C film. (a) Plane-view TEM image. (b) Distribution of the grains size. (c) Magnetization curves. (d) Side-view TEM image of the $(FePt)_{0.9}Ag_{0.1}$-40 vol.%C film.

The in-plane TEM image shows the uniform microstructure with an average particle size of 7.7 nm (9.7 nm) and size distribution of 2.1 nm (2.1 nm) for FePtC (FePtAgC respectively). The pitch distance (center to center) is about 10.8 nm (15.5 nm). Figure 2.37 (c) shows the magnetization curves of out-of-plane and in-plane directions. The film has strong perpendicular anisotropy. The perpendicular H_C is about 3.5 T, and an anisotropy field estimated by the cross point of the in-plane and out-of-plane curves is about 6.5 T. The estimated K_u of the FePt particles is 4.3×10^6 J/m^3 , which is half of that in the bulk. The high K_u and H_C result from the high degree of order in these films. Because the (FePt)Ag-C nanogranular films can be deposited easily by sputtering on the MgO seed layer, where crystal orientations are naturally aligned to the [001] direction during the film growth, the (FePt)Ag-C films can be fabricated various substrates such as glass or amorphous metals.

The magnetic properties and structural characterizations seems to fit perfectly to the needs of the HAMR technology, however a better look to the cross sectional TEM in Fig. 2.37 (d) highlight some of the drawbacks held by C in FePt-C films. Indeed one can see the high roughness on the surface (see Fig. 2.37 (d)) of the film induced by the too strong driving force for phase separation due to C. Although strong phase separation makes the particle isolation better in the lateral direction, this in turn interrupts the columnar growth in the growth direction and causes another grain to nucleate on an underlying grain. This evolution is prejudicial both for magnetic properties because the high

columnar aspect ratio $D/h > 1.5$ is weaken and for the HDD applications where the flatness of the disk is a key parameter.

Anyway as it is unlikely that those refinements of the parameters would affect the optical properties of the films, we will consider the columnar media in its globality to compare the results with the other kind of materials.

2.3 Magneto-Optical Measurements Technics

The evolution of magnetism through the application of ultrafast pulses can be divided in two main parts : the dynamic process and the static final state of magnetization. Even if we would expect a similar evolution of the magnetization for the two timescale the very complex physics involved in the hypothesized mechanisms could be counterintuitive. As most of the previous research were mostly focused on the very first picoseconds of the dynamic in order to understand the final state, we decided to emphasize on the understanding of this new physics through the direct observation of the final magnetic configuration for different systems. In this thesis we will try to make the link between the characteristics of the light excitation that is created thank to an amplifier system and the observation performed with a Faraday microscope. Therefore, this chapter starts with a brief general introduction on this both aspects. We will then point out the procedure and main behavior observed in our systems to have a clear nomenclature. In addition we utilized several setup extensions involving electrical measurements, which will be briefly introduced in section **??**.

2.3.1 Faraday imaging

Faraday Effect

In 1845, Michael Faraday discovered the first physical phenomenon linking light and magnetism[57]. He was able to rotate the polarization of an incident light when he induced a magnetic field in the direction of propagation of the light in a transparent dielectric medium. In this configuration a linearly polarized incident light going through the medium is subject to a circular birefringence effect. In circular birefringent materials, different indices of refraction exist for the left and right circularly polarized component. As a result, these beams propagate at different speeds through the medium. As any polarization can always be divided into its two left and right circular components, the two rays have different evolutions that end up in an offset for the final polarization compared to the incident ray. This effect is known as the Faraday Rotation or Faraday Effect. The relation between the rotation of the ray and magnetic field is given as:

$$\theta = \nu B d \tag{2.9}$$

with ν the Verdet constant of the material, B the magnetic field and d the distance traveled by the light in the medium.

Even if this phenomenon was first demonstrated using an external magnetic field it is directly existing in ferromagnetic materials due to their intrinsic magnetization. In this case the polarization rotation is the result of spin-orbit interaction that creates an asymmetry of the electronic wave-functions, leading to a rotation of the excited dipolar currents[6]. Depending on the wavelength the expression of the Faraday rotation can be different but in the case of the visible range or its vicinity

the electric dipole approximation can be used. It is then possible to express the rotation angle θ_F of the polarization plane for a linearly polarized light transmitted through a magnetized medium[108] :

$$\theta_F = \alpha_{ijk} M(0) \frac{\omega L}{nc} \tag{2.10}$$

where α_{ijk} is the magneto-optical susceptibility[160,99], $M(0)$ the first order magnetization, ω the frequency of the incident light, L the propagation distance of the light in the medium[226], c the speed of light in vacuum and n the refraction coefficient of the medium.

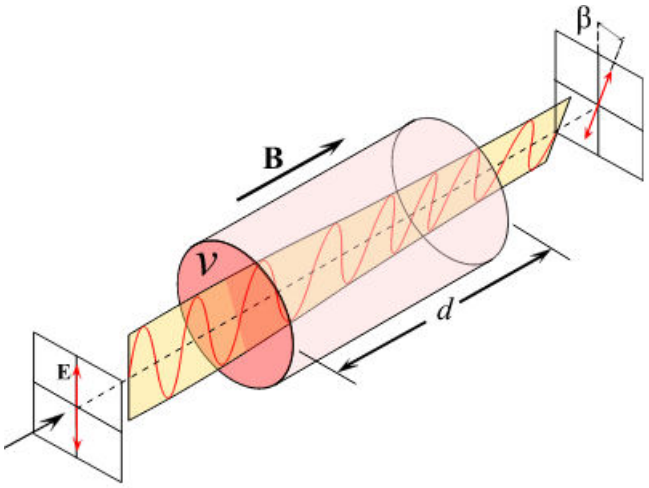

Figure 2.38: Faraday rotation through a magnetized medium. Figure extracted from *Borzsonyi et al.*[19]

Therefore, linear magneto-optical effects can be used as a probe of the magnetization of a medium and can be sensitive to very thin magnetic films[164]. However in the case of a combination of different atoms, such as alloys or multilayers, the Faraday rotation depends on each material parameters which can make the observations harder than in individual layers. Furthermore, the Faraday rotation only happens when the direction of magnetization is along the beam axis. In the case of our polar configuration this means that only samples with an out-of-plane magnetization can be imaged.

Setup for static magnetization observations

In order to detect the change in the final state of magnetization after the lighting we designed a classic Faraday microscope that allow a direct imaging of the sample while using the ultrafast laser beam. In both laboratories (IJL and CMRR) the same configuration was used (see Fig. 2.39 and only a few details where modified regarding the magnification or the power control and measurement for example.

A Faraday microscope is a combination of a source of light, a pair of polarizer-analyzer, a magnifying lens and an imaging device. If the concept of the Faraday effect will be described in the previous section, we will quickly go through the important features to take into account in a static Faraday imaging setup.

First of all the resolution of the final picture is due to the combination of the magnifying lens and the number of pixel of the camera. In our case we used a regular charge-coupled device (CCD) camera with a pixel size of approximately $\sim 3\ \mu m$ for a total surface of 2048 x 2048 pixels coupled to a 20x- or 40x-magnification microscope objective. A long working distance objective was even available in Nancy in order to ease the integration of additional optical or measurement devices close to the

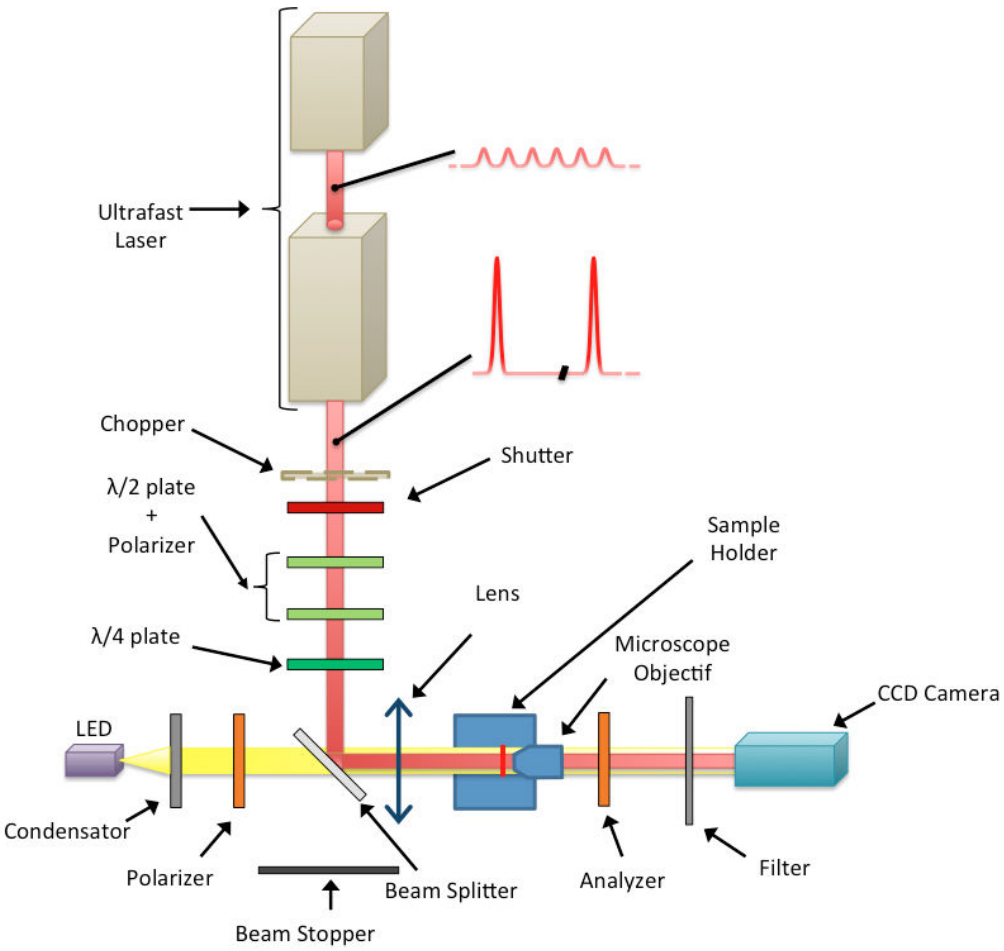

Figure 2.39: Experimental setup for femtosecond laser excitation of transparent materials and Faraday imaging.

sample. For example a reasonable working distance is necessary in order to measure the magnetic surface on both side of thick substrates too.

The Faraday effect is the consequence of the polarizer-analyzer pair that is responsible for the polarization of the incident white light and its extinction when the sample is out of setup. Indeed, the two polarizers are oriented perpendicularly to each other to give a maximum contrast when a magnetic sample is introduced along the beam axis. When no sample are inserted in the setup the projection of the incident light after the polarizer just cancel out giving a full black picture whereas the magnetization of any magnetic sample slightly modifies the incoming light and misalign the polarizer-analyzer pair. This modification depends on the orientation of the magnetization so a black and white picture will be created that reflects the domain structure on the sample. In order to obtain the highest contrast possible even for low magnetization difference we used Glan-Taylor polarizers with high extinction coefficients.

The last part of the imaging setup corresponds to the light source that gives the magnetic contrast. Basically almost any type of light is possible for the setup as long as the intensity is the highest possible to have a good definition for the image. A mere white source was used at the CMRR while a selection of monochromatic high intensity LED were available at the IJL. This latter solution offers the advantage to select the wavelength for the probe in the system and potentially modifies the selection of the atoms imaged on the CCD because of the differential absorption in an alloy for example[174]. As both the ultrafast pulses and the imaging light are going through the same focusing lens before the

sample the choice of optimum focal distance has to be consider both the spot size required for the excitation and the intensity required for a maximum imaging contrast.

Using a 50/50 beam-splitter an overlap of the imaging source and ultrafast beams is possible allowing for a direct imaging of the magnetization during the lighting. Prior to this gathering of the two beams along the same beam axis the ultrafast laser intensity and polarization are set with a combination of a half-wave plate, a Glan-Taylor polarizer and a quarter-wave plate mounted on rotating stages. Once focused on the sample with the final lens the ultrafast spot size typical range from 30 to 80 μm in diameter with an associated power depending on the laser systems described in section 2.3.2.

The magnetic preparation of the sample can be perform in situ on the sample holder with two different tools : an electromagnet for limited magnetic field up to 60 Oe, and a permanent magnet for field up to 3000 Oe for sample with high coercitive fields. All magnetic field values were measured with a Gaussmeter at the sample position to prevent drifts due to the magnets position.

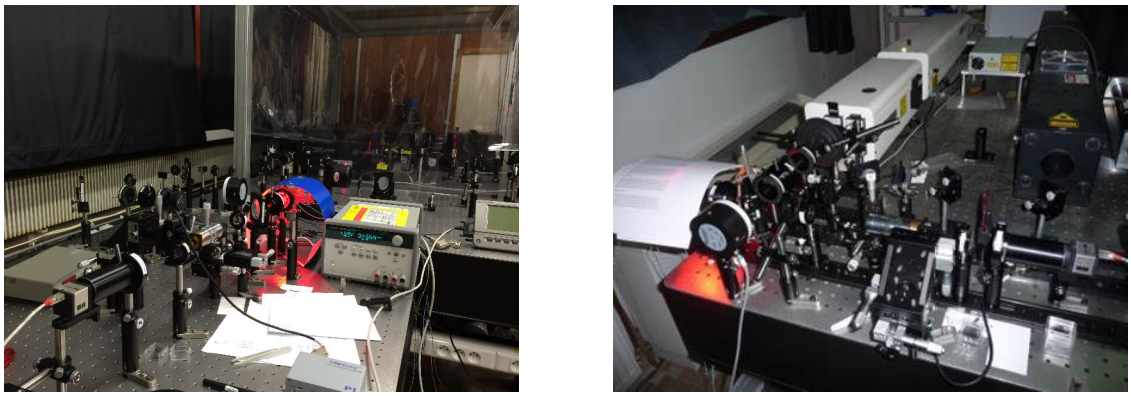

(a) (b)

Figure 2.40: Pictures of the Faraday microscopes used during this thesis.

2.3.2 Ultrafast Laser Experiments

The fastest conventional way to reverse magnetization is based on a precessional motion of the magnetization in an orthogonal external magnetic field. A realistic switching time, which can be achieved in such a process, is of the order of ∼100 ps[68,178,100], and is determined by the strength and duration of the magnetic field pulse. One of the most intriguing alternatives to such magnetic field-induced switching is making use of a subpicosecond laser pulse[109]. Already the first observation of subpicosecond demagnetization by *Beaurepaire et al.*[11] subjected to a 60 fs laser pulse suggested that such a pulse represents a powerful stimulus that is able to cause ultrafast changes in the magnetic state of matter.

Many different home-made or commercial systems give access to such type of ultrafast excitations. However among the different existing solutions, it is often the same final laser parameters that are tuned in order to probe the underlying demagnetization phenomena. In this section we will precise most of the feature permitted by the different laser used during this thesis that will give us the range of optical excitations available to study.

Femtosecond laser setup

Amplification of femtosecond laser pulses

Based on the previous work done in the field the stimulation of the magnetization seems to rely on the combination of ultrafast pulses and high energy per pulse. The usual approach that combine both requirements corresponds to the post-amplification of an ultrafast seed laser.

In particular for our dynamical experiments on the magnetization reversal we need ultrashort laser pulses (making the femtosecond timescale accessible) with a high pulse energy (allowing a strong excitation of the material).

The creation of the ultrashort seed laser pulses will not be discussed here. Information about that topic can be found in Refs.[43,172]. This section rather focuses on the amplification process and the associated pulse stretching and compression process, as this is important with respect to our pulse duration dependent measurements.

To achieve such a high peak power, a femtosecond laser adopts special amplification technique, so called the chirped pulse amplification[43,172,130] (CPA) method (see Fig. 2.41).

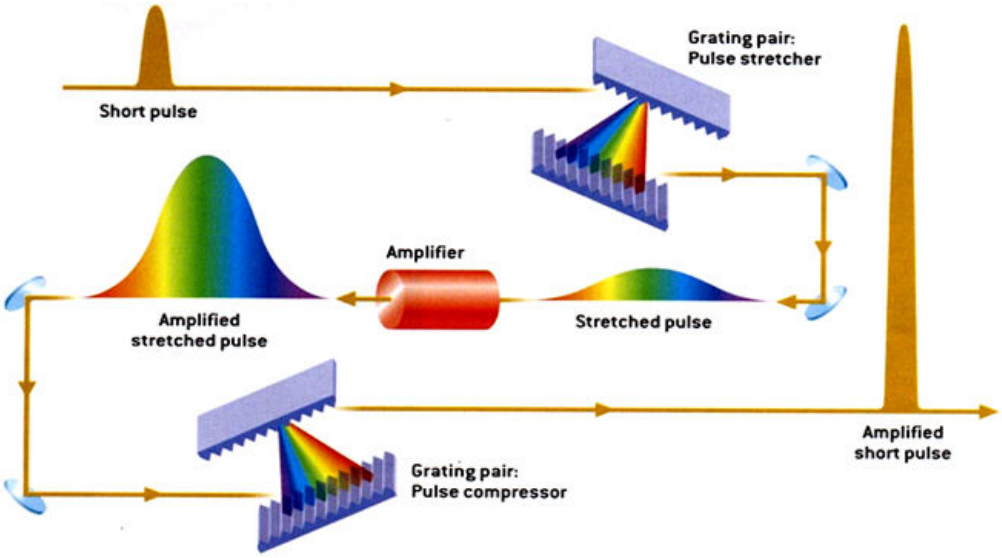

Figure 2.41: Principle of chirped pulse amplification[205].

In CPA, a femtosecond laser pulse coming from the oscillator is stretched out in time prior to introducing it to the gain medium using a pair of gratings. The gratings expand the incident laser beam spectrally so that the low-frequency component of the laser pulse travels a shorter path than the high-frequency component does as illustrated in figure 2.42. As a result, the high-frequency component lags behind the low-frequency component, and the overall pulse has longer pulse duration than the original by a factor of 10^3 to 10^5. By this pulse stretching, the laser pulse can be safely amplified by a factor 10^6 or more without causing damages on the internal optics. During this step the seed laser pulse passes several times ($\sim$ 10 times) through an optical ring resonator which includes an externally pumped laser active crystal. Accordingly, the intensity of the seed laser pulse increases each time it passes the crystal. After amplification, the stretched pulse is then recompressed back to the original pulse width through the reversal process of stretching. Therefore, the exact pulse duration depends on the distance of the compressor gratings and we can use the internal compressor of the amplifier to optimize or slightly modify the laser pulse duration.

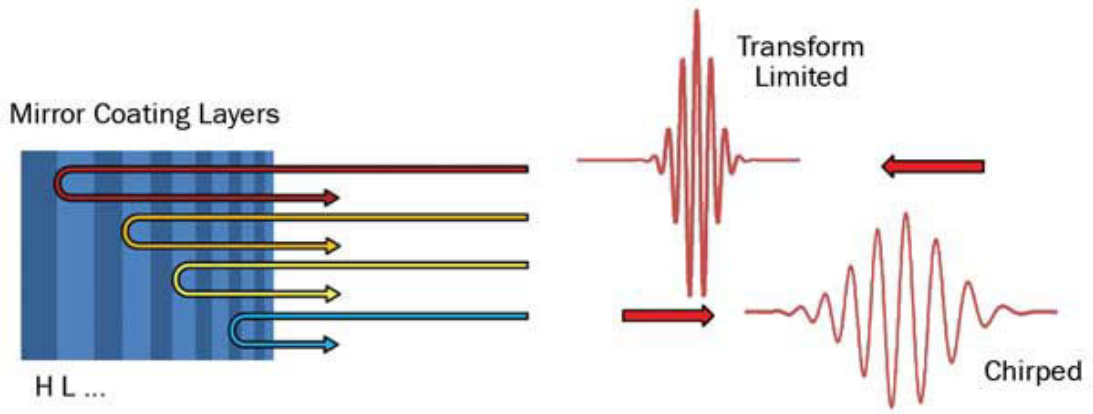

Figure 2.42: This schematic illustrates dispersion in coated optics and its effect on ultrafast pulses. H = high-index layer, L = low-index layer. Figure extracted from *Kirchner et al.*[107]

The CPA is increasing the intensity of fs-pulses by several orders of magnitude but at the cost of the repetition rate. Indeed, the typical MHz rate of the fs-oscillators is usually decreased down to kHz repetition rate for the final amplified pulse train. Even if this thesis is based on static imaging of magnetization this type of experiment is often combined with pump-probe experiment to figure out the first picoseconds dynamics. In this case the choice of amplification will be a compromise between an high repetition rate required for good statistics and a maximum pulse energy obtained for lower rates. In addition the heat accumulation during the experiment also depends on the resting time between pulses so this parameter appears to be of prime importance [ref Albrecht et autres].

Laser system used

Thanks to the collaboration between the CMRR in San Diego and the IJL in Nancy different setups have been used to perform all-optical helicity dependent switching experiments. As the experimental setups used are commercial ones this section will just provide a quick overview of the main specifications of the equipments. Especially in the third chapter if nothing is specified we will consider that its the default configuration that has been used during the measurements. In addition if a different system is not mentioned explicitly we utilized the UCSD setup to obtain the images. The two additional equipments used during this thesis and their contribution to the understanding of the phenomenon will be presented.

CMRR Setup

Using the common structure to obtain high power ultrafast pulses the CMRR setup is based on the combination of an oscillator (Tsunami) and an amplifier (Spitfire) both coming from the Spectra-Physics company. The two stages of the system use a Ti:Sapphire crystal as an active medium and deliver a central wavelength of 800 nm. The Tsunami oscillator is clocked at 80 MHz and offers a pulse duration shorter than 100 fs and a maximum output pulse energy of $\sim$ 8 nJ. This oscillator is formerly pumped with a single frequency CW laser called Millennia Edge running at 532 nm. The spectrum of the oscillator is centered at 800 nm and its bandwidth is about 60-70 nm. On the other side, the amplifier is pumped with an Empower system offering a 527 nm wavelength and a 10 mJ per pulse energy. The final output power after amplification is typically 3-4 W with a repetition rate of 1

kHz. This last parameter can be tuned using the pockel cell controller down to 250 Hz however the overall stability of the pulses can be modified using such mean.

IJL fs-setup

The ultrafast laser system operated at IJL in Nancy is based on a Vitara Ti:Sapphire ultrafast oscillator developed by Coherent Inc. using a conventional Kerr Lens Modelocking to produce pulse duration lower than 20 fs for a 80 MHz repetition rate and a bandwidth greater than 50 nm for a central wavelength of 800 nm. The maximum power output of the oscillator is ranging from 400 to 550 mW thanks to an integrated Verdi-G pump laser and an active power optimization tracking that is fully computer controlled. The oscillator is connected to an Legend Elite amplification stage that deliver up to 8 W with a 5 kHz repetition rate thanks to an additional Carrier-Envelope Phase (CEP) stabilization. Indeed this regenerative amplifier includes an active feedback control to lock the phase velocity of the oscillating light field to the group velocity of the phase envelope (see Fig. 2.43).

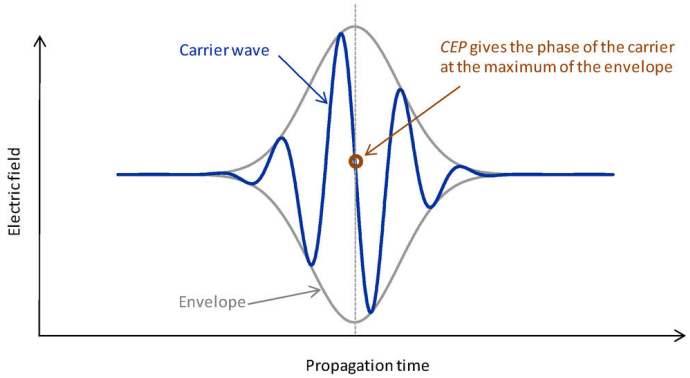

Figure 2.43: Definition of the carrier-envelope phase. Figure extracted from *Borzsonyi et al.*[19]

Thus, for ultra short pulses consisting of only a few optical cycles, the peak of the oscillating electrical field can be maximized under the phase envelope to optimize the maximum output power of the laser. The final pulse duration is approximately 30 fs but can be tuned up to 250 fs with the grating adjustments. A TOPAS-prime extension created by Coherent Inc. is available and provide the ability to extend the tuning range of the Legend Elite amplifier. The TOPAS is an optical parametric amplifier (OPA) that includes a white light seeding for an increased input noise performance. The set of modular optical extension gives access to wavelength ranging from 190 to 1200 nm. However the OPA requires a 30 fs pulse input so it is not compatible with the tuning of the pulse duration. In order to check the pulse duration a single-shot autocorrelator (SSA) is located along the beam axis and can extract pulse temporal intensity profile from 300 fs down to 20 fs in its actual configuration.

The combination of all this tools and extensions gives us the extensive possibility to study the interaction of ultrafast pulses on magnetism for different pulse durations, wavelengths and energy.

2.3.3 Main behaviors

All optical helicity dependent switching / Thermal demagnetization

In the ideal case the modification of the magnetic parameters can create two main behavior depending on the sample : the regular thermal demagnetization and the so called all-optical helicity

dependent switching. The difference between the two is defined by the shape of the track on the sample after the exposure. If the observed domain pattern shows a dependence on the laser helicity and only a uniform single domain is created along the beam path (see fig 2.44a) we consider the observation as all-optical helicity dependent switching (AO-HDS). In the contrary, if a combination of both domain orientations or a uniform grey contrast is left on the track which both correspond to a multidomain state the result is called a pure thermal demagnetization (TD) as shown in fig 2.44b.

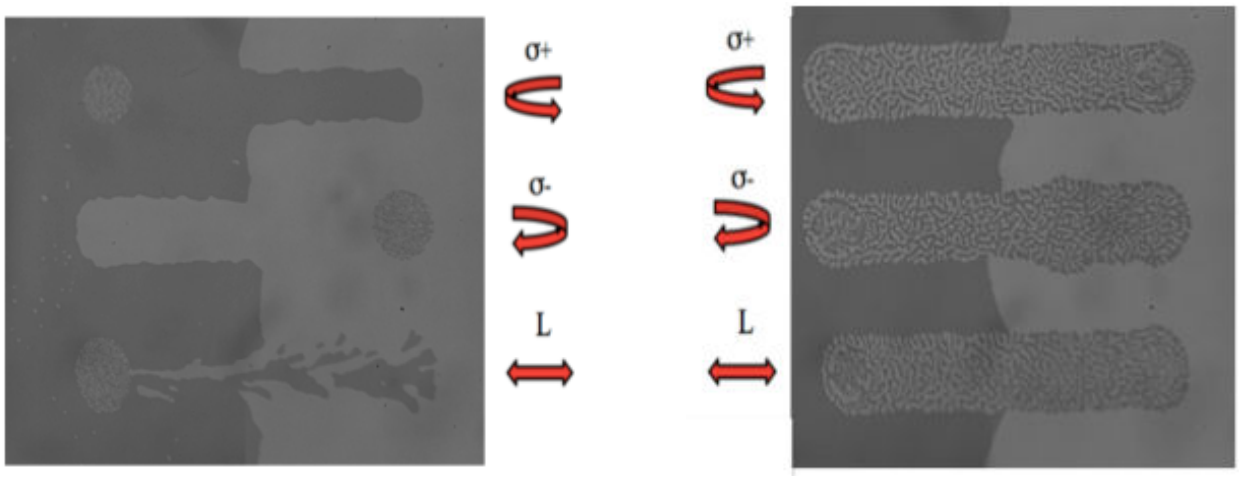

(a) (b)

Figure 2.44: Ideal cases of magneto-optical responses in the two main opposite situation : (a) AO-HDS sample with a deterministic switching for left and right helicities and a random pattern for linear polarization; (b) TD behavior with a multidomain pattern for each polarization.

Heat Assisted Magnetic Recording

Besides the two helicity dependent behaviors that characterize our study it is also possible to use a more general effect on our sample : the Heat assisted magnetic recording (HAMR). By simultaneously using our femtosecond laser and an external magnetic field it becomes possible to manipulate the magnetization of the sample locally. As presented in a previous section it is especially valuable when dealing with high anisotropy materials. Indeed the large amount of heat brought to the system by the laser is sufficient to reach a temperature close to the ordering temperature for most of the sample developed. In this situation even a small push into one of the two preferential orientation is enough for the system to stabilize in a fully saturated state once cooled. If this effect is easily observed along the track of the beam when we sweep over the sample as illustrated in figure 2.45, it can be seen in the center part of the beam too. At this position the system is in an highly unstable state very similar to a paramagnetic state. Thus the magnetic field aligns the spins along its direction for most of the time between two pulses.

This argument seems straigth-forward in the case of a regular ferromagnet, however when the system is formed by two distinct sublattices the recovery process needs to be checked to know which of the two sublattices will be dominant. In particular the existence of a ferromagnetic like state and its consecutive toggle switching could be modified with an external magnetic field. In the contrary it is usually accepted that the interaction with an external magnetic field is only growing back a few picoseconds after the excitation, so no particular change with the field should be expected. For such

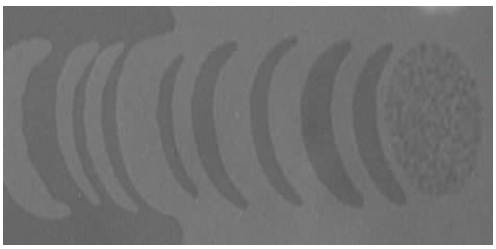

Figure 2.45: Heat Assisted magnetic writing. The black and white domain formed during the exposure of the sample with our ultrafast laser and an additional external oscillating magnetic field.

reasons we sometimes used the interaction with an external magnetic field during the exposure to probe the AO-HDS in our samples and this will be presented in the third part of this thesis.

2.3.4 Description of Magneto-Optical Measurements

The goal of this thesis is to understand the role of the magnetic materials in the all-optical helicity dependent switching phenomenon. But as we are using only a static Faraday microscopy technic to image our sample it is important to remind the origin of the contrast and the conclusions that can be done using what we observe. In this section we will focus on the link between the contrast and the magnetic structure, then we will highlight the main behavior observed for perpendicularly magnetized samples and finally we will present the method used to extract some of the optical parameters that will be presented in the last chapter.

Method for sample observations

As described above the Faraday images mostly gives relatives informations between the possible states of magnetization so a known reference is a key point of the technic. To do so we first saturate the sample with a given orientation with a permanent magnet. Using both helicities and the linear polarization we sweep the beam (actually moving the sample for a given beam position) with a regular pace and switch off the illumination using a mechanical shutter or covering up the beam path. This technic was the first one used to characterize the all-optical switching phenomenon[186] and has the advantage of smoothing the eventual magnetic parameters inhomogeneities of the sample[74] and the pulse to pulse fluctuations that could affect the conclusions. As the quarter-wave plate does not deliver a constant power for every angle we make sure between each sweeping to correct the power to be able to compare the polarizations in the same conditions. It should be noted that if the beam size and shape are supposed independent of the power we are directly modulating the fluence by this mean. We repeat the same procedure using the opposite saturation in order to test all combinations of polarizations and saturations. Then depending on the final state of magnetization left we modify the power to check for the variation of the effect with the incoming energy.

Misleading cases

Those two behaviors are the expressions of an ideal situation but in reality they correspond to the two extreme cases of a much broader zoology of observations. Indeed the Gaussian beam profile brings the sample to different temperatures on different positions of the spot. Then the center of the beam can accumulate much more heat than the parts aside. One can try to simulate the heat transfer between adjacent areas using similar equations to the one presented in section 1.3.2 but the

sweeping process adds another degree of freedom that will be discussed in section 3.6. Apart from this point the beam profile always creates the highest temperature in the middle of the track whereas the sides are kept cooler whatever the method used to study the sample (single pulses or sweeping of the beam). With such a profile different phenomena naturally take place at different location of the track. An example is illustrated in Fig. 2.46 where the center is subject to a TD process while the side is fully saturated in one of the direction which is the signature of the AO-HDS phenomenon. This demonstrates how the balance between heat and the symmetry breaking mechanism is important.

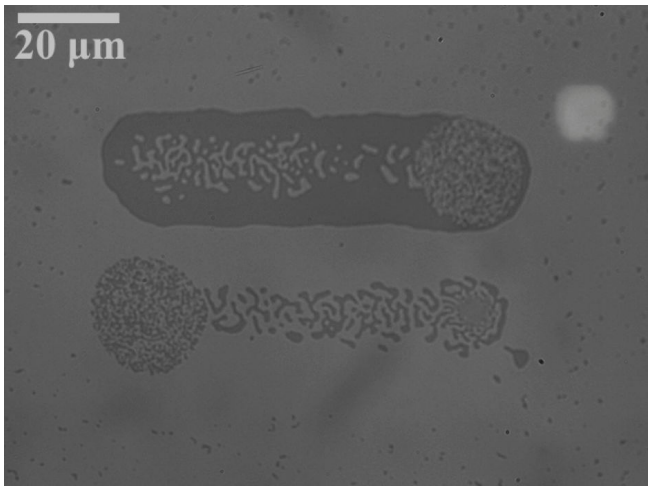

Figure 2.46: Intermediate behavior with an AO-HDS rim and a TD core.

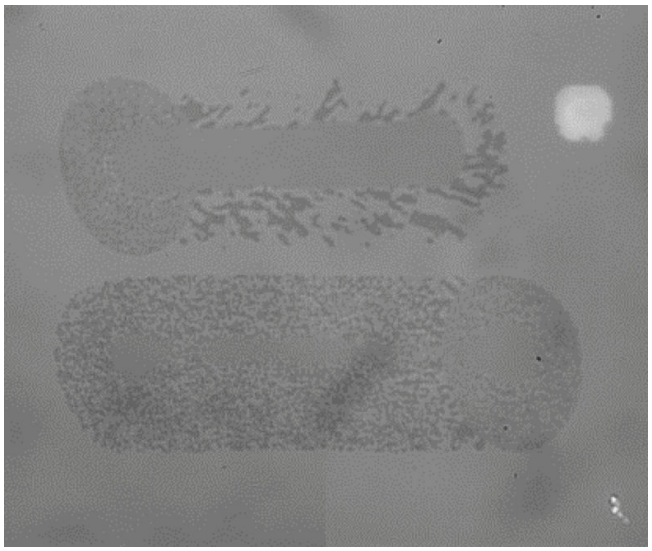

Figure 2.47: Picture of a damaged sample ([Co/Tb] multilayer) showing a grey contrast in the center probably related to an in-plane configuration.

The figure 2.47 also depicts one of the observations that can lead to incorrect conclusions. A very high power was applied on the sample which creates a damaged area in the center of the beam. This action can range from a mere modification of the magnetic properties to a complete destruction of an exposed area. In the weaker case the grey area corresponds to an area were the magnetization probably lies in the plane of the sample leading to a neutral contrast with our polar Faraday configuration. But as described above a grey continuous area can correspond to a multidomain state with submicrometric domains or even a paramagnetic part arising when the beam is on. So a special care is needed to deduce the magnetic state with the Faraday images. Hopefully this kind of phenomena can be washed

off with our method because a damaged area is not modified by applying our external magnetic field so the area will remain grey and unchanged whatever the saturation. Then an excessive power can be suspected for this effect.

Another ambiguous situation can arise when the beam is interacting with existing domains. In certain cases the laser is only responsible for the drag of the domain wall and the subsequent domain wall stretching. The reason is that the beam spot and its associated heat profile is favoring a motion of the domain wall during the sweeping. In order to check for this unwanted behavior a solution is to start with a multidomain state and to sweep the beam across the interface. If the domain wall remains mostly unchanged the conclusion stays but if a significant stretch appears the sample is designated neither as AO-HDS nor pure TD and further investigations are required.

Measure of the magnetization reversal

We presented before some of the drawbacks of the Faraday microscopy method but some improvements can easily be done on such kind of setup to compensate some of the weakness. Among the different possibilities the combination with electrical measurements during the illumination presents the best potential.

Indeed the most problematic part of Faraday setup is the lack of quantitative information about the magnetization. If the relative contrast is enough to deal with bistable systems it can get very tricky to interpret more complicated systems. On figure 2.48 we show an example were two magnetic layers are decoupled by a non-magnetic layer and subsequently exposed to our ultrafast laser setup. The background is made of two domain walls separating the three most stable state and the beam is swept over the sample. The effect on both layers is different especially depending on the first layer exposed to the laser but in every case the final state of magnetization is a multidomain state. However it is not trivial to determine if only one or both layers are affected by the laser (especially at low fluence) via domain wall vertical duplication[85] for example so additional measurements are required.

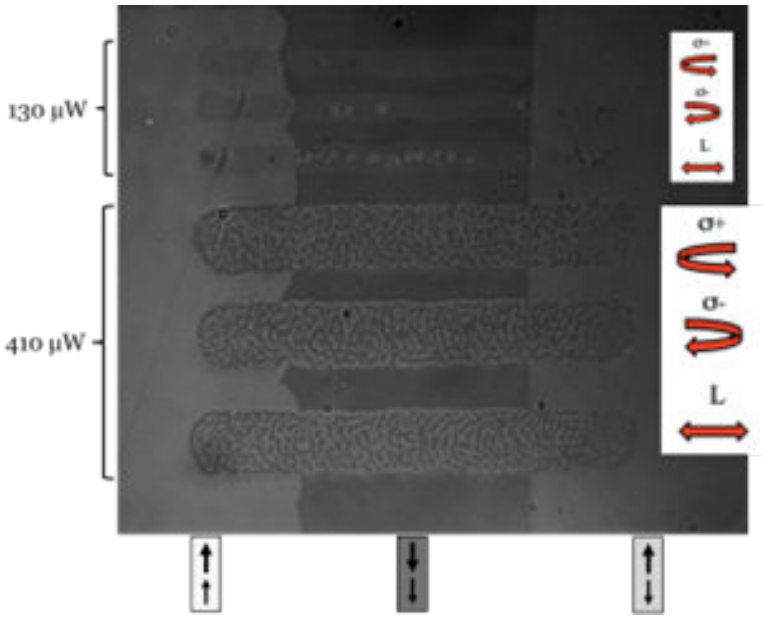

Figure 2.48: Multiple layer reversal observed with a Faraday microscope.

A chip holder has been created and can be adapted to our regular sample holder at wish. It is made of a simple breadboard mounted with regular chip pins to fit the versatile chip that are compatible

with every transport setup (including the commercial Physical Property Measurement System (PPMS from Quantum Design) in our group. 16 connections are available to offer the maximum possibilities for the system. This approach gives us the flexibility to perform any type of transport measurement on our sample or to move any existing setup on our ultrafast optics bench.

Power threshold

Once the type of effect induced by the ultrafast laser has been determined its power threshold can be extracted. To do so we perform the same methodical procedure described earlier by using a saturated sample and looking of the effect for both helicity on the magnetization. For a sample showing AO-HDS effects a pair of saturation/helicity is chosen in order to see a domain formation whereas for a pure TD effects no preferential helicity is preferred and we tend to use the same pair as the one defined for AO-HDS sample with similar compositions. In a first step we start with a power where no effect is observed and we slowly increase the power step by step sweeping the laser for each value. When the first domain appears or when the characteristic paramagnetic area in the middle of the spot shows up the power is measured. In a similar manner we start on the same sample with a power above the threshold and slowly decrease the power while sweeping the beam. When the beam is not affecting any more the magnetization the power is measured again. The final value for the power threshold then corresponds to the mean of the two values measured by the increasing and decreasing ways. From time to time the threshold for a reference sample is additionally measured in order to check if any long term bias due to the laser aging appears. For the extend of this thesis this last step did not permit to observe any significant change in the measures of the threshold power for a given spot size.

Difficulties

Role of the probing wavelength

As described earlier (see section 2.3.1) the magnetic contrast in our setups is originated from the combination of a LED source (or white light) with a polarizer/analyzer pair. The latter is mostly responsible for the intensity of the light transmitted to the CCD camera and a fine adjustment of it can ensure a high intensity ratio between up and down domains. On the other hand the light source is directly the probe of the magnetic system through its interaction with the different atoms in the material. If it is clear that the intensity of the probe is much smaller than the ultrafast excitation and therefore will not modify anything to the magnetic configuration. In contrary its wavelength comes into consideration for the understanding of the observations. In all the images that will be presented here the wavelength is defined in order to correspond to the transition metal observation. This is for example important for TbFe alloys were an inversion of the contrast is expected around 600 nm[174].

The delocalized 3d states of the transition metal are much easily probed than the localized 4f lying several eV below the Fermi level or the lower level of 5d states accessible with the visible light. Furthermore in ferromagnetic samples the final Faraday rotation is a combination of the Faraday rotation of the each individual layer. In this case a particular care has to be taken to avoid a perfect compensation of the elements with a positive and negative rotation that would greatly lower the contrast.

Averaging time

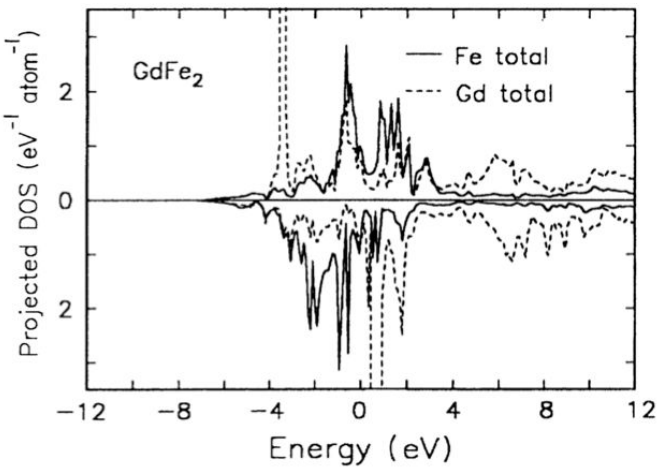

Figure 2.49: Calculated projected density of states (DOS) for a $Gd_{33}Fe_{67}$ amorphous alloy. The solid line represents the Gd 5d-electrons, the dashed line the Gd 4f-electrons and the solid line the Fe 3d-states. The energy scale is plotted relative to the Fermi energy ($E_F = 0$ eV). Figure extracted from *Tanaka et al.*[194].

The second aspect to think about when looking at the images coming from our Faraday microscope are the limitations of the CCD camera. To obtain a clear contrast of the two magnetic orientations an integration time of several hundreds of milliseconds (usually ranging from 100 to 500 ms) is required. If it does not affect the interpretation of the magnetic configuration when the laser if off several possibilities remain possible looking at areas where the dynamic is taking place. Three parameters are particularly blurring the conclusions : the repetition rate of our ultrafast laser, the maximum spatial resolution of our microscope and the metastable magnetic states induced by the pulses.

The first limitation arises from the high repetition rate of the ultrafast laser. If it is still far from the usual MHz repetition rate of common oscillators the 1 kHz and 5 kHz amplified laser used during this thesis are bursting much quicker than the imaging system. The major drawback is an averaging of the pictures over hundreds of pulses. As illustrated in fig 2.50 a single picture can have several interpretations and a special care is required to discuss the area under illumination.

Indeed the contrast recorded by the camera is only an average of hundreds of final magnetic state left after each pulse. So as long as the laser is not producing a same deterministic behavior after each pulse the interpretation can only be correlated to other experiments or measures about the sample. However even if it seems to be a major weakness of this type of measure we have to keep in mind that it is also appearing in pump-probe measurements where the result is always a statistical measurement over thousands of events. In this case it is possible to get around the problem by adding a static magnetic and to suppose that this last is not affecting the dynamics at very short time scale and that the initial state is always the same. But the statistical part of the problem remains because of the temperature accumulation due to the train of pulses. Because of that the final measure reflects the dynamic of the system in its steady state configuration and does not exactly correspond to the dynamic after one single pulse where the heating effect would be much lower. For our imaging setup some informations can be extracted from the shade of grey that is directly linked to the mean magnetic orientation. An additional contribution comes from the magnetic state left when the beam is switch off on the sample. As it is showing the configuration after the last pulse we can extrapolate that it is probably a similar behavior that happen under the beam but again the heating configuration is different.

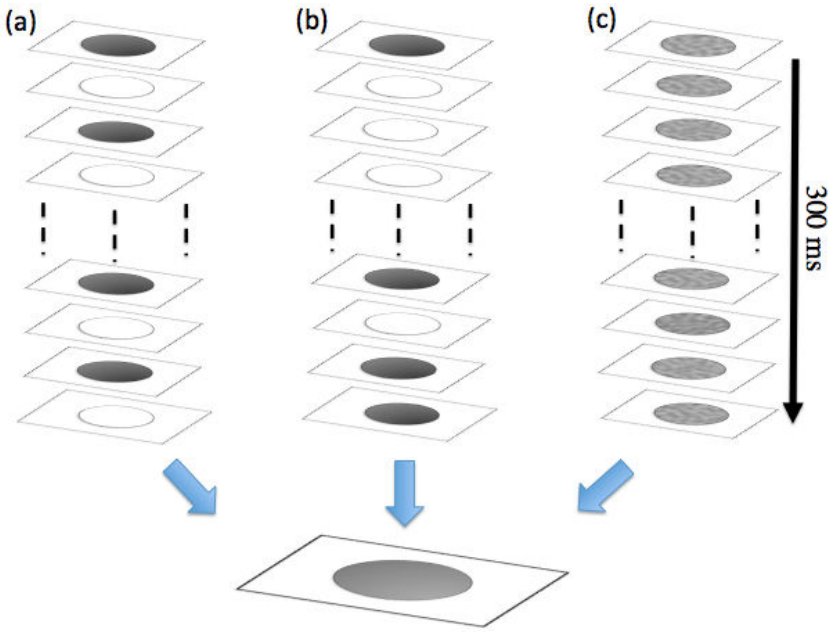

Figure 2.50: Averaging effects occurring with a quasi-static Faraday imaging. The same image can be the consequence of different domain configurations, such as (a) deterministic switching after pulse, (b) random single domain structure after each pulse, (c) random multidomain pattern after each pulse.

The second technical constraint that will limit our observations is the spatial resolution of the microscope. Using long working distance objectives and in a smaller proportion regular microscope objectives limits the maximum magnification available to image the sample. In our case 20x- and 40x-magnification objectives were used which gives us an average of 3 to 5 μm lateral resolution. For any smaller feature the separation will not be possible or at least the magnetic orientation could not be determined. Of course the obvious problem corresponds to the impossibility to image small nano- or micro-structures but as we will be mostly dealing with full films this is not a major problem. On the other hand some of the samples present a domain configuration which size depends on the magnetic parameters (as described in section 1.1.3). In particular cases the domain size can become very small and therefore our microscope is unable to differentiate individual domains (see Fig. refmutti).

An additional scan using a Magnetic Force Microscopy (MFM) can of course be performed on the uncertain area but this is really not convenient to find the area illuminated and the size of the scan is very limited in general. On the other hand an additional telescope can be added before the CCD camera to increase the precision but at some point this technic will be limited by the maximum incident intensity of the LED source. In order to obtain some informations about the magnetic state we usually modified the intensity or the polarization of the incident pulses in order to detect if there was any change in the contrast or we resort to alternative measurement technics (as presented in section refelectr) for example.

The last disadvantage of the Faraday imaging is the lack of quantitative values usually expressed for the magnetic state. Mostly based on the contrast between black and white domains it can be mislead if the several stable state of magnetization are available. During this thesis most of the system only have two possible reversed state so the upper and lower limit for the magnetization and contrast are fixed. However in the case of the the dynamic area under illumination where the state of

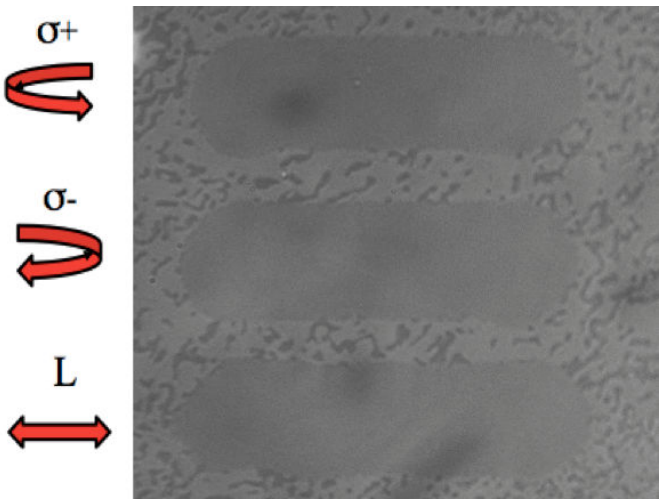

Figure 2.51: Multidomain pattern for an TD sample where the mean domain size is much smaller than the resolution of our microscope.

magnetization can be different after each pulses (see fig 2.48), it might be hard to extract the value of the magnetization. The same conclusion is particularly problematic in multilevel samples (such as spin-valves or MTJ) where the final contrast can originate from different magnetic configuration for the individual layers (see fig 2.48). In this case a first idea would ideally to have layers with very different thickness so that a clear difference should appear between the magnetic states.

An additional parameter is the range of metastable states possibly induced by an ultrafast laser. Even if two stable magnetic states are allowed in quasi-static measurements ultrafast lasers can favor intermediate states. In particular the ultrafast pulses bring so much energy into the system that some in-plane or paramagnetic configurations start to show up and do not facilitate the interpretation of contrast. A correlation between observations and magnetization versus temperature measurement already gives a good hint and the profile of the beam also helps to understand which state it can be.

According to this few drawbacks the link between static pictures and the most energetic part of the beam seems unclear. In the following we will mostly focus on the observations done among beam sweeping that gives us access to the final state of magnetization and a much easier interpretation of the measures. However whenever possible we will try to discuss the origin of the final state out of the beam with the dynamics created in the center of the beam using any additional characterization available in our labs.

Chapter 3

Material-dependence of All-Optical Switching

In chapter two we described a large variety of samples that could be grown in our sputtering deposition system. Studying different types of materials we should be able to provide new insight in the AO-HDS. Indeed not only we were able to tune the different magnetic parameters of the studied thin films but we could change the chemical and structural parameters in such a way that we can probe new aspects involved in the AO-HDS effects. We have explored the response of more than 1000 separate samples that span a range of fundamental magnetic properties such as spin-orbit coupling, exchange coupling, magnetization and magneto-crystalline anisotropy.

In this chapter we report optical responses for six classes of magnetic thin-film materials exhibiting perpendicular magnetic anisotropy (PMA) and demonstrate AO-HDS: (1) RE-TM alloys; (2) RE/TM multilayers; coupled (3) RE-TM heterostructures; (4) synthetic ferrimagnets that are made of antiferromagnetically coupled TM-based ferromagnetic layers that mimic a RE-TM ferrimagnetic material; (5) simple ferromagnetic continuous media; and (6) high anisotropy granular media expected as the next generation of magnetic recording media. In a first approach, after sweeping the laser beam over the sample the sample will fall into one of the two categories : thermal demagnetization or AO-HDS. Then we present an empirical model unifying the different observations made on different materials. The last part is devoted to the influence of field and pulse train characteristics that provide us some additional informations on the robustness and perspectives existing for the AO-HDS phenomenon.

3.1 Rare-Earth-Transition Metal Systems

Amorphous RE-TM Alloys

We have investigated a range of RE-TM alloys, RE = Gd, Tb, Dy and Ho and TM = Fe, Co or Fe-Co alloys to study the influence of the RE type and concentration on the AO-HDS. (Previous studies of Gd-TM alloys are given in refs[188,4,190,207,82] and Tb-TM alloys in refs[71,79].) These compounds all form amorphous ferrimagnetic alloys but exhibit a wide range of magnetic parameters such as the exchange coupling, spin-orbit coupling, magneto-crystalline anisotropy, magnetization and compensation temperatures[75,76]. Gd for instance has a half-filled 4f shell with a net orbital moment of zero. The spin-orbit coupling (and the coupling of the Gd moment to the lattice) is very weak in Gd-based alloys, leading to low magneto-crystalline anisotropy. However, for Tb, Dy and Ho the presence of a large orbital momentum leads to a strong spin-orbit coupling and larger magnetic anisotropy. Note

that the large difference in spin-orbit coupling in the different RE materials has been shown to have a significant influence on the demagnetization processes in response to ultrafast laser pulses[174].

Four different types of alloy have been grown: Gd_xFeCo_{1-x} , Tb_xCo_{1-x} , Dy_xCo_{1-x} and $HoxFeCo_{1-x}$. Each was deposited on a glass/Ta(4 nm) substrate and capped with a 4nm Ta layer. Most of the alloy samples show strong PMA. Only Gd_xFeCo_{1-x} alloys with $x < 22\%$ and $x > 28\%$ showed in-plane remanent magnetization due to low magneto-crystalline anisotropy and increasing magnetization as we move away from the compensation.

In Fig. 3.2 we identify as a function of average composition for which samples we observe thermal demagnetization or AO-HDS (or in-plane magnetization for Gd-based alloys). We observe AOHDS for all of the ferrimagnetic alloys studied, regardless of the specific RE element, indicating that this is a general response for this class of materials. However, we observe AO-HDS for only a narrow window of RE concentrations around 25%, in agreement with previous studies[71,79]. From the peak in the coercive field that occurs when T_{Mcomp} equals room temperature and from the symmetry of the magneto-optic Kerr effect loops allow us to determine the compensation concentration for each alloy and whether T_{Mcomp} is above or below room temperature. In previous chapter in Fig. 2.10 we show the evolution of the coercive field for each alloy composition. In Fig. 3.2 we highlight compositions where the T_{Mcomp} is below room temperature (blue region). Figure 3.2 clearly indicates that most alloys exhibiting AO-HDS behaviour show T_{Mcomp} near or above room temperature. This behavior is in agreement with recent results shown for GdFeCo alloys[137].

RE-TM Multilayers

To investigate the role of the atomic ordering and consequently the exchange coupling between the two sublattices on AO-HDS, we extended these studies to RE-TM multilayers. By evolving from an alloy to a well-defined layered structure we are tuning the heterogeneity of the system. Indeed it was recently shown that the demagnetization behavior can be quite different in alloys compared with multilayer structures, as shown by comparing FeNi alloy[136] and Fe/Ni multilayer films[171]. Moreover, there is emerging evidence that laser-induced superdiffusive spin currents can flow in heterogeneous systems (for example, see ref.[9,201]) that may play a role in the demagnetization process and AO-HDS.

The systems studied are $[RE(t_1)/TM(t_2)]_N$, where N is the number of repeats and were grown on glass/Ta(4 nm) substrate and subsequently covered with Ta(4 nm). The total multilayer thickness was kept constant at ∼25nm to be comparable to the alloy films. In these structures it is possible to tune the average composition or to keep the RE-TM ratio constant and grow different structures starting from a homogeneous isotropic amorphous alloy to well defined multilayers (Fig. 3.1). The sample heterogeneity is tuned by increasing the layer thicknesses and reducing N to keep a constant total thickness and average concentration. In all cases the magnetization of the RE layers is antiferromagnetically coupled to that of the TM layers.

For [Gd/Co] multilayers, once the Gd layer thickness exceeds 1nm the PMA becomes too weak and the magnetization lies in-plane. However, for [Tb/Co] and [Ho/CoFe] multilayers, a strong PMA and a TC larger than room temperature are measured even for a 6nm periodicity (that is 3nm layers). An example is shown in Fig. 3.1 where we compare three samples with the same average composition and total thickness: an $Tb_{26}Co_{74}$ (25 nm) alloy, $[Tb(0.3\text{ nm})/Co(0.3\text{ nm})]_{x42}$ and $[Tb(2.5\text{ nm})/Co(2.5\text{ nm})]_{x5}$ multilayers. X-ray reflectivity measurements performed on [Co/Tb] multilayers (see Fig. 2.14) show clear super-structure peaks confirming the distinct layers and periodic nature of the multilayer samples. As can be seen in Fig. 3.1, AO-HDS can be observed in all three samples and these

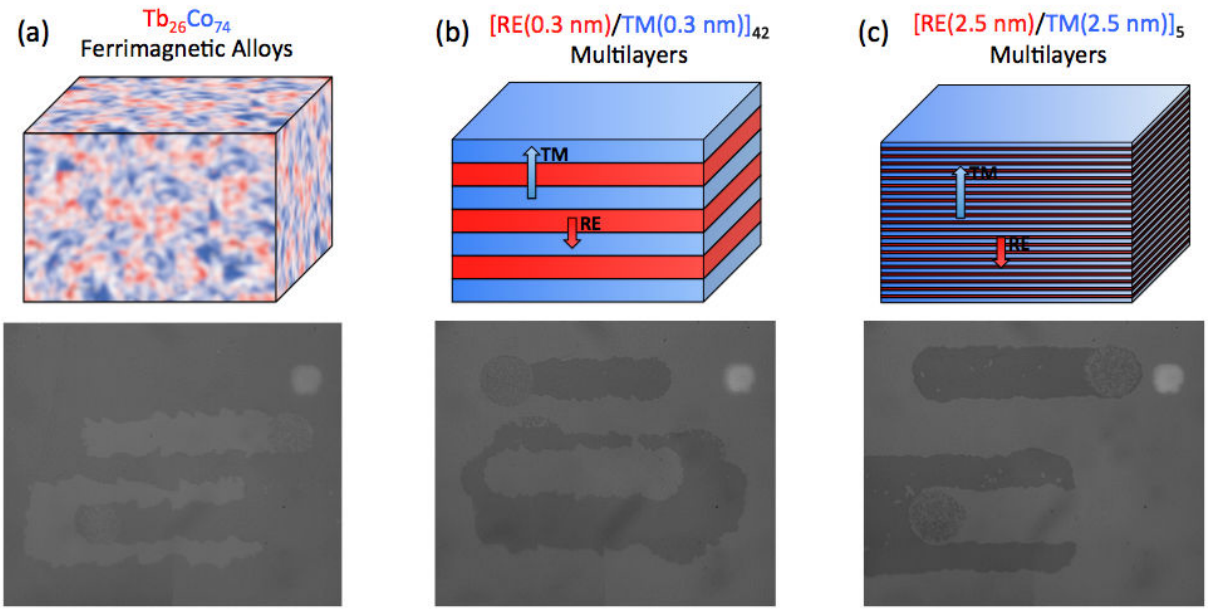

Figure 3.1: Circularly polarized beams (σ^+ or σ^-) have been swept over the samples. All-optical switching can be observed for three different samples: a $Tb_{26}Co_{74}$ alloy, a $[Tb(0.3nm)/Co(0.3nm)]_{x42}$ multilayer and a $[Tb(2.5nm)/Co(2.5nm)]_{x5}$ multilayer, which have the same average concentration of Tb and Co atoms.

measurements represent the first observation of AO-HDS in multilayer structures. From Fig. 3.1, it is clear that AO-HDS is not limited to amorphous alloys. The multilayer systems show similar compensation effects as the alloys and T_{Mcomp} can be defined from the sign change of the magneto-optic Kerr effect signal and the divergence of the coercivity (for example, Fig. 3.2 and Fig. 2.13). In Fig. 3.2 we give a synopsis of the data similar to the one shown for the alloys to summarize a set of multilayer samples where the RE thickness ranged from 0.3 to 0.5nm and the TM thickness ranged from 0.25 to 1.0 nm. For simplicity, the data are gathered as a function of the average composition (although some care is needed in making such a plot as T_{Mcomp} for a given average composition depends on the repeat period and tends to decrease with increasing layer thickness). Indeed, only a narrow set of average composition exhibit AO-HDS and most samples showing AO-HDS have compensation temperatures near or above room temperature.

These results suggest that not only does the magnetic compensation play a major role for the AO-HDS process but, crucially, that magnetic compensation does not have to be established at the atomic level but can be obtained while averaging over larger length scales of at least 6nm (see Fig. 3.1). This upper limit in the multilayers is set by the layer thicknesses that maintain PMA.

RE-TM Multilayers Heterostructures

For the multilayers described above the response to optical excitations seems to be controlled by the average magnetic properties. To further probe this averaging process we formed exchange-coupled stacks (Fig. 1c) composed of two types of multilayer such as $[Tb(0.5\ nm)/Co(0.45\ nm)]_N$ and $[Tb(0.35\ nm)/Co(0.7\ nm)]_{25\text{-}N}$. $[Tb(0.5\ nm)/Co(0.45\ nm)]_{25}$ multilayer samples have a T_{Mcomp} around 450K and the net magnetization at room temperature is aligned with the RE sublattice. These multilayers show AO-HDS. Conversely, for the $[Tb(0.35\ nm)/Co(0.7\ nm)]_{25}$ multilayers the net magnetization is parallel to the TM layers and therefore does not exhibit a magnetic compensation temperature at any

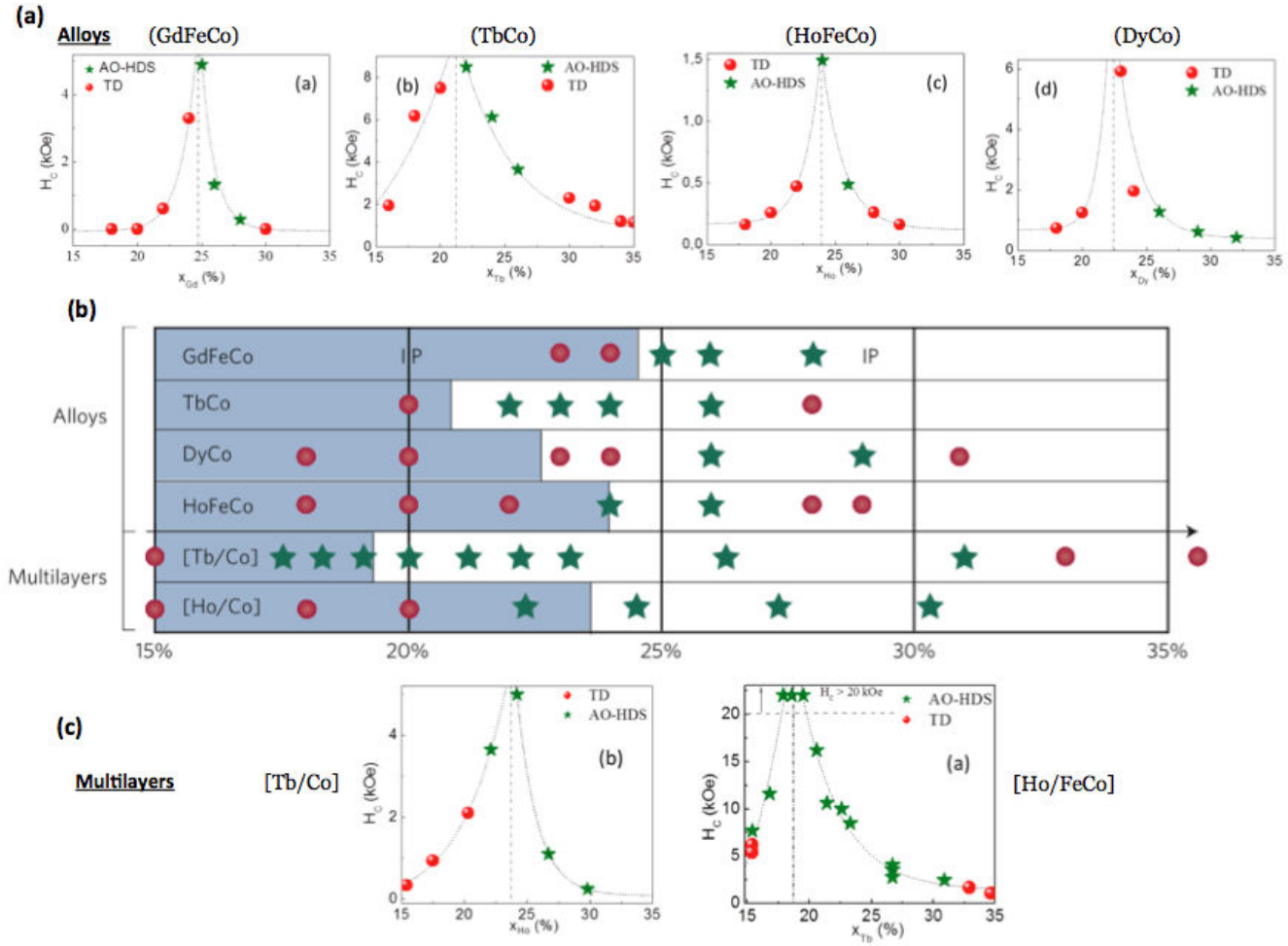

Figure 3.2: (a) Evolution of the room temperature coercive fields (H_C) for the four RE-TM alloys (Gd_xFeCo_{1-x}, Tb_xCo_{1-x}, Dy_xCo_{1-x}, Ho_xFeCo_{1-x}) and (c) for the two RE-TM multilayers [Tb/Co] and [Ho/FeCo] as a function of the RE concentration (x). (b) Summary of the response to optical excitation for RE-TM alloys and RE-TM multilayer. Red dots indicate thermal demagnetization and green stars AO-HDS in all figures. In (b), the regions shaded correspond to alloy compositions for which T_{Mcomp} is below room temperature.

temperature above room temperature. As shown schematically in Fig. 2.4 (c), the composite structure will be a mix of these two behaviours and the compensation composition will be given by the average of the total film structure. $[Tb(0.5\text{ nm})/Co(0.45\text{ nm})]_N/[Tb(0.35\text{ nm})/Co(0.7nm)]_{25-N}$ heterostructures were studied as a function of N. For N >15 AO-HDS was observed, whereas for N <15 thermal demagnetization is observed. This transition happens as the T_{Mcomp} of the average film structure is found to cross room temperature (see Fig. 3.3 (a)); that is, when T_{Mcomp} less than room temperature no AO-HDS is observed. A similar behaviour is obtained from another set of heterostructures, $[Tb(0.5\text{ nm})/Co(0.45\text{ nm})]_N/[Tb(0.35\text{ nm})/Co(0.53\text{ nm})]_{25-N}$, where again the onset of AO-HDS is linked to the position of T_{Mcomp} of the average film structure compared to room temperature (see Fig. 3.3 (b)).

3.2 Synthetic Ferrimagnets heterostructures

From the results shown above, we observe AO-HDS for a broad range of ferrimagnetic RE-TM structures and compositions with the following average magnetic properties: the samples exhibit PMA; the samples consist of two distinct magnetic sublattices (or layers) that are antiferromagnetically coupled;

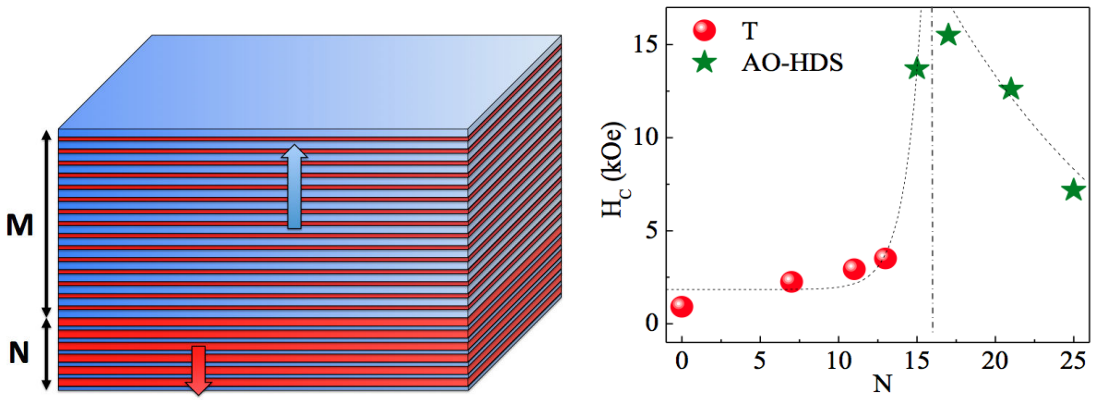

(a) (b)

Figure 3.3: (a) Schematic representation of a RE-TM multilayers heterostructure. (b) Evolution of the coercive fields (H_C) as a function of the number N for [Tb(0.5 nm)/Co(0.45 nm)]$_N$/[Tb(0.35 nm)/Co(0.53 nm)]$_{25\text{-}N}$ exchange coupled multilayers. The red dots show concentrations for which Thermal demagnetization has been observed, whereas the green stars are for AO-HDS.

and the two magnetic sublattices have different temperature dependences such that compensation of the average magnetization is present near or above room temperature. A crucial scientific and technological question is whether a RE-free heterostructure that exhibits these magnetic characteristics will also exhibit AO-HDS.

3.2.1 Synthetic Ferrimagnets Engineering

To address this question we synthesized SFI based on Co/Ir multilayers. Previous studies have shown that Co/Ir multilayers possess the combination of PMA and strong antiferromagnetic interlayer coupling to form a synthetic antiferromagnet[222,143]. In the present structure, the Ir layer thickness of 0.4nm was chosen to maximize the antiferromagnetic coupling between the ferromagnetic layers. We initially formed antiferromagnetically coupled structures [Co(1 nm)/Ir/Co(0.8 nm)]$_N$. While this structure exhibited PMA and ferrimagnetic properties we were not able to observe AO-HDS and either was able to image domains or only observe thermal demagnetization effects. However, because the 1nm Co layer has both a higher moment and higher T_C than the 0.8 nm layer this structure does not exhibit a T_{Mcomp} and thus only fulfils the first two magnetic properties listed above.

To design a SFI structure that exhibits a T_{Mcomp} we replace the 0.8nm Co layer with a [Co(0.4 nm)/Ni(0.6 nm)/Pt(t_2)/Co(0.4 nm) magnetic layer structure where the Pt layer could be adjusted to control the total moment and exchange and therefore the Curie temperature of the composite layer. This resulted in the following Co/Ir/CoNiPtCo/Ir heterostructures: Ta(4 nm)/Pd(3 nm)/[Co(t_1)/Ir/CoNiP(t_2)Co/Ir]$_N$/Pd(3 nm). This structure has PMA and at room temperature a field of 10 T is not sufficient to overcome the antiferromagnetic exchange coupling (see Fig. 3.5). At such high field, the are still not fully parallel and are just slowly tilting from their stable AF state. But as we are only interesting in the existence of the coupling compared to its real value, we just use this observation to confirm our structure. Additionnally, the thicknesses of t_1 and t_2 can be chosen such that at room temperature the CoNiPtCo composite layer total magnetization is larger than the Co layer but has a lower Curie temperature compared with the Co layer with thickness t_2. Consequently, the CoNiPtCo layer moment decreases faster than that of the Co layer with increasing temperature, resulting in

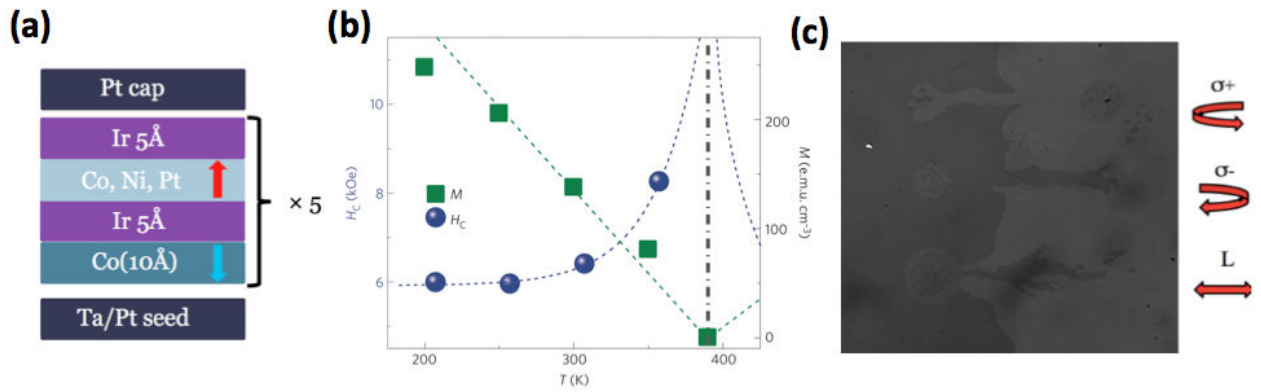

Figure 3.4: (a) Typical stack for the synthetic ferrimagnetic materials explored during this thesis. Ir is responsible for the PMA and AF-coupling, while the Ni and Pt adjunctions allow for a tuning of the magnetic properties. (b) Magnetic measurements of a Ta(4 nm)/Pd(3 nm)/[Co(1 nm)/Ir/Co(0.4 nm)/Ni(0.6 nm)/Pt(0.3 nm)/Co(0.4 nm)/Ir]$_5$/Pd(3 nm) SFI structure. Remanent magnetization M and coercive field H_C as a function of temperature allow us to define a compensation temperature at $T_{Mcomp} = 380$ K. (c) Images after scanning the laser with three types of polarized beam that were swept over the sample: from top to bottom, right circularly polarized light (σ^+), left circularly polarized light (σ^-) and linear polarized light (L).

a magnetic compensation temperature for selected structures. By tuning the layer thickness of the CoNiPtCo composite structure we were able to tune T_{Mcomp} and successfully synthesize SFI systems, showing the three properties described above.

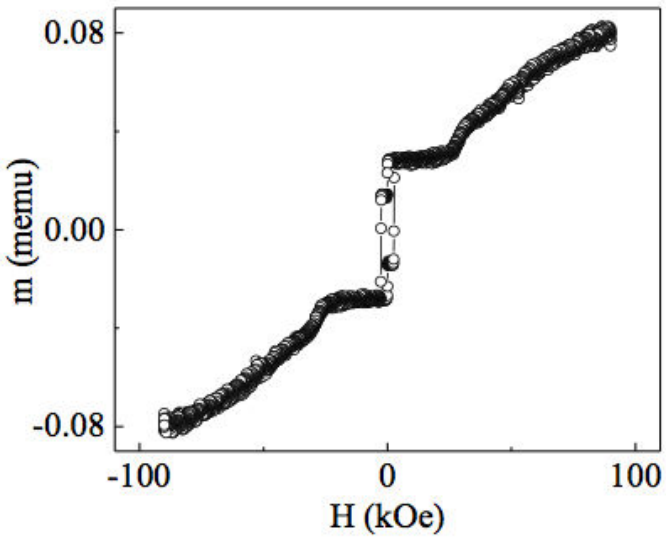

Figure 3.5: Magnetization as a function of the applied magnetic field perpendicular to the film plane for Ta(4 nm)/Pd(3 nm)/[Co(1 nm)/Ir(0.4 nm)/Co(0.4 nm)/Ni(0.6 nm)/Pt(0.3 nm)/Co(0.4 nm)/Ir(0.4 nm)]$_{x5}$/Pd(3 nm). This measurements show that an applied magnetic field of about 10 kOe is needed to overcome the antiferromagnetic exchange coupling between the Co(1 nm) and the Co(0.4 nm)/Ni(0.6 nm)/Pt(0.3 nm)/Co(0.4 nm) layers.

Figure 3.4 (a) shows the temperature dependence of the magnetization and coercive fields of a Ta(4 nm)/Pd(3 nm)/[Co(1 nm)/Ir/Co(0.4 nm)/Ni(0.6 nm)/Pt(0.3 nm)/Co(0.4 nm)/Ir]$_5$/Pd(3 nm) SFI structure. The divergence of H_C correlated to the decrease of the net magnetization to zero determines $T_{Mcomp} = 380$ K. The compensation temperature may be tuned by adjusting the layer thicknesses in the composite structure. For instance, changing the Pt layer to 0.6nm in the CoNiPtCo

layer decreases T_{Mcomp} to 300K (see Fig. 3.6). Most importantly, as shown in Fig. 3.4 (b) , the SFI structures with T_{Mcomp} greater than room temperature exhibit AO-HDS, demonstrating control of the sublattice magnetization with light.

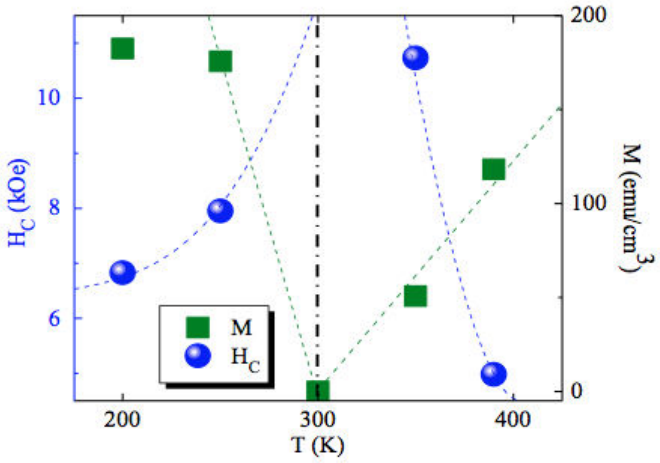

Figure 3.6: Magnetic measurements on a Ta(4nm)/Pd(3nm)/[Co(1 nm)/Ir(0.4 nm)/Co(0.4 nm)/Ni(0.6 nm)/Pt(0.6 nm)/Co(0.4 nm)/Ir(0.4 nm)]$_{x5}$/Pd(3 nm). Plotted are the remanent magnetization M and coercive field HC as a function of temperature which allows us to define a compensation temperature T_{Mcomp} = 300 K

3.3 Ferromagnetic Thin Films and Nanostructures

3.3.1 Ferromagnetic Thin Films

Evolution with the number of repeats

The optical response of ferromagnetic samples are studied by optical/heat-assisted magnetic switching experiments where the samples are excited by a $\sim$ 100-femtosecond pulsed laser source and subsequently imaged in a Faraday microscope. Figure 3.7 show images of [Co(0.4 nm)/Pt(0.7)]$_N$ multilayers (N = 8, 5 and 3) which have perpendicular magnetic anisotropy so the magnetization easy axis is normal to the film and the image contrast results from the two possible directions of the magnetization. The laser helicity is either of two circular polarizations (σ^+ or σ^-) or linear polarized (L). For Fig. 3.7, (a) to (c), the laser is scanned across a region of the films that have both magnetization directions allowing the effect of the initial state of the magnetization on the magneto-optical response to be studied.

For N = 8 (see Fig. 3.7 (a)) domain formation is observed in the region scanned by the laser, that is filled with disordered stripe subdomains that minimizes the dipole energy[86]. This process is independent of the light polarization and represents laser-induced thermal demagnetization (TD). A rim is observed at the edge of the scanned area where the magnetic orientation is opposite to the background stabilized by dipolar fields from the surrounding film. For N = 5 (see Fig. 3.7 (b)) the formation of subdomains in the scanned region is again observed. The average domain size is larger for decreasing number of layers, since in the thin-film limit the equilibrium domain size increases with decreasing film thickness[86]. More importantly the resulting domain structure depends on the light polarization. For σ^+ light white isolated bubble-like domains are observed in a dark background while for σ^- light dark domains are seen in a white background and the magnetization near the edges of

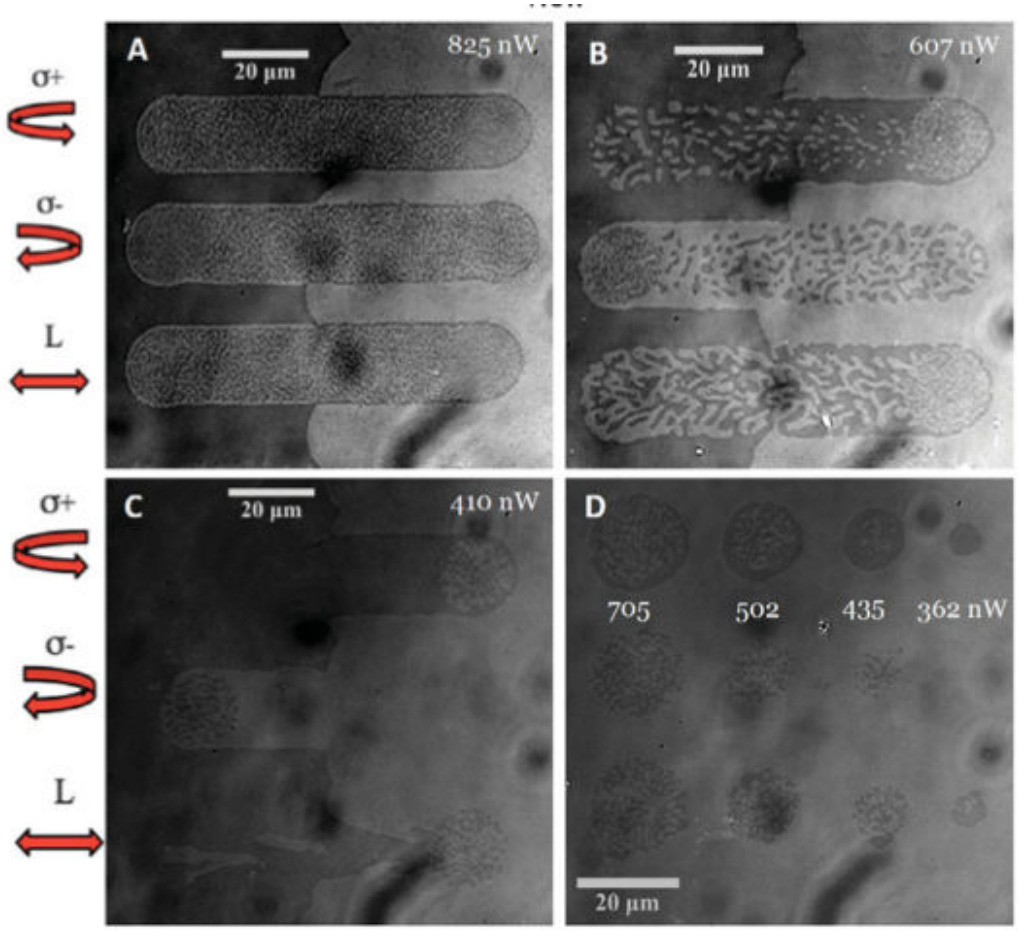

Figure 3.7: Magneto-optical response in zero applied magnetic field of $[\mathrm{Co}(0.4\ \mathrm{nm})/\mathrm{Pt}(0.7\ \mathrm{nm})]_{\mathrm{N}}$ multilayer samples to various laser polarizations. (A) N = 8 (B) N = 5 (C and D) N = 3 repeats. For each image, the laser is circularly polarized (σ^+ or σ^-) or linear polarized (L). For (a) to (c), the laser beam was swept over a region of the sample with two perpendicularly oriented magnetic domains showing black/white contrast in the images, with a domain wall that runs vertically in the middle of each image. In (d), the laser was fixed at individual spots over a region of the sample with uniform magnetization (white contrast). The average laser intensity at different spots is indicated in the image.

the line scan favors the direction opposite of the surrounding film.

In contrast for N = 3 (Fig. 3.7 (c)) fully deterministic magnetization reversal is observed for both circular polarizations that is independent of the initial magnetization direction, a clear demonstration of AO-HDS in a ferromagnetic material. The random domains created for linear polarization are much larger for N = 3 in accord with the small dipolar energy gain for ultra-thin films. Figure 3.7 (d) shows images for the N = 3 sample for various laser powers where the film is saturated in one direction and the laser spot is fixed and not scanned on the surface. For low power (362 nW) a reversed domain is written for σ^+, there is no change to the film for σ^- and a region of random domains is observed for linear polarization. With increasing laser power, regions of demagnetized random domains develop in the center of the laser spot for all three polarizations indicating that the power is such that the temperature exceeds a critical temperature for which domains are formed (e.g., the Curie temperature T_C). For σ^+ there is a rim at the edge of the demagnetized area that shows deterministic switching that is not present for σ^- or linearly polarized light.

To determine how general AO-HDS is we studied a range of ferromagnetic film materials includ-

ing [(Co(t_{Co})/Pt(t_{Pt})]N, [Co(t_{Co})/Pd(t_{Pt})]$_N$, [$Co_xNi_{(1-x)}$(0.6nm)/Pt(0.7nm)]$_3$ and [Co/Ni]$_N$ multilayer structures where we have varied several material parameters (t_{Co}, t_{Pt}, N and Ni concentration) that change the material magnetic properties such as magnetization, T_C, anisotropy and exchange.

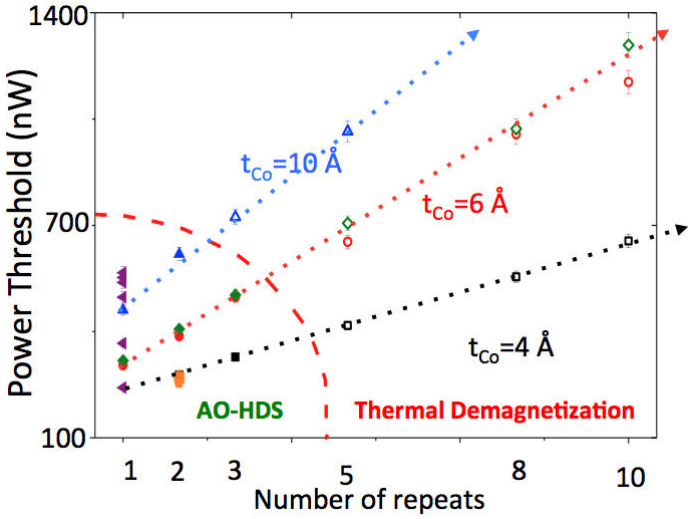

Figure 3.8: Threshold power and magneto-optical response to circular polarization light for ferromagnetic multilayer films versus N for [Co(t_{Co})/Pt(0.7 nm)]$_N$ samples with t_{Co} = 0.4, 0.6 and 1.0 nm. Plotted is the evolution of the threshold power to achieve either TD or AO-HDS of various samples. For each sample, the threshold power is given either as a filled symbol for AO-HDS or open symbols for TD.

AO-HDS is observed in all these ferromagnetic materials classes including single Co layers sandwich between Pt layers. Figure 3.8 to 3.11 summarizes selected results for the threshold laser power needed to achieve either AO-HDS (solid symbols) or TD (open symbols). For [Co(t_{Co})/Pt(0.7nm)]N multilayers the results (Fig. 3.8) show AO-HDS for N = 2 or 3 and $t_{Co} \leq$ 0.6 nm (i.e., the thinnest samples) and TD for thicker samples (consistent with Fig. 3.7). The threshold laser power increases linearly with both N and t_{Co} and these trends are independent of AO-HDS or TD final states.

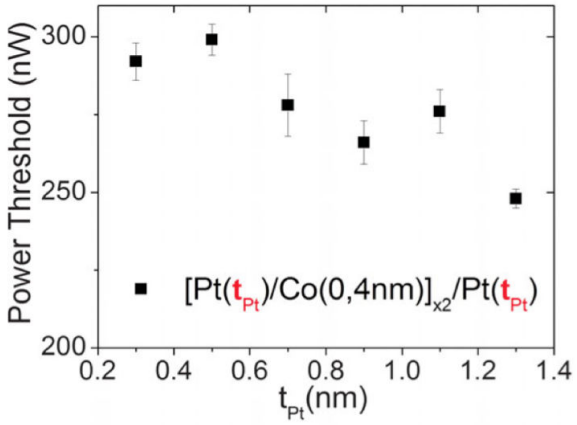

Figure 3.9: Threshold power and magneto-optical response to circular polarization light for ferromagnetic multilayer films versus t_{Pt} for [Co(0.4 nm)/Pt(t_{Pt})]$_2$ multilayer samples. Plotted is the evolution of the threshold power to achieve AO-HDS on various samples.

For [Co(0.4 nm)/Pt(t_{Pt})]$_2$ samples (see Fig. 3.9) the threshold power decreases slightly with increasing Pt thickness. For N = 1 trilayer structures, i.e., Pt/Co(t_{Co})/Pt (see Fig. 3.10) we observed AO-HDS for 0.6 nm $\leq t_{Co} \leq$ 1.5 nm. The upper limit is set by the thickness where the sample

maintains perpendicular magnetic anisotropy and lower limit by the sensitivity of the optical detection. The threshold power increases linearly with t_{Co} and the values for single Co layers are consistent with the extrapolation of the data in Fig. 3.8 to N = 1.

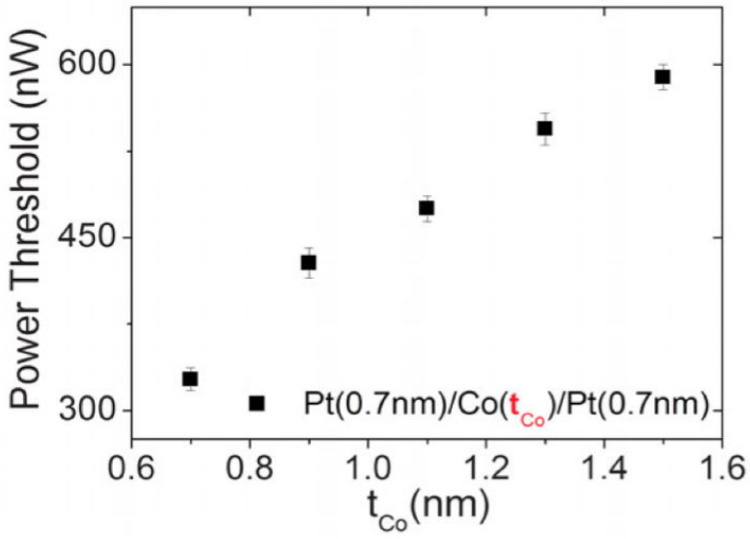

Figure 3.10: Threshold power and magneto-optical response to circular polarization light for ferromagnetic multilayer films versus t_{Co} for Pt/Co(t_{Co})/Pt trilayer samples. Plotted is the evolution of the threshold power to achieve either TD or AO-HDS of various samples. For each sample, the threshold power is given either as a filled symbol for AO-HDS or open symbols for TD.

For $[Co_{(1-x)}Ni_x(0.6nm)/Pt(0.7nm)]_N$ multilayers as a function of both N and Ni concentration the threshold power increases with N as seen in Fig. 3.11 and decreases with Ni concentration. Finally AO-HDS is seen for a Cu(10nm)/[Ni(0.5nm)/Co(0.1nm)]$_2$/Ni(0.5nm)/Cu(5nm) multilayer.

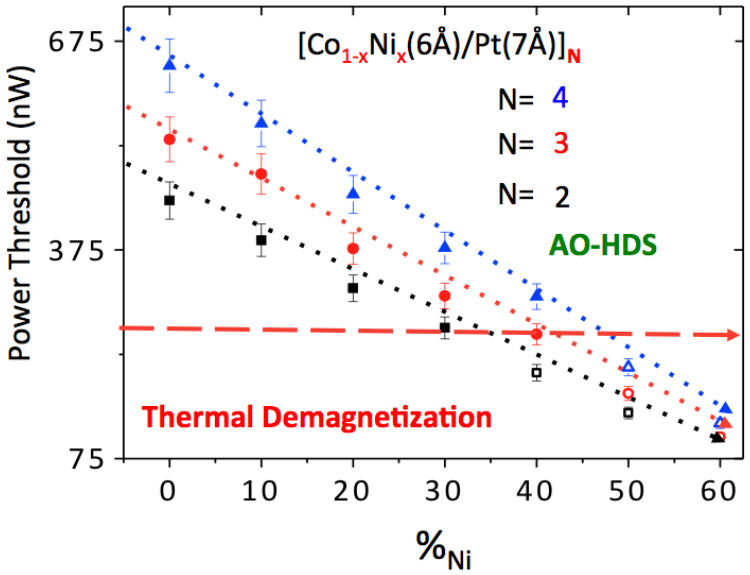

Figure 3.11: Threshold power and magneto-optical response to circular polarization light for ferromagnetic multilayer films versus Ni concentration for $[Co_{(1-x)}Ni_x(0.6\ nm)/Pd(0.7\ nm)]_N$, with N = 2, 3 or 4 repeats. Plotted is the evolution of the threshold power to achieve either TD or AO-HDS of various samples. For each sample, the threshold power is given either as a filled symbol for AO-HDS or open symbols for TD.

3.3.2 High Anisotropy Magnetic Materials

Optical Response of FePt-$L1_0$

We studied the role of AO-HDS in combination with applied magnetic fields on high-anisotropy FePt-based HAMR media[222]. The media are FePtAgC and FePtC granular films which form high-anisotropy FePt grains separated by C grain boundaries. The average grain size is $\sim$ 9.7 nm and $\sim$ 7.7 nm for the FePtAgC and FePtC, respectively (see Fig. 2.37). The room-temperature magnetic anisotropy and coercive fields are 7 T and 3.5 T, respectively (see Fig. 3.12 in section 2).

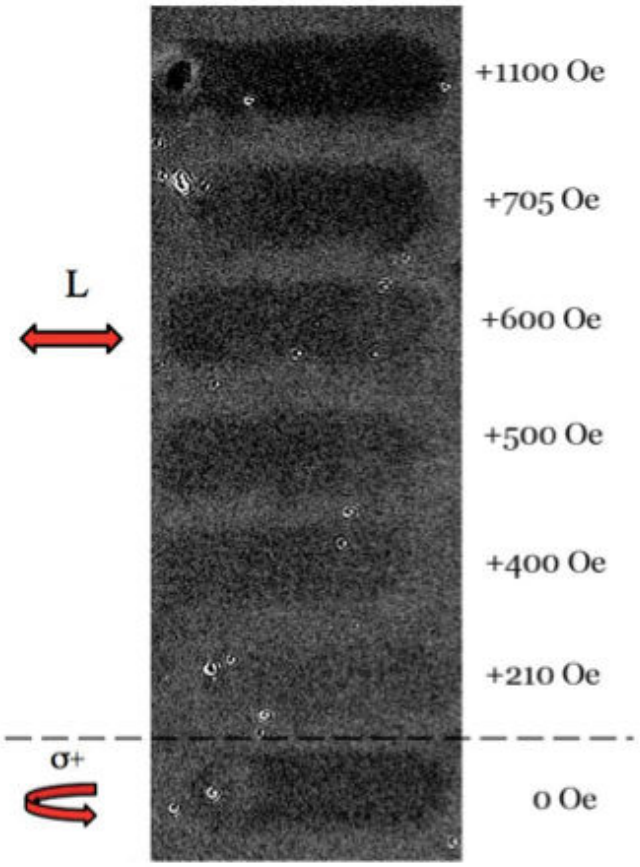

Figure 3.12: Magneto-optical response of the FePtAgC sample. Shown are a line scan for right circular polarization in zero applied field (bottom) and line scans for linear polarization with increasing applied magnetic field. The magnitude of the field is shown in the right of the image.

Figure 3.13 are optical results on the FePtAgC granular film which is initially in a random magnetic state with equal up or down oriented magnetic grains. Because the grain size is well below the resolution of the Faraday microscope the randomly magnetized sample appears grey. Figure 3.13 (a) shows there is a net magnetization achieved that depends on the helicity of the circularly polarized light, while no change is observed with linear polarization. This clearly demonstrates that the film magnetization is controlled by the polarization of the light.

Figure 3.13 (b) are images recorded without scanning the laser beam as in Fig. 3.13 (d). With increasing power above the threshold power (420 nW) there is a region of reversed grains. Above 600 nW a ring forms where AO-HDS occurs at a particular radius consistent with a relatively narrow range of powers to achieve AO-HDS. The center of the ring where the laser intensity is the highest is demagnetized (TD-behavior), presumably exceeding T_C.

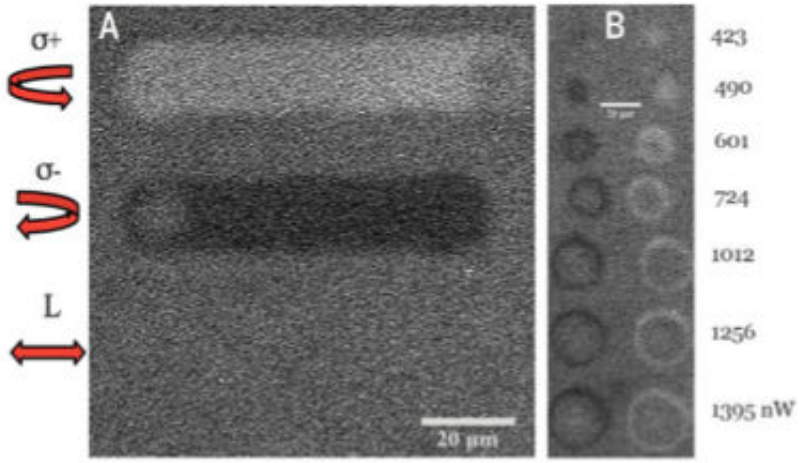

Figure 3.13: Magneto-optical response in zero applied magnetic field of a 15-nm FePtAgC granular film sample starting with an initially demagnetized sample. (a) Line scans for σ^+, $\sigma-$, and linear polarized light (L). The laser beam was swept over the sample, and the magnetization pattern was subsequently imaged. (B) Images of magnetic domains written by keeping the laser spot at a fixed position on the sample. The laser was either σ^+ polarized (left column) or σ^- polarized (right column). The laser power is given next to the image.

While AO-HDS is observed the degree of magnetization is less than 100%. By comparing the contrast to the saturated film the estimate of the induced magnetization is 10-20% of saturation. The lack of saturation can arise from at least two effects. The first is that AO-HDS is only affecting a subset of the grains. The second, and more likely, is that the magnetic grains are highly thermally activated. Near T_C there is a strong drop in K_u and the magnetic energy stored in the grain K_uV (where V is the volume of the grain) becomes comparable to thermal energy k_BT and the particles are superparamagnetic. During the sample cooling after the optical pulse the grain assembly can partially demagnetizes due to thermal switching of individual grains (see discussion in ref.[169]]. This effect is further driven by the dipolar fields from the neighboring grains that support a demagnetized ground state.

To quantify the role of thermal activation on AO-HDS, an external magnetic field was applied while the sample was illuminated by the polarized light. Figure 3.14 are the results of line scans with both circular polarizations for different external magnetic field. An applied field of 700 Oe is sufficient to suppress the effects of the helicity of the light where no contrast is observed for σ^-. For σ^+ the contrast increases with increasing field. Similarly, we can excite the films with linear polarized light and an applied field of 600 Oe yields a similar optical contrast as the AO-HDS results (see Fig. 2.39). The fact that these modest fields (relative to the room-temperature coercive field) are sufficient to magnetize the sample and/or counter the polarization of the light indicates that the sample is heated by the laser near T_C. Moreover the grains are highly thermally activated during the optical excitation, as an external field up to 1100 Oe is not sufficient to fully saturate the film.

3.4 Model

Our results show that AO-HDS is not exclusive to ferrimagnetic materials and therefore antiferromagnetic exchange coupling between two magnetic sublattices is not required. Given that we observe AO-HDS switching on single Co films as well as Co/Pt and Co/Ni multilayers it is unlikely that super-

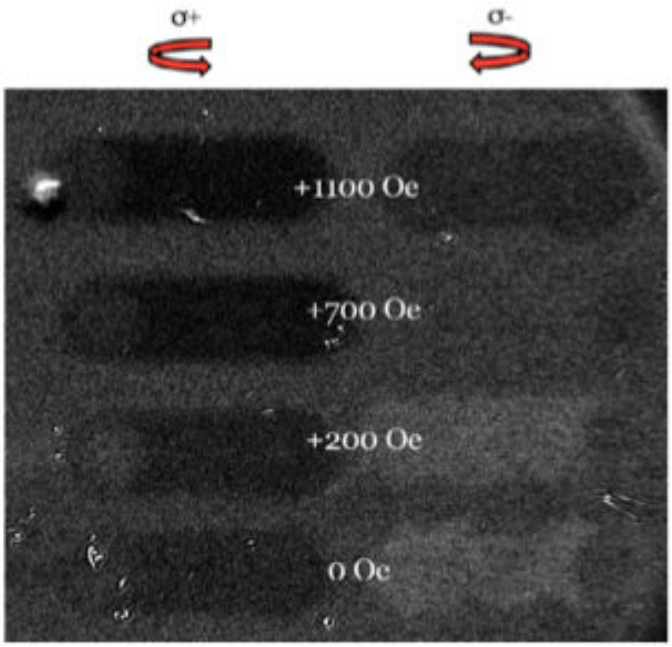

Figure 3.14: Magneto-optical response in various applied magnetic field of a 15-nm FePtAgC granular film sample starting with an initially demagnetized sample. Shown are line scans for $\sigma+$ circularly polarized light in the left column and σ^- left circularly polarized light in the right column. The laser power was 677 nW. The magnitude of the external magnetic field is given in the figures, and the orientation of the field supports σ^+ polarization and opposes the σ^- polarization.

diffusive currents that couple different magnetic regions in a heterogeneous sample are required. The results do suggest that heating near the Curie point is important for the AO-HDS in ferromagnetic materials as the threshold intensities for both AO-HDS and TD (Fig. 3.8) generally track with the expected trends for T_C and do not scale with parameters such as interlayer exchange or anisotropy. Near T_C the inverse Faraday effect or transfer of angular momentum from the light to the magnetic system is expected to be most effective. Recent modeling within the Landau-Lifshitz-Bloch formalism finds that achieving a nearly quenched magnetization is crucial for linear reversal under an ultrashort opto-magnetic field pulse arising from the inverse Faraday effect[207]. Well below T_C the magnetization reversal is precessional and governed by the Landau-Lifshitz-Gilbert equation. In the current geometry the opto-magnetic field is parallel to the magnetization, the least efficient for precessional switching[7]. Similarly when approaching T_C the transfer of the relatively modest angular moment in the light can lead to a symmetry breaking such that magnetization is deterministically switched.

The final ingredient for AO-HDS is that the magnetization state, once switched near T_C, be maintained while the sample cools. If demagnetization and thermal energies are too large then the sample will demagnetize during cooling. For perpendicular magnetized films there are strong dipolar fields within the film that support domain formation. The dipolar energy gain for domain formation is strongly suppressed in the ultrathin film limit and explains the observation of AO-HDS only in the thin-film limit (see Figs. 3.7 and 3.8 to 3.11). Domain formation is also suppressed in low magnetization materials consistent with AO-HDS measurements of ferrimagnetic materials[133].

Our model can be sketch as presented in figure 3.15 : (1) Light brings enough energy to the spin system that it reaches T_C ; (2) an effect capable of breaking the system symmetry takes place so that a part of the material switch toward one direction or the other depending on the light helicity. Note that for temperature close to T_C little angular momentum is needed to break the symmetry ;

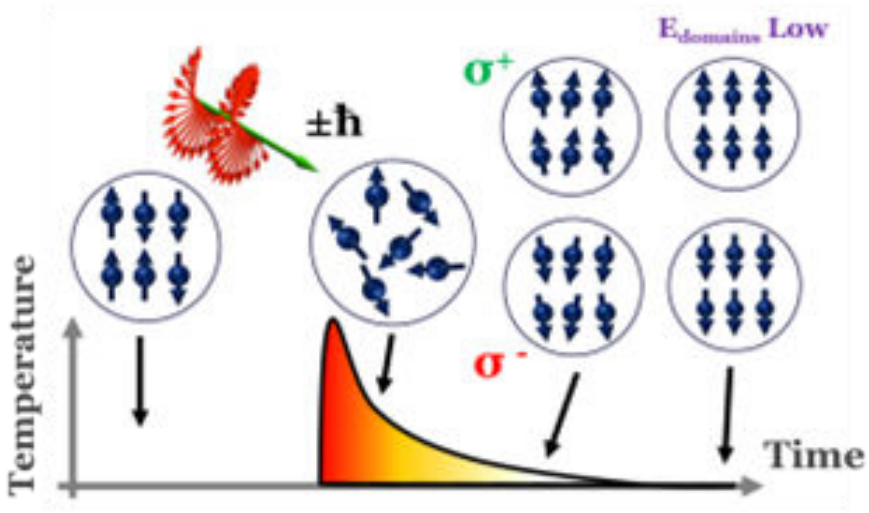

Figure 3.15: Schematic representation of the magnetization switching. (1) Strong heat accumulation that brings the system near the ordering temperature, (2) Symmetry breaking depending on helicity, (3) Conservation of the preferential orientation during cooling thanks to a low demagnetization energy.

(3) the cooling process and the material property need to be such that the magnetization direction is maintain and the system does not break into domain. This is the reason why two classes of material show AO-HDS. The first one show low magnetization for temperature between room temperature and Curie temperature. Those are typically ferrimagnetic materials with a compensation temperature above room temperature. The second one are very thin layers and the domain created are large. In both case the energy gain by creating magnetic domains is low.

Concerning step (2) unfortunately our study does not shed much light on the origin of the mechanism. We can state that it is a very general effect since it seems that we are only limited by step (3). However the process could be either related to an angular momentum transfer or to pure heat transfer knowing that heat absorption depends on the helicity.

The present results on ferromagnetic materials demonstrate a new and technologically important class of materials showing AO-HDS and opens new directions in integrated magnetic-optical memory, data storage and processing applications. This study further offers progress toward a better understanding of the interaction between pulsed polarized light and magnetic materials.

3.5 Field influence during beam exposure

Temperature profile upon irradiation

A lot of simulation can be done to deduce the temperature of the three reservoirs defined in section 1.3.2 upon the exposure to ultrafast laser. However the measure of such parameter is usually indirect and it seems impossible to separate the different contributions in a real system. A first idea can be of course given by the knowledge of the magnetic properties upon static heating or cooling. We have already shown that the power threshold is related to the Curie temperature of the system in ferromagnetic samples. We found out that it is also the case for ferrimagnetic samples where we can even highlight the two characteristic temperature of the system, namely the compensation and Curie temperatures. To do so we used some GdFeCo samples of different composition and by combining an external magnetic field upon irradiation we were able to see the area were the system is RE- or

TM-driven.

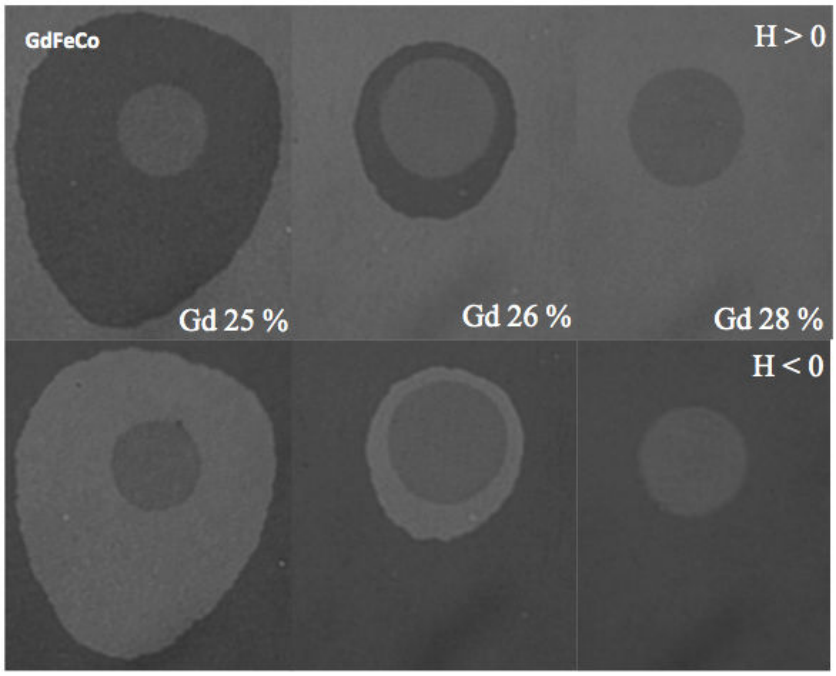

Figure 3.16: Evolution of the reversed area with the Gd composition. The power and beam size is kept constant for the three pictures. All pictures have the same dimensions.

In Fig. 3.16 we can see the domain formation for a same power light on three different GdFeCo samples with an applied external magnetic field used during the exposure. Depending on the composition the two compensation and Curie temperatures are tuned as shown experimentally by Hansen et al.[75,76]. Gd 25 % is characterized by the lowest T_{Comp} and the highest T_C and consequently needs very little energy to heat the sublattices to the compensation but a much higher one to reach the ordering temperature. With the increasing Gd component such as the Gd 26 % sample the compensation increases while the Curie temperature is lowering to finally end in the case of Gd 28 % where both of them are very close to each other.

Upon the exposure with our ultrafast laser the beam profile can be considered as a thermal profile too : the closer to the center the higher the temperature. So the addition of an external field uniform over the whole surface with the beam active is responsible for different evolutions of the magnetism depending on the position. Indeed below and above the compensation the net magnetization is not driven by the same component of the RE-TM alloy. In each of the two areas (below and above compensation) its the dominant sublattice that is oriented along the magnetic field. But as the Faraday imaging setup is only sensitive to the TM sublattice the FeCo magnetization will be following two opposite directions as we go farther from the center. This is responsible for the donut shape highlighted in Fig. 3.16 with two different domains depending on the position from the beam center.

The three different samples have different T_{Comp} and T_C so the size of the domains corresponds to the separated evolution of each of them. As illustrated in Fig. 3.17 the position of the limit between the two saturated part (black or white domain) is moving with T_{Comp}. On the other side the T_C is decreasing with increasing the Gd part so an increasing part of the beam will be at a temperature above T_C if we keep the power constant. This can be observe in Fig. 3.16 where we see the grey area in the middle that grows from left to right. In this area the system is in a paramagnetic state and a small external field applied in one of the two direction is enough to switch the system. However in

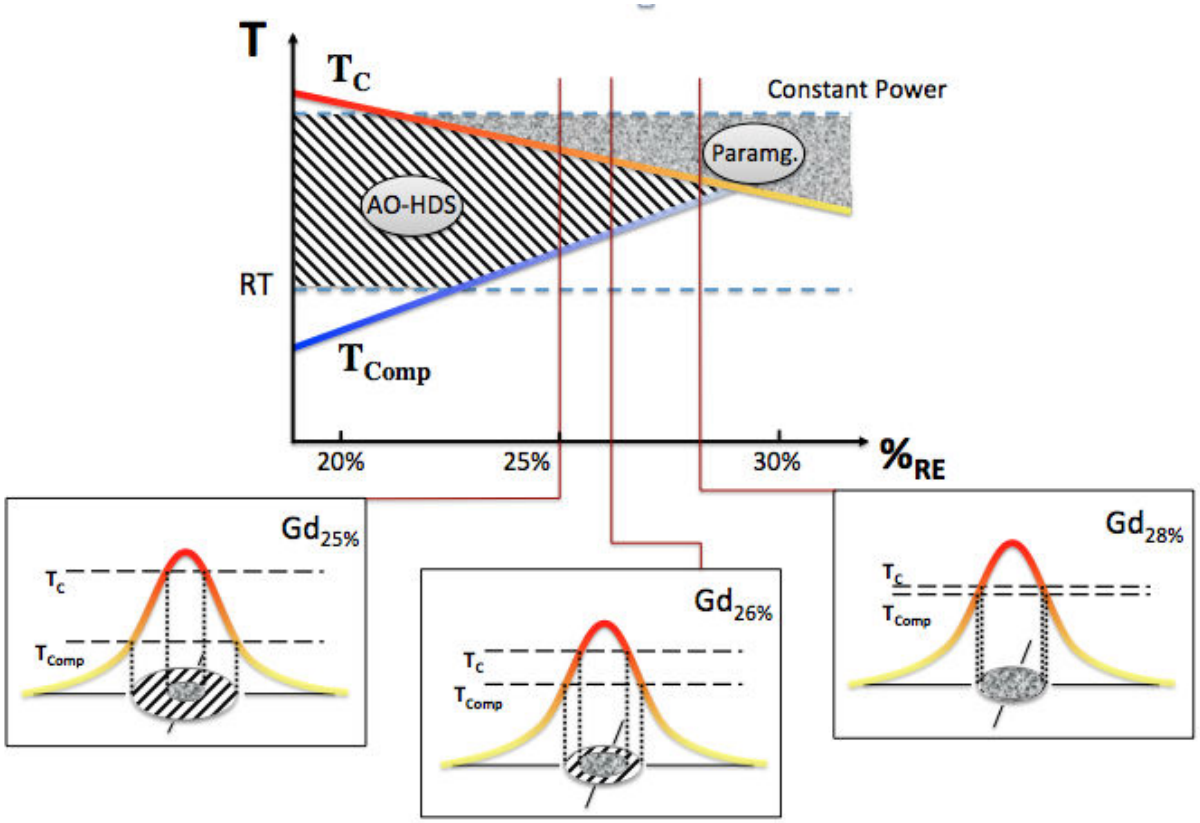

Figure 3.17: Schematic representation of the reversed area depending on the distance to compensation.

contrary to the AO-HDS region in the phase diagram 3.17 any part of the sample in the paramagnetic region will directly go back to a random state if we switch off the beam. In the case of the AO-HDS region the sample leaves behind the characteristic donut shape.

Field influence on beam sweeping

We further explored the laser induced AO-HDS and TD combining the effect of light and an external magenetic field in Fig. 3.18 to 3.20.

In Fig. 3.18 are the results for the $[Co(0.4\ nm)/Pt(0.7nm)]_3$ multilayer sample shown in Figs. 3.7 (c) and (d) in the last section. At room temperature this sample exhibits a square hysteresis loop with a coercive field of 204 Oe (see Fig. 2.21 in chapter 2). Line scans for different helicities (left and right circular polarization and linear polarization) are shown for increasing magnetic fields. In the left image (+) and the middle image (-) an applied field opposes the helicity of the light. When the helicity of the external magnetic field opposes the helicity of the light an external magnetic field of 7 Oe is yields a demagnetized film while 11.5 Oe will saturate the film in the field direction and opposite to the AO-HDS direction. For linear light an external field of ~ 3 Oe is needed to achieve saturation.

In Fig. 3.19 are the results for the $[Co(0.4\ nm)/Pt(0.7nm)]_5$ multilayer sample shown in Fig 3.7 (b) in the last section. At room temperature this sample exhibits a square hysteresis loop with a coercive field of 297 Oe. Line scans for different helicities (left and right circular polarization and linear polarization) with increasing magnetic fields are shown. In the left image the helicity of the light and the magnetic field support the magnetization of the sample. Conversely for the middle images the applied field opposes the helicity of the light. The right images are for linear polarization. When the helicity of the light supports the external magnetic field an external magnetic field of 7 Oe

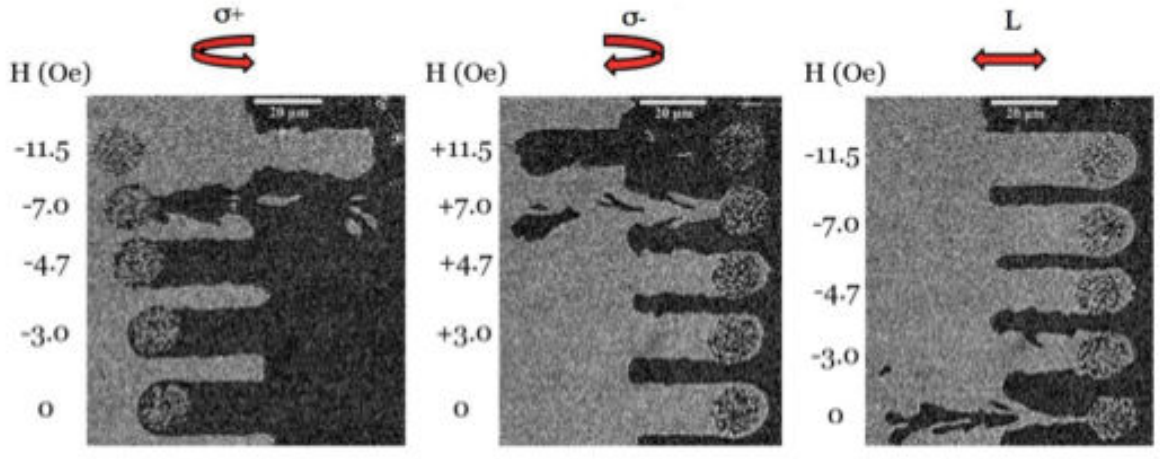

Figure 3.18: Magnetic response of a $[Co(0.4\ nm)/Pt(0.7nm)]_3$ multilayer to the combined effect of optical excitation and an external magnetic field starting with two domains and a domain wall in the middle of each image. The magnitude of the magnetic field is shown to the left of each line scan and the average laser power was 523 nW.

is needed to saturate the film. Conversely for same applied field and the opposite helicity requires an external field of 21-25 Oe to achieve saturation indicating a clear helicity dependent response. For linear light an external field of $\sim$ 12 Oe is needed to achieve saturation.

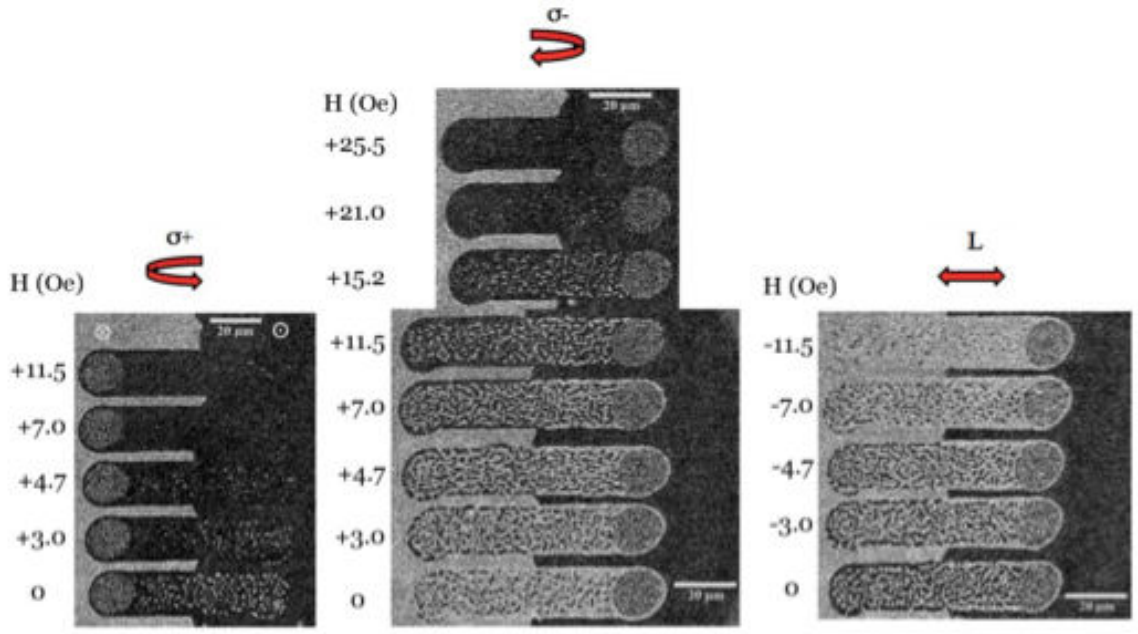

Figure 3.19: Magnetic response of a $[Co(0.4\ nm)/Pt(0.7)]_5$ multilayer to the combined effect of optical excitation and an external magnetic field starting with two domains and a domain well in the middle of each image. The magnitude of the magnetic field is shown to the left of each line scan and the average laser power was 720 nW.

In Fig. 3.20 are the results obtained on the $[Co(0.4\ nm)/Pt(0.7nm)]_8$ multilayer sample presented in Fig 3.7 (a) of the last section. At room temperature this sample exhibits a square hysteresis loop with a coercive field of 368 Oe. What is shown are line scans for different helicities (left and right circular polarization and linear polarization) with increasing applied magnetic fields. In zero applied field the sample shows TD as seen in Fig. 3.7 (a) but with increasing applied field the contrast in the

area where the laser is swept increases. A field on the order of 35-40 Oe is needed to saturate the film. When comparing left circular polarized light with linear polarized light that have same applied magnetic fields the results are very similar indicating the helicity of the light is not contributing to the final state of the magnetization.

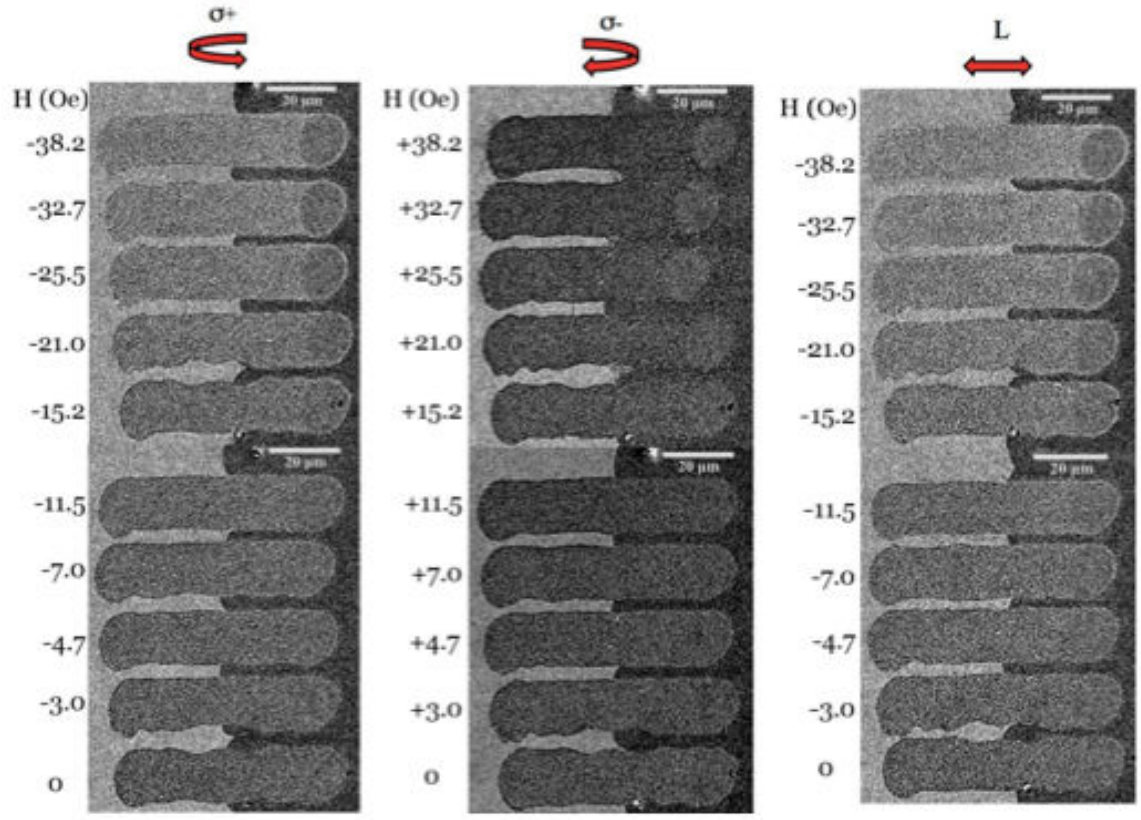

Figure 3.20: Magnetic response of a $[Co(0.4\ nm)/Pt(0.7nm)]_8$ multilayer to the combined effect of optical excitation and an external magnetic field starting with two domains and a domain well in the middle of each image. The magnitude of the magnetic field is shown to the left of each line scan and the average laser power was 682 nW.

Using this method we explored the effective driving energy for AO-HDS and domain formation (TD) by adding external magnetic fields to the experiments. While linear polarization leads to domain formation in zero applied field the application of a magnetic field can stabilize a uniform magnetization state. This field increases from 3-4 Oe for the N = 3, to $\sim$ 12 Oe for N = 5 and $\sim$ 40 Oe for N = 8 demonstrating the increased dipolar energy with thickness.

When the applied field is combined with circular polarization the applied field can either support or oppose the circular polarization. For N = 3 a field of 7 Oe opposes the circular polarized light and yields a demagnetized film while a field of $\sim$ 12 Oe will saturate the film in the opposite direction as that expected for the helicity of the light (see Fig. 3.20). For N = 5 the field to yield a demagnetized film is $\sim$ 12 Oe while a field of $\sim$ 25 Oe is needed to saturate the film opposite to the light helicity (see Fig. 3.19). Fig. 3.21 and 3.22 sums up the evolution of the magneto-optical response for the three different helicities on the samples with 3 to 8 repeats. As we can see the evolution is very similar between the two films, however it is the multi-domain pattern located between the two monodomain states that is increasingly growing with the number of repeats. One has to add an increasing external magnetic energy to the system to stabilize a monodomain state has the system cools down. We see that the addition of the magnetic field progressively favors one of the two orientations by unbalancing the

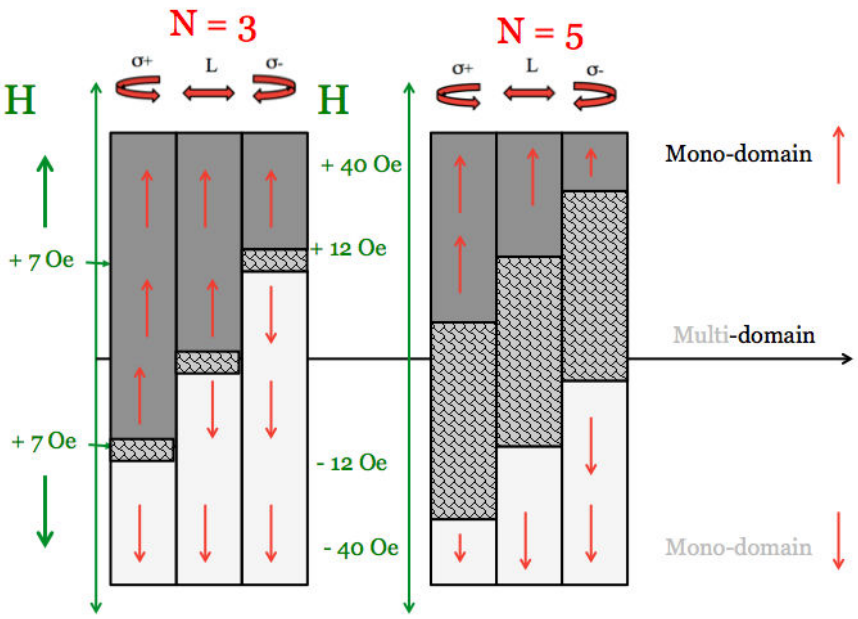

Figure 3.21: Schematic representation of the magnetic response of $[Co(0.4\ nm)/Pt(0.7nm)]_N$ multilayer for $N = 3$ and 5 to the combined effect of optical excitation and an external magnetic field for the three different polarization available.

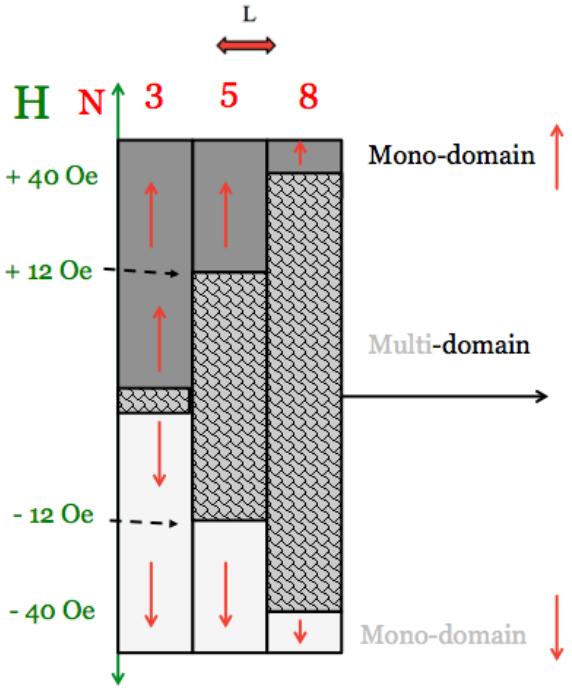

Figure 3.22: Schematic representation of the magnetic response of the three $[Co(0.4\ nm)/Pt(0.7nm)]_N$ multilayer for $N = 3$ and 5 and 8 to the combined effect of optical excitation and an external magnetic field for the a linear polarization. This effect is very similar to the observation with an helicity applied alone.

domain pattern as in Fig. 3.19 for example. This observation would suggest that any magnetic material would possibly be switched using circularly polarized light but it is the monodomain configuration that is in most of the case unstable and vanishes in the first picosecond of the magnetic recovery to end up in a multidomain state.

However, when comparing the effects of circular polarization of the light to the applied magnetic

field one has to remember that the magnetic field is applied during the entire thermal process while the role of the helicity of the pulse is believed to persist only for a few picoseconds after the laser excitation[82].

3.6 Discussion on the temperature Influence

A second way to obtain a deeper understanding of the all-optical helicity dependent switching phenomenon is to test how the system respond to a change in the optical excitation properties. Some works already looked into the influence of central wavelength, pulse chirp and some other purely optical parameter but instead we will try to understand the specific role of heat dissipation in the phenomenon. The data presented in this section show how the phenomenon develops depending on the pulse train. In detail, here we vary the repetition rate, exposure time, pulse length and try to relate it to the heat absorbed in the material. Furthermore we applied some magnetic field during the exposure to look at its influence on the final magnetization.

3.6.1 Repetition rate

During this thesis we had access to two different femtosecond lasers with similar characteristics except for the repetition rate. The first setup where most of the results presented here were obtained is a 1 kHz laser whereas the second one is a 5 kHz repetition. This parameter is particularly important in our case because of the sweeping procedure developed here. Indeed the repetition rate convoluted with the sweeping rate defines how much pulses is left for each consecutive position of the beam. If a sufficient high sweeping speed was originally used to spatially separate two pulses and observe the subsequent evolution this kind of apparatus was not available on our setups. In our case there is always several pulses reaching a same area and this is responsible for a certain heat accumulation in the sample. It is particularly true because of the nature of the substrate used. All samples were deposited on glass with a very small underlayer such as 3 to 5 nm of Ta or Pt which means that the heat has some difficulties to be dissipated as illustrated in fig 3.23. Between two pulses the system cannot come back to its original state and the temperature of the lattice progressively ramps up.

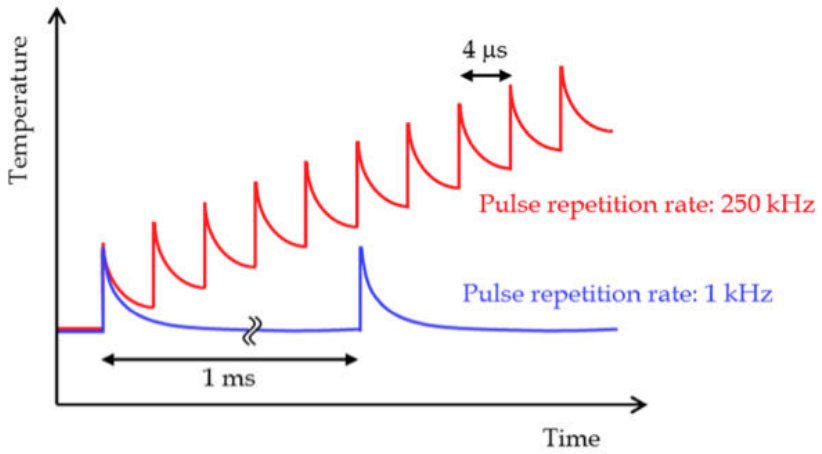

Figure 3.23: Schematic temperature profiles induced in an irradiated samples by femtosecond laser pulses at repetition rates of 1 kHz and 250 kHz. Figure extracted from *Miura et al.*[141]

In our case this appears with a modification of the limit between the AO-HDS and the TD final state. The 1 kHz repetition laser on CoPt favors AO-HDS for samples below 3 repetition, has a

transitional behavior at 4 repeats and fully induces domains for higher numbers of repeats (see fig 3.7). On the contrary the 5 kHz laser directly creates domain for 3 repetitions and develops AO-HDS for lower number of repeats.

This experiment can be compared to some recent work where the substrate[81] or the temperature of the system[80] were modified in order to investigate the temperature dependence of the AO-HDS. They found out that the not only the optical parameters are of importance but that the external parameters can also be tuned to control the switching. Since all this works has been done using quasi-static measurements it would be interesting to see how the ultrafast dynamics is modified using the same framework. In particular the response of different sublattices can be different hence giving a new way to challenge some of the theory existing at the moment.

3.6.2 Exposure Time

Once the evidence of a heat accumulation is proven due to the shift of the AO-HDS region for CoPt multilayers it is necessary to probe the time scale involved in the process. Thanks to a mechanical shutter along the beam axis we were able to modify the exposure time of the surface and then change the number of consecutive pulses reaching the sample. On figure 3.24 we compare the exposure for the three different polarization for a power slightly higher than the threshold power. We see that the formation of the switched area is not instantaneous and requires a certain number of pulses to stabilize to its final configuration. We used the 1 kHz laser so we can consider that 1 ms is equivalent to one pulse.

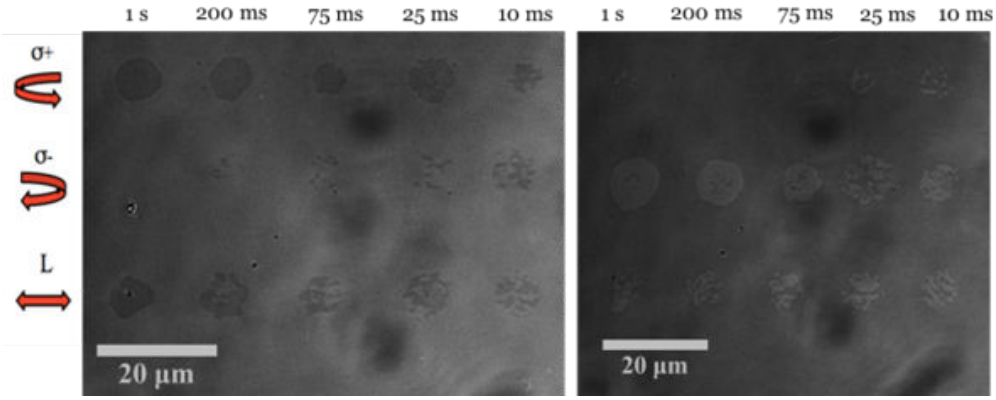

Figure 3.24: Evolution of the spot reversal for a threshold fluence and different exposure times.

For a small number of pulses the final state is multidomain while a single domain remains after enough time. This single domain is the equivalent of the AO-HDS rim presented in the previous section but using a lower power. In this context it could be that the system need to reach a certain quasi-static temperature to trigger the reversal. The phenomenon could be sensitive to the maximum temperature reached or more likely to the cooling sequence occurring once the beam is stopped (see fig 3.25). Similarly to the evolution with the repetition rate, the magnetization needs to be quenched in its switched state before the temperature breaks the uniform magnetization.

Another way to highlight the influence of the exposure time is to sweep the beam at different speeds. As shown on figure 3.26 the material requires enough resting time at each position to reach its final state that corresponds to the slowest sweeping speed for this sample. This experiment confirms that its the lattice temperature that enters in consideration for the final state. Indeed the maximum temperature for the electron system is directly linked to the spatial profile of the beam whereas the

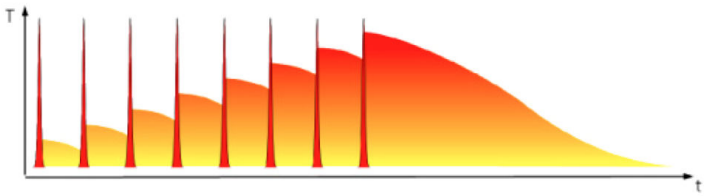

Figure 3.25: Schematic representation of the static heating existing upon constant irradiation of the sample with pulsed lasers. Figure extracted from Miura et al.[141]

lattice temperature mostly depends on the lateral dissipation of the heat. So in our case the electron temperature exactly fits to the beam shape whereas the quasi-static temperature is much broader and more blurred than the beam.

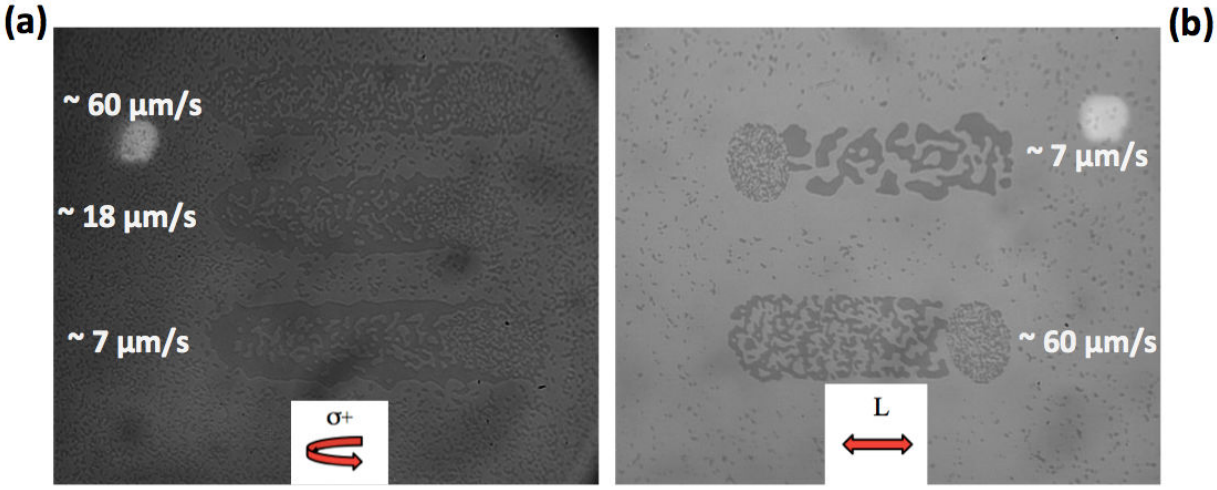

Figure 3.26: Evolution of a full multidomain pattern (b) and a transitional behavior with an AO-HDS rim (a) depending on the sweeping speed of the laser.

In particular we see that the domains are created in all the beam so the electronic temperature is driving the switching mechanism whereas the slow sweeping rate and its associated heat accumulation is stabilizing the final state. In addition this result is valid for RE-TM alloys such as CoTb even if the reversal in such systems is supposed to occur on a single pulse basis.

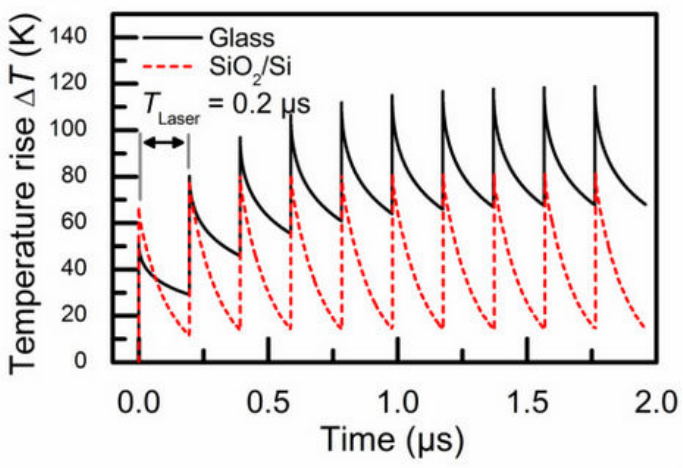

Figure 3.27: Calculated transient temperature of a $Tb_{30}Fe_{70}$ film on glass or SiO_2/Si substrate for laser pulses at a repetition rate of 5.1 MHz. Figure extracted from *Hassdenteufel et al.*[81]

This experiments tend to show that as described by the group from Manfred Albrecht[80,81] that the temperature of the material when the pulse hit the sample is important. This is for example illustrated in Fig. 3.27 where we see that a change in the substrate drastically change the temperature profile in the sample with consecutive pulses. If the peak temperature is increased it is more probably the static elevation of temperature represented by the slope of the minimum temperature that influence the AO-HDS phenomenon.

Summary

This thesis focuses on the understanding of the interaction between ultrashort laser pulses and magnetic materials. Among the different behaviors induced by ultrafast lasers we were interested in the possibility to manipulate magnetization without any applied external magnetic field and the different parameters required to obtain a stable switching. This domain of research is described as the All-Optical Helicity dependent Switching and the mechanisms involved are still highly debated. Our contribution to this field was to perform what can be qualified as a material study. Indeed we have grown a large number of magnetic thin films and tested if AO-HDS is observed. In our case we define AO-HDS as a full reversal of the magnetization in one direction for one helicity and the opposite direction for the opposite helicity in a stable manner.

The first part of this work shed light on the many different interactions involved in magnetism and in particular the different energies associated and that are acting at different timescale. However the advent of ultrafast optics made possible the stroboscopic study of such ultrashort transition and gives access to a whole new way to measure the response of magnetic materials. Instead of directly focusing on the quasi-static observation of magnetization as for usual novel magnetic phenomena such as polarized current reversal or electric field influence, the optical induced effects take place in a much quicker timescale. In this case new transient states can arise and vanish in the subpicosecond regime but they still can drive the system in metastable states that would not be accessible normally. In this framework the AO-HDS phenomenon is developing and gives full emphasize on ultrafast induced effects. On the other hand ultrafast pulses carry both heat and angular momentum to the system and it is hardly possible to disentangle their individual contributions. The AO-HDS seems to be a consequence of this two interacting aspects of ultrafast pulses and the microscopic mechanism in charge of the final state should reflect this duality.

For the first stages of the AO-HDS research field a lot has been done on the probing of the mechanism on a few rare earth (RE) - transition metals (TM) samples. Many improvements have been developed on the optical role of the phenomenon but stayed rather vague on the possible extend of it. Especially the GeFeCo used is a particularly complex material where the net magnetization comes from two different sublattices with well distinct origins for their magnetism. If the two individual contributions were eventually measured experimentally it remains unclear how they finally relate to the recovery of the magnetization after the laser excitation. Furthermore the small range of material available at this time did not permit a particular definition of the material parameters required for the switching to occur.

In this context we engineered many different materials and structures to see the extend of the AO-HDS phenomenon. Starting with the former RE-TM association we were interested in the role of

the heavy rare-earth element on the optical behavior. Thanks to very similar coupling properties the perpendicular anisotropy was achieved and different RE with intrinsically different atomic properties possible. We then were able to probe the structural sensitivity of the phenomenon by segregating the RE and TM atoms in a multilayer with tunable thicknesses and repeats.

A strong step forward was necessary to push even further the ferrimagnetic structure to basically mimicking artificially the RE-TM properties with a RE-free multilayer. The three main properties of interest of the RE-TM alloys were possibly tuned : the perpendicular anisotropy, the antiferromagnetic coupling between two sublattices and the compensation temperature.

The previous materials described were all presenting a ferrimagnetic structure which in fact was predicted by some articles to be a requirements for the AO-HDS phenomenon to appear. Inspired by the domain size evolution near the compensation composition at room temperature in RE-TM we investigated ferromagnetic structures with a much different approach than before. Instead of focusing only on the temperature evolution of the magnetization we wanted to test if its more the global demagnetization energy that could be the key parameter in the process. To do so a range of thin ferromagnetic multilayers were deposited using the same sputtering equipment as for all the materials presented in this thesis. Co/Pd, Co/Pt and Co/Ni multilayers with were the basic structures developed due to their compatibility with our optical measurement setup.

The final approach was to transpose our knowledge from regular ferromagnetic thin films to some of the high anisotropy materials that are already prospected for next generation of magnetic recording media. Out of the tremendous anisotropy existing in such materials, their microscopic structure with nanometer size grains could foresee a well different behavior through optical excitation.

Our study is based on the different possible final state of magnetization induced by a femtosecond laser. Most of the observations were done using a Faraday imaging setup that allows for a direct probing of the magnetic configuration in transparent magnetic materials. Even if the temporal resolution could not be compared to the one of pump-probe experiments this technic can use the spatial profile of the beam as a tool. The different zones and behaviors created in the spot size permit to seize the ingredients required for the AO-HDS. Indeed depending on the location on the beam and on the surface of the sample the balance between heat and angular momentum or the initial state of magnetization can be studied. Additional tools can be attached to the setup to get more quantitative informations or introduce some external bias to see how the AO-HDS is modified under such conditions.

The main part of this thesis was devoted to the understanding of the mechanism underlying the AO-HDS by systematically changing the characteristics of our materials. We find out some similarities between the different systems described earlier which help us build a model to describe the phenomenon. The ferrimagnetic systems highlight the role of the compensation temperature as a a key ingredient to reach an helicity dependent writing. The compensation temperature above room temperature means that while the system is cooling down after the pulse excitation it will pass through a state with a very low magnetization and its associated low demagnetization field that favors a monodomain state for the system (at least for a given region in the spot). The same characteristic is supposed to be responsible of the switching in rare-earth free ferrimagnets as we copied the RE-TM components to reach our goal.

On the other side, the ferromagnetic systems do not present any compensation temperature so in order to unify the two different systems it is necessary to consider another argument. In this case only

a low magnetic thickness allows a switching of the samples while a higher number of repeats leaves the full film in a multidomain state along the beam track. This observations can be related to the bigger domain size allowed in thinner samples. The demagnetization energy is much smaller which echoes on the domain stability. In this case the system once cooling down will favor large domains and through the impulse of the helicity will end up in a deterministic monodomain for the final state. Indeed the demagnetization energy in the case of very thin films is low which does not give a chance for the magnetization to break into domain during the magnetization recovery following the laser excitation.

A step further has been achieved thanks to the use of ferromagnetic granular thin films. This configuration that allows for a long-term stability of the magnetization through very high anisotropy materials is taking advantage of the small dimension of the grains. The limited dimensions only permit single domain to form in each of the grains so it overcomes the need for a large domain size that drives the mechanism in the regular ferromagnetic films. Granular media also point out the key role of the heat in the system. Using the similar approach as the one foreseen for HAMR technology the system has to be heated up close to the ordering temperature for the symmetry breaking to happen. As the system cools down the grains preferentially orient along the helicity of the beam however a full reversal has not been achieved in granular films at the moment. This observation might be related to the distribution in size, anisotropy or Curie temperature that is inherent to such kind of materials. A comparison with an external magnetic field has been done and gives an idea of the equivalent field that would be required to obtain the same results. Once again this direct comparison does not directly suit to the AO-HDS mechanism that is supposed to occur at ultrafast timescale but it allows the comparison with existing cases. Anyway the observation of AO-HDS in such materials opens up promising perspectives in the development of HAMR-like technologies.

Furthermore we gave an overview of the kind of stages that seems to happen through the exposure of a magnetic thin film to an ultrafast laser. In the very first femtosecond of the process the system reaches a temperature close to the ordering temperature that brings the spin system in a highly unstable configuration; then an effect is reorienting the spins along a given and deterministic direction that depends on the helicity of the laser; and if the demagnetization energy of the system is low it will relax back to a monodomain configuration. This process is in agreement with all the samples we measured and with the observations done previously in the domain.

Finally this thesis does not claim to shed light on the microscopic mechanism of the AO-HDS but it offers progress toward a better understanding of the interaction between pulsed polarized light and magnetic materials by greatly increasing the possibility of further studies. Additional experiments will be required to make the link between the quasi-static reversal we observe and the different models that are supposed to account for the ultrafast dynamics of such systems. At least the present results on ferromagnetic materials demonstrate a new and technologically important class of materials showing AO-HDS and opens new directions in integrated magneto-optical memory, data storage, and processing applications. In particular these results show that AO-HDS is a rather general phenomenon for ferromagnetic films but is only limited according to the thin-film limit, which is useful in a number of spintronic applications (e.g., magnetic random access memory).

Bibliography

[1] M. Agranat, S. I. Ashitkov, A. B. Granovskii, and G. I. Rukman, Sov. Phys. JETP **59** (1984), 804.

[2] L. Allen, M. Beijersbergen, R. Spreeuw, and J. Woerdman, Phys. Rev. A **45** (1992), 8185.

[3] and A. Garanin, Phys. Rev. B **55** (1997), 3050.

[4] and A. Kirilyuk, A. Kimel, and T. Rasing, Rep. Prog. Phys. **72** (2013), 026501.

[5] V. Antropov, M. Katsnelson, B. Harmon, M. van Schilfgaarde, and D. Kuznetsov, Phys. Rev. B **54** (1996), 1019.

[6] P. Argyres, Phys. Rev. **97** (1955), 334.

[7] C.H. Back, R. Allenspach, W. Weber, S.S.P. Parkin, D. Weller, Edward L. Garwin, and H.C. Siegmann, Science **285** (1999), 864–867.

[8] V. Baltz, A. Marty, B. Rodmacq, and B. Dieny, Phys. Rev. B **75** (2007), 014406.

[9] M. Battiato, K. Carva, and P. Oppeneer, Phys. Rev. Lett. **105** (2010), no. 2, 027203.

[10] J.-M.L. Beaujour, W. Chen, K. Krycka, C.-C. Kao, J. Z. Sun, and A. D. Kent, Euro. Phys. J. B **59** (2007), 475–483.

[11] E. Beaurepaire, J.-C. Merle, A. Daunois, and J.-Y. Bigot, Phys. Rev. Lett. **76** (1996), 4250.

[12] E. Beaurepaire, G. Turner, S. Harrel, M. Beard, J.-Y. Bigot, and C. Schmuttenmaer, Appl. Phys. Lett. **84** (2004), 3465.

[13] P. Beauvillain, A. Bounouh, C. Chappert, R. Mégy, S. Ould-Mahfoud, J. Renard, P. Veillet, D. Weller, and J. Corno, J. of Appl. Phys. **76** (1994), no. 10, 6078–6080.

[14] D. Bedau, H. Liu, J. Bouzaglou, A. Kent, J. Sun, J. Katine, E. Fullerton, and S. Mangin, Appl. Phys. Lett. **96** (2010), no. 2, 022514.

[15] R. Beth, Phys. Rev. **50** (1936), 115–125.

[16] J.-Y. Bigot, M. Vomir, and E. Beaurepaire, Nat. Phys. **5** (2009), 515.

[17] F. Bloch, Phys. Rev. **70** (1936), 460.

[18] S. Blundell, Oxford University Press, 2006.

[19] A. Borzsonyi, A. P. Kovacs, and K. Osvay, Appl. Sciences **3** (2013), 515–544.

[20] F. Den Broeder, W. Hoving, and P. Bloemen, J. Magn. Magn. Mater. **93** (1991), 562–570.

[21] W. Brown, Phys. Rev. **100** (1955), 1243.

[22] P. Bruno, J. Phys. Condens. Matter **11** (1999), 9403.

[23] K.H.J. Buschow, P.G. van Engen, and R. Jongebreur, J. Magn. Magn. Mat. **38** (1983), 1.

[24] I. A. Campbell, J. of Phys. F: Metal Physics **2** (1972), L47.

[25] K. Capelle, G. Vignale, and B. Györffy, Phys. Rev. Lett. **87** (2001), 206403.

[26] P. Carcia, J. Appl. Phys. **63** (1988), 5066.

[27] P. Carcia, A. Meinhaldt, and A. Suna, Appl. Phys. Lett. **47** (1985), no. 2, 178–180.

[28] P.F. Carcia, Proc. Intern. Symp. on Physics of Magnetic Materials **240** (1987), 1.

[29] P.F. Carcia, A.D. Meinhaldt, and A. Suna, Appl. Phys. Lett. **47** (1985).

[30] A. Cavalleri, Cs. Toth, C. W. Siders, J. A. Squier, F. Raksi, P. Forget, and J. C. Kieffer, Phys. Rev. Lett. **87** (2001), 237401.

[31] P. Chaudhari, J. Cuomo, and R. Gambino, Appl. Phys. Lett. **22** (1973), 337.

[32] A. Chernyshov, M. Overby, X. Liu, J. Furdyna, Y. Lyanda-Geller, and L. P. Rokhinson, Nat. Phys. **5** (2009), 656–658.

[33] D. Chiba, M. Sawicki, Y. Nishitani, Y. Nakatani, F. Matsukura, and H. Ohno, Nature **455** (2008), 7212.

[34] D. Chiba, M. Yamanouchi, F. Matsukura, and H. Ohno, Science **301** (2003), 943.

[35] O. Chubykalo-Fesenko, U. Nowak, R. Chantrell, and D. Garanin, Phys. Rev. B **74** (2006), 094436.

[36] W. Coffey, D. Crothers, J. Dormann, L. Geoghegan, Y. Kalmykov, J. Waldron, and A. Wickstead, Phys. Rev. B **52** (1995), 15951.

[37] C. Cohen-Tannoudji, J. Dupont-Roc, and G. Grynberg, Wiley, 1989.

[38] G. Crabtree, Phys. Rev. B **16** (1977), 1117.

[39] G. Daalderop, P., Kelly, and F. den Broeder, Phys. Rev. Lett. **68** (1992), 682–685.

[40] F. J. A. den Broeder, H. C. Donkersloot, H. J. G. Draaisma, and W. J. M. de Jonge, J. Appl. Phys. **61** (1987), 4317.

[41] F. J. A. den Broeder, H. W. van Kesteren, W. Hoving, and W. B. Zeper, Appl. Phys. Lett. **61** (1992), 1468.

[42] J. Van der Ziel, P. Pershan, and L. Malmstrom, Phys. Rev. Lett. **15** (1965), no. 5, 190.

[43] J.-C. Diels, Academic Press, 1996.

[44] Y.F. Ding, J.S. Chen, E. Liu, C.J. Sun, and G.M. Chow, J. Appl. Phys. **97** (2005), 10.

[45] M. Djordjevic and M. Münzenberg, Phys. Rev. B **75** (2007), 012404.

[46] H. J. G. Draaisma, W. J. M. de Jonge, and F. J. A. den Broeder, J. Magn. Mag. Mater. **66** (1987), 351.

[47] J. Dubowik, Phys. Rev. B (1996).

[48] D. Edwards and J. Hertz, J. Phys. F: Met. Phys. **3** (1973), 2191.

[49] W. Eerenstein, N. D. Mathur, and J. F. Scott, Nature **442** (2006), 7104.

[50] R. Elliott, Phys. Rev. **96** (1954), 266.

[51] B. Engel, C. England R. Van Leeuwen, M. Wiedmann, and C. Falco, Phys. Rev. Lett. **67** (1991), no. 14, 1910.

[52] B. Engel, M. Wiedmann, R. Van Leeuwen, and C. Falco, Phys. Rev. B **48** (1993), no. 13, 9894.

[53] L. Ertl, G. Endl, and H. Hoffmann, J. Magn. Magn. Mater. **113** (1992), 227–237.

[54] R. F. L. Evans, R. W. Chantrell, U. Nowak, A. Lyberatos, and H.-J. Richter, Appl. Phys. Lett. **100** (2012), 102402.

[55] B.-G. Fabrice, Ph.D. thesis, Université Joseph Fourier - Grenoble I, 2004.

[56] M. Fanle and D. Steiauf, Phys. Rev. B **73** (2006), 184427.

[57] M. Faraday, Phil. Trans. R. Soc. Lond. **136** (1846), 104–23.

[58] N. Del Fatti, C. Voisin, M. Achermann, S. Tzortzakis, D. Christofilos, and F. Vallée, Phys. Rev. B **61** (2000), no. 24, 16956.

[59] J. A. Fernandez-Baca and W.-Y. Ching, World Scientific Publishing Co. Pte. Ltd., 1995.

[60] S. Foner, Rev. Sci. Instrum. **30** (1959), 548–557.

[61] K. Fukumoto, Ph.D. thesis, Freien Universitat Berlin, 2005.

[62] A. Garanin, Physica A **172** (1991), 470.

[63] P. F. Garcia, J. Appl. Phys. **63** (1988), 5066.

[64] P. F. Garcia, A. D. Meinhaldt, and A. Suna, Appl. Phys. Lett. **47** (1985), 178.

[65] J. Gay and R. Richter, Phys. Rev. Lett. **56** (1986), no. 25, 2728.

[66] G. Genkin, Y. Nozdrin, A. Okomelkov, and I. Tokman, Phys. Rev. B **86** (2012), 024405.

[67] S. Gepraegs, A. Brandlmaier, M. Opel, R. Gross, and S. T. B. Goennenwein, Appl. Phys. Lett. **96** (2010), 14.

[68] T. Gerrits, H. van den Berg, J. Hohlfeld, L. Bahr, and T. Rasing, Nature **418** (2002), 509.

[69] K. Gilmore, Y. Idzerda, and M. Stiles, Phys. Rev. Lett. **99** (2007), 097601.

[70] D. Gopman, D. Bedau, S. Mangin, C.-H. Lambert, E. Fullerton, J. Katine, and A. Kent, Appl. Phys. Lett. **100** (2012), 062404.

[71] S. Alebrand M. Gottwald, M. Hehn, S. Steil, M. Cinchetti, D. Lacour, E. Fullerton, M. Aeschlimann, and S. Mangin, Appl. Phys. Lett. **101** (2012), 162408.

[72] U. Gradmann, J. Magn. Magn. Mater. **54** (1986), 733.

[73] U. Gradmann and J. Müller, Phys. Status solidi **27** (1968), no. 1, 313–324.

[74] C. E. Graves, A. H. Reid, T. Wang, B. Wu, S. de Jong, K. Vahaplar, I. Radu, D. P. Bernstein, R. Coffee M. Bionta S. W. Epp R. Hartmann N. Kimmel M. Messerschmidt, L. Müller, G. Hauser, A. Hartmann, P. Holl, H. Gorke, J. H. Mentink, A. Tsukamoto, A. Fognini, D. Rolles H. Soltau L. Strüder J. J. Turner, W. F. Schlotter, Y. Acremann, A. V. Kimel, A. Kirilyuk, J. Stöhr Th. Rasing, A. O. Scherz, and H. A. Dürr, Nat. Mat. **12** (2013), 293–298.

[75] P. Hansen, C. Clausen, G. Much, M. Rosenkranz, and K. Witter, J. Appl. Phys. **66** (1989), 756.

[76] P. Hansen, S. Klahn, C. Clausen, G. Much, and K. Witter, J. Appl. Phys. **69** (1991), 3194.

[77] S. Hashimoto, J. Appl. Phys. **75** (1994), 438.

[78] S. Hashimoto, Y. Ochiai, and K. Aso, J. Appl. Phys. **67** (1990), 4429.

[79] A. Hassdenteufel, B. Hebler, C. Schubert, A. Liebig, M. Teich, M. Helm, M. Aeschlimann, M. Albrecht, and R. Bratschitsch, Adv. Mat. **25** (2013), no. 22, 3122–3128.

[80] A. Hassdenteufel, J. Schmidt, C. Schubert, B. Hebler, M. Helm, M. Albrecht, and R. Bratschitsch, Phys. Rev. B **91** (2015), 104431.

[81] A. Hassdenteufel, C. Schubert, B. Hebler, H. Schultheiss, J. Fassbender, M. Albrecht, and R. Bratschitsch, Optics express **22** (2014), no. 8, 10017–10025.

[82] S. Alebrand A. Hassdenteufel, D. Steil, M. Cinchetti, and M. Aeschlimann, Phys. Rev. B **85** (2012), 092401.

[83] K. B. Hathaway, B. Heinrich, and J. A. C. Bland, Springer, 1994.

[84] H. Haus, Prentice-Hall, 1984.

[85] O. Hellwig, A. Berger, and E. Fullerton, J. Magn. Magn. Mater. **290-291** (2004), 1–7.

[86] O. Hellwig, A. Berger, J. Kortright, and E. Fullerton, J. Magn. Magn. Mater. **319** (2007).

[87] J. Herault, C. Papusoi, G. Prenat, B. Dieny, and R. Sousa, Int. J. of Nanotech. (2010).

[88] R. Hertel, S. Gliga, M. Fähnle, and C. Schneider, Phys. Rev. Lett. **98** (2007), 117201.

[89] D. Hilton, R. Averitt, C. Meserole, G. Fisher, D. Funk, J. Thompson, and A. Taylor, Opt. Lett. **29** (2004), 1805.

[90] A. Holz and A. Hubert, Z. angew. Phys. **26** (1969), 145.

[91] A. Hubert and R. Schafer, Springer, 1998.

[92] W. Hübner and G. P. Zhang, Phys. Rev. B **58** (1998), R5920.

[93] A. Itoh and A. Tsukamoto, Presented at the International workshop on Laser-induced magnetization dynamics in nanostructures, 2010.

[94] J. Jackson, Wiley, 1962.

[95] W. Jellinghaus, Z. Tech. Phys. **17** (1939), 33.

[96] S. Jeong, M.E. McHenry, and D.E. Laughlin, IEEE Trans. Magn. **37** (2001), 1309.

[97] G. Ju, J. Hohlfeld, B. Bergman, R. J. M. van de Veerdonk, O. N. Mryasov, J.-Y. Kim, X. Wu, D. Weller, and B. Koopmans, Phys. Rev. Lett. **93** (2004), 197403.

[98] G. Ju, A. V. Nurmikko, R. F. Farrow, R. F. Marks, M. J. Carey, and B. A. Gurney, Phys. Rev. B **58** (1998), R11857.

[99] A. Kabychenkov, Zh. Eksp. Teor. Fiz. **100** (1991), 1219.

[100] S. Kaka and S. Russek, Appl. Phys. Lett. **80** (2002), 2958.

[101] V. Kambersky, Czech J. Phys. B **26** (1976), 1366.

[102] E. Karimi, *Spin Angular Momentum of Light, year = 2014, url = http://en.wikipedia.org/wiki/spinangularmomentumoflight/media/file:samu1.png, urldate = 2014-01-03.*

[103] J. Katine, F. Albert, R. Buhrman, E. Myers, and D. Ralph, Phys. Rev. Lett. **84** (2000), 3149.

[104] N. Kazantseva, U. Nowak, R. W. Chantrell, J. Hohlfeld, and A. Rebei, Euro. Phys. Lett. **81** (2008), 27004.

[105] A. Kimel, A. Kirilyuk, A. Tsvetkov, R. V. Pisarev, and Th. Rasing, Nature **429** (2004), 850.

[106] A. Kimel, A. Kirilyuk, P. Usachev, R. Pisarev, A. Balbashov, and T. Rasing, Nature **435** (2005), 655.

[107] M. Kirchner, A. Hankla, and C. Wood, Photonics Spectra **47** (2013), 48–51.

[108] A. Kirilyuk, A. Kimel, and T. Rasing, Phil. Trans. R. Soc. A **369** (2011), 3631–3645.

[109] A. Kirilyuk, A. V. Kimel, and T. Rasing, Rev. Mod. Phys. **82** (2010), 2731.

[110] C. Kittel, Wiley Interscience Publication, 1996.

[111] W. C. Koehler, J. Appl. Phys. **36** (1965), 1078.

[112] W. Kohn and L. Sham, Phys. Rev. **140** (1965), A1133.

[113] B. Koopmans, H. Kicken, M. van Kampen, and W. J. M. de Jonge, J. Magn. Magn. Mater. **286** (2005), 271.

[114] B. Koopmans, G. Malinowski, F. Dalla Longa, D. Steiauf, M. Fähnle, T. Roth, M. Cinchetti, and M. Aeschlimann, Nat. Mat. **9** (2010), 259–165.

[115] B. Koopmans, J. J. Ruigrok, F. D. Longa, and W. J. de Jonge, Phys. Rev. Lett. **95** (2005), 267207.

[116] B. Koopmans, M. van Kampen, J. Kohlhepp, and W. de Jonge, Phys. Rev. Lett. **85** (2000), 844.

[117] T. Kraft, P. M. Oppeneer, V. N. Antonov, and H. Eschrig, Phys. Rev. B **52** (1995), 3561.

[118] V. Kruglyak, R. Hicken, M. Ali M, B. Hickey, A. Pym, and B. Tanner, Phys. Rev. B **71** (2005), 233104.

[119] M. Kryder, E. Gage, T. McDaniel, W. Challener, E. Rottmayer, J. Ganping, Y. Hsia, and M. Erden, IEEE Trans. Magn. **96** (2008), 1810 – 1835.

[120] C-H. Lambert, S. Mangin, B. S. Varaprasad, Y. K. Takahashi, M. Hehn, M. Cinchetti, G. Malinowski, K. Hono, Y. Fainman, M. Aeschlimann, and E. E. Fullerton, Science **345** (2014), no. 6202, 1337–1340.

[121] C.-H. Lambert, A. Rajanikanth, T. Hauet, S. Mangin, E. Fullerton, and S. Andrieu, Appl. Phys. Lett. **102** (2013), 122410.

[122] M. Lax, W. Louisell, and W. McKnight, Phys. Rev. A **11** (1975), 1365.

[123] D. Lebeugle, D. Colson, A. Forget, M. Viret, A. M. Bataille, and A. Gukasov, Phys. Rev. Lett. **100** (2008), 22.

[124] S. Lee, W. Ratcliff, II, S-W. Cheong, and V. Kiryukhin, Appl. Phys. Lett. **92** (2008), 19.

[125] Z. Li and S. Zhang, Phys. Rev. B **69** (2004), 134416.

[126] X.-X. Lia, J. Baob, L.-Y. Lub, X.-G. Xub, and Y. Jiang, Solid State Communications **148** (2008), 209–212.

[127] F. Dalla Longa, J. T. Kohlhepp, W. J. de Jonge, and B. Koopmans, Phys. Rev. B **75** (2007), 224431.

[128] T Lottermoser, T Lonkai, U Amann, D Hohlwein, J Ihringer, and M Fiebig, Nature **430** (2004), 6999.

[129] Y. Luo, M. Moske, and K. Samwer, Europhys. Lett. **42** (1998), no. 5, 565–570.

[130] P. Maine, D. Strickland P. Bado, M. Pessot, and G. Mourou, IEEE Journal of Quantum Electronics **24** (1988), 398.

[131] G. Malinowski, L. Dalla, R. Francesco, J. Rietjens, P. Paluskar, R. Huijink, H. Swagten, and B. Koopmans, Nature Physics **4** (2008), no. 11, 855–858.

[132] S. Mangin, C. Bellouard, S. Andrieu, F. Montaigne, P. Ohresser, N. Brookes, and B. Barbara, Phys. Rev. B **70** (2004), 014401.

[133] S. Mangin, M. Gottwald, C-H. Lambert, D. Steil, V. Uhlir, L. Pang, M. Hehn, S. Alebrand M. Cinchetti, G. Malinowski, Y. Fainman, M. Aeschlimann, and E. E. Fullerton, Nat. Mat. **13** (2014), 286–292.

[134] S. Mangin, D. Ravelosona, J.A. Katine, M.J. Carey, B.D. Terris, and E.E. Fullerton, Nature Mater. **5** (2006).

[135] S. O. Mariager, F. Pressacco, G. Ingold, A. Caviezel, E. Mohr-Vorobeva, P. Beaud, S. L. Johnson, C. J. Milne, E. Mancini, S. Moyerman, E. E. Fullerton, R. Feidenhansel, C. H. Back, and C. Quitmann, Phys. Rev. Lett. **108** (2012), 087201.

[136] S. Mathias, L. Chan, P. Grychtol, P. Granitzka, E. Turgut, J. Shaw, R. Adam, H. Nembach, M. Siemens, and S. Eich, Proc. of the Nat. Acad. of Sciences **109** (2012), no. 13, 4792–4797.

[137] R. Medapalli, I. Razdolski, M. Savoini, A. Khorsand A. Kalashnikova, A. Tsukamoto, A. Itoh, A. Kirilyuk, A. Kimel, and T. Rasing, Euro. Phys. J. B **86** (2013), no. 4, 1–4.

[138] R. Medapalli, I. Razdolski, M. Savoini, A. Khorsand A. Kirilyuk, A. Kimel, T. Rasing, A. Kalashnikova, A. Tsukamoto, and A. Itoh, Phys. Rev. B **86** (2012), 054442.

[139] J. Mentink, J. Hellsvik, D. Afanasiev, B. Ivanov, A. Kirilyuk, A. Kimel, O. Eriksson, M. Katsnelson, and T. Rasing, Phys. Rev. Lett. **108** (2012), 057202.

[140] S. Middelhoek, J. Appl. Phys. **34** (1963), 1054.

[141] K. Miura, K. Hirao, and Y. Shimotsuma, Abbass Hashim, 2011.

[142] P. Mohn, Springer, 2003.

[143] A. Moser, K. Takano, D. Margulies, M. Albrecht, Y. Sonobe, Y. Ikeda, S. Sun, and E. E. Fullerton, J. Phys. D.: Appl. Phys. **35** (2002), 19.

[144] E. Myers, D. Ralph, J. Katine, R. Louie, and R. Buhrman, Science **285** (1999), 5429.

[145] V. M. Naik, S. Hameed, R. Naik, L. Pust, L. E. Wenger, G. L. Dunifer, and G. W. Auner, J. Appl. Phys. **84** (1998), 3273.

[146] N. Nakajima, T. Koide, T. Shidara, H. Miyauchi, H. Fukutani, A. Fujimori, K. Iio, T. Katayama, M. Nývlt, and Y. Suzuki, Phys. Rev. Lett. **81** (1998), 5229–5232.

[147] U. Nowak, O. Mryasov, R. Wieser, K. Guslienko, and R. Chantrell, Phys. Rev. B **72** (2005), 172410.

[148] L. Néel, J. Phys. Rad. **15** (1954), 376.

[149] H. Ohno, , D. Chiba, F. Matsukura, T. Omiya, E. Abe, T. Dietl, Y. Ohno, and K. Ohtani, Nature **408** (2000), 6815.

[150] H. Ohno, D. Chiba, F. Matsukura, T. Omiya, E. Abe, T. Dietl, Y. Ohno, and K. Ohtani, Nature **408** (2000), no. 6815, 944–946.

[151] T. A. Ostler, R. F. L. Evans, R. W. Chantrell, U. Atxitia, O. Chubykalo-Fesenko, I. Radu, R. Abrudan, F. Radu, A. Tsukamoto, A. Itoh, A. Kirilyuk, T. Rasing, and A. Kimel, Phys. Rev. B **84** (2011), 024407.

[152] T.A. Ostler, J. Barker, R.F.L. Evans, R.W. Chantrell, u. Atxitia, o. Chubykalo-Fesenko, El Moussaoui, L. Le Guyader, E. Mengotti, L.J. Heyderman, F. Nolting, A. Tsukamoto, A. Itoh, D. Afanasiev, B.A. Ivanov, A.m. Kalashnikova, K. Vahaplar, J. mentink, A. Kirilyuk, Th. Rasing, and A. Kimel, Nat. Comm. **3** (2012), 666.

[153] J. Bland M. Padgett, R. Butcher, and N. Bett, J. of Phys. E: Scientific Instruments **22** (1989), no. 5, 308.

[154] M. Padgett, PRSA **470** (2014), 2172.

[155] S. Parkin, Phys. Rev. Lett. **67** (1991), no. 25, 3598.

[156] P. Pershan, Phys. Rev. **130** (1963), 919.

[157] P. Pershan, J. van der Ziel, and L. Malmstrom, Phys. Rev. **143** (1966), 574.

[158] A. Perumal, Y.K. Takahashi, and K. Hono, Appl. Phys. Exp. **1** (2008), 101301.

[159] H. Petek and S. Ogawa, Prog. Surf. Sci. **56** (1997), 239.

[160] L. Pitaevskii, Sov. Phys. JETP **12** (1961), 1008.

[161] C.L. Platt, K.W. Wierman, E.B. Svedberg, R. Veerdonk, J.K. Howard, A.G. Roy, and D.E. Laughlin, J. Appl. Phys. **92** (2002), 6104.

[162] J. Poynting, Proc. Roy. Soc. London Ser. A **82** (1909), 560–567.

[163] Z. Qian and G. Vignale, Phys. Rev. Lett. **88** (2002), 056404.

[164] Z. Qiu and S. Bader, J. Magn. Magn. Mater. **200** (1999), 664.

[165] I. Radu, K. Vahaplar, C. Stamm, T. Kachel, N. Pontius, H. A. Durr, T. A. Ostler, J. Barker, R. F. L. Evans, R. W. Chantrell, A. Tsukamoto, A. Itoh, A. Kirilyuk, Th. Rasing, and A. V. Kimel, Nature **472** (2011), 205.

[166] I. Radu, G. Woltersdorf, M. Kiessling, A. Melnikov, U. Bovensiepen, J.-U. Theile, and C. H. Back, Phys. Rev. Lett. **102** (2009), 117201.

[167] D. C. Ralph and M. D. Stiles, J. Magn. Magn. Mater. **320** (2008), 7.

[168] D.C. Ralph and M.D. Stiles, J. Magn. Magn. Mater. **320** (2007).

[169] H. Richter, A. Lyberatos, U. Nowak, R. Evans, and R. Chantrell, J. Appl. Phys. **111** (2012), no. 3, 033909.

[170] M. A. Ruderman and C. Kittel, Phys. Rev. **96** (1954), 99.

[171] D. Rudolf, L. Chan, M. Battiato, R. Adam, J. Shaw, E. Turgut, P. Maldonado, S. Mathias, P. Grychtol, and H. Nembach, Nature Communications **3** (2012), 1037.

[172] C. Rullière, Springer, 1998.

[173] S. Sahoo, S. Polisetty, C.-G. Duan, S. Jaswal, E. Tsymbal, and C. Binek, Phys. Rev. B **76** (2007), 9.

[174] A. Khorsand M. Savoini, A. Kirilyuk, A. Kimel, A. Tsukamoto, A. Itoh, and T. Rasing, Phys. Rev. Lett. **110** (2013), 107205.

[175] A.R. Khorsand M. Savoini, A. Kirilyuk, A.V. Kimel, A. Tsukamoto, A. Itoh, and T. Rasing, Phys. Rev. Lett. **108** (2012), 127205.

[176] M. Savoini, R. Medapalli, B. Koene, A. Khorsand L. Le Guyader, L. Duo, M. Finazzi, A. Tsukamoto, A. Itoh, and F. Nolting, Phys. Rev. B **86** (2012), no. 14, 140404.

[177] G. Schiitz, R. Wienke, W. Wilhelm, W. B. Zeper, H. Ebert, and K. Sporl, J. Appl. Phys. **67** (1990), 4456.

[178] H. Schumacher, C. Chappert, P. Crozat, R. Sousa, P. Freitas, J. Miltat, J. Fassbender, and B. Hillebrands, Phys. Rev. Lett. **88** (2002), 227201.

[179] E. Simánek and B Heinrich, Phys. Rev. B **67** (2003), 144418.

[180] R. Skomski, Oxford University Press, 2008.

[181] B. Skubic, J. Hellsvik, L. Nordstrom, and O. Eriksson, J. Phys. : Condens. Matter. **20** (2008), 315203.

[182] J. Slonczewski, J. Magn. Magn. Mater. **159** (1996), 1–2.

[183] J. C. Slonczewski, J. Magn. Magn. Mater. **247** (2002), 2341.

[184] D2-Inline Solutions.

[185] N. Spaldin and M. Fiebig, Science **309** (2005), 5733.

[186] C. D. Stanciu, F. Hansteen, A. V. Kimel, A. Kirilyuk, A. Tsukamoto, A. Itoh, and Th. Rasing, Phys. Rev. Lett. **99** (2007), 047601.

[187] C. D. Stanciu, A. V. Kimel, F. Hansteen, A. Kirilyuk, A. Tsukamoto, A. Itoh, and Th. Rasing, Phys. Rev. B **73** (2006), 220402.

[188] C.D. Stanciu, F. Hansteen, A.V. Kimel, A. Kirilyuk, A. Tsukamoto, A. Itoh, and T. Rasing, Phys. Rev. Lett. **99** (2007).

[189] D. Steiauf and M. Fähnle, Phys. Rev. B **79** (2009), 140401.

[190] D. Steil, S. Alebrand A. Hassdenteufel, M. Cinchetti, and M. Aeschlimann, Phys. Rev. B **84** (2011), 224408.

[191] M. D. Stiles, B. Heinrich, and J. A. C. Bland, Springer, 2005.

[192] B. Stipe, T. Strand C. Poon, H. Balamane, T. Boone, J. Katine, J.-L. Li, V. Rawat, H. Nemoto, A. Hirotsune, O. Hellwig, R. Ruiz, E. Dobisz, D. Kercher, N. Robertson, T. Albrecht, and B. Terris, Nat. Phot. **4** (2010), 484–488.

[193] J. Stöhr and H. C. Siegmann, Springer, 2005.

[194] H. Tanaka, S. Takayama, and T. Fujiwara, Phys. Rev. B **46** (1992), 7390.

[195] J.-U. Thiele, M. Buess, and C. H. Back, Appl. Phys. Lett. **85** (2004), 2857.

[196] T. Trunk, M. Redjdal, A. Kakay, M. F. Ruane, and F. B. Humphrey, J. Appl. Phys. **89** (2001), 7606.

[197] S. Tsunashima, Journal. of Phys. D: Appl. Phys. **34** (2001), R87.

[198] S. Tsunashima, S. Masui, T. Kobayashi, and S. Uchiyama, J. Appl. Phys. **53** (1982), 8175.

[199] I. Tudosa, C. Stamm, A. Kashuba, F. King, H. Siegmann, J. Stöhr, G. Ju, B. Lu, and D. Weller, Nature **428** (2004), no. 6985, 831–833.

[200] E. Turgut and P. Grychtol, Phys. Rev. X **3** (2013), no. 3, 39901.

[201] E. Turgut, J. Shaw, P. Grychtol, H. Nembach, D. Rudolf, R. Adam, M. Aeschlimann, C. Schneider, T. Silva, and M. Murnane, Phys. Rev. Lett. **110** (2013), no. 19, 197201.

[202] S. Uchiyama, Mat. Chem. and Phys. **42** (1995), 38–44.

[203] B. Ujfalussy, L. Szunyogh, P. Bruno, and P. Weinberger, Phys. Rev. Lett. **77** (1996), no. 9, 1805.

[204] S. Urazhdin, N. Birge, W. Pratt, and J. Bass, Phys. Rev. Lett. **91** (2003), 146803.

[205] `https://laser.gist.ac.kr/board/bbs/board.php?bo_table=rese_01`, Extracted in February 2014.

[206] `https://www.uni-ulm.de`, Extracted in February 2015.

[207] K. Vahaplar, A. M. Kalashnikova, A. V. Kimel, S. Gerlach, D. Hinzke, U. Nowak, R. Chantrell, A. Tsukamoto, A. Itoh, A. Kirilyuk, and Th. Rasing, Phys. Rev. B **85** (2012), 104402.

[208] K. Vahaplar, A. M. Kalashnikova, A. V. Kimel, D. Hinzke, U. Nowak, R. Chantrell, A. Tsukamoto, A. Itoh, A. Kirilyuk, and T. Rasing, Phys. Rev. Lett. **103** (2009), 117201.

[209] M. van Kampen, C. Jozsa, J. T. Kohlhepp, P. LeClair, L.Lagae, W. J. M. de Jonge, and B. Koopmans, Phys. Rev. Lett. **88** (2002), 227201.

[210] H.W. van Kesteren and W.B. Zeper, J. Magn. Magn. Mater. **120** (1993), 271–273.

[211] B. Varaprasad, M. Chen, Y. K. Takahashi, and K. Hono, IEEE Trans. Magn. **49** (2013), 718–722.

[212] B. S. D. Ch. S. Varaprasad, Y. K. Takahashi, and K. Hono, JOM (2013), 853–861.

[213] J. Versluis, A. V. Kimel, V. N. Gridnev, D. R. Yakovlev, G. Karczewski, T. Wojtowicz, J. Kossut, A. Kirilyuk, and Th. Rasing, Phys. Rev. B **80** (2009), 235326.

[214] G. Vignale and W. Kohn, Phys. Rev. Lett. **77** (1996), 2037.

[215] J. Walowski, G. Müller, M. Djordjevic, M. Münzenberg, M. Kläui, C. A. F. Vaz, and J. A. C. Bland, Phys. Rev. Lett. **101** (2008), 237401.

[216] D.-S. Wang, R. Wu, Ruqian, and A. Freeman, Phys. Rev. Lett. **70** (1993), no. 6, 869.

[217] Y. Wu, J. Stöhr, B. Hermsmeier, M. Samant, and D. Weller, Phys. Rev. Lett. **69** (1992), 2307–2310.

[218] Y. Yafet, Academic, 1963.

[219] T. Yoshino, J. Magn. Magn. Mater. **323** (2011), 2531.

[220] G. Zhang, W. Hübner, G. Lefkidis, Y. Bai, and T. George, Nat. Phys. **5** (2009), 499.

[221] H.-L. Zhang, Y.-Z. Wang, and X.-J. Chen, J. Magn. Magn. Mater. **321** (2009), L73.

[222] L. Zhang, Y. K. Takahashi, K. Hono, B. C. Stipe, J. Y. Juang, and M. Grobis, J. Appl. Phys. **109** (2011), 07B703.

[223] L. Zhong, M. Kim, X. Wang, and A. Freeman, Phys. Rev. B **53** (1996), no. 15, 9770.

[224] J.-G. Zhu, X. Zhu, and Y. Tang, IEEE Trans. Magn. **44** (2008), 25.

[225] V. Zhukov and E. V. Chulkov, Phys. Usp. **52** (2009), 105.

[226] A. Zvezdin and V. Kotov, Institute of Physics Publishing, 1997.

Etude du retournement optique dépendant de l'hélicité dans des couches minces magnétiques

Depuis une quinzaine d'années, de nombreuses solutions différentes ont été proposés afin de modifier l'aimantations de matériaux sans aucun champ magnétique extérieur appliqué. La manipulation d'aimantation à moindre coût énergétique, de préférence à des échelles de temps ultracourtes, est devenu un enjeu fondamental avec des implications pour les technologies d'enregistrement magnétique et de nouvelles sortes de stockage. Sur ce chemin, le type d'interaction découverte par *Stanciu et al.* ouvre la voie à l'utilisation de la lumière comme moyen d'exciter et de sonder directement les matériaux magnétiques.

La description des théories et modèles existants dans ce domaine permet de nous rendre attentif sur les différents paramètres impliqués par l'interaction des lasers ultrarapides et matériaux magnétiques. L'entrelacement spécifique des impulsions de chaleur et de moment angulaire propre aux lasers ultrarapides est mise en avant afin de discuter de leur rôle dans les phénomènes observés. Le délai des interactions responsables de l'état final de l'aimantation est abordé et notamment la manière dont celle-ci ont un impact sur la façon dont le système se stabilise après une excitation laser.

En outre, nous nous sommes intéressés à la relation entre les paramètres matériels et l'état final de l'aimantation obtenue avec un laser ultrarapide. Grâce aux nombreuses classes de matériaux magnétiques existantes les paramètres magnétiques peuvent être ajustés dans une grande gamme de valeurs et de manière entièrement contrôlés. Notre installation d'imagerie magnétique est alors capable de sonder les caractéristiques optiques et la stabilité des domaines après l'excitation.

Nous avons finalement démontré que le retournement optique dépendent de l'hélicité peut être observée non seulement dans un grand nombre de couches minces d'alliages de terre rare-métaux de transition (RE-TM) mais aussi dans une variété beaucoup plus large de matériaux, y compris les multicouches et hétérostructures de RE-TM. Nous montrons en outre que les hétérostructures ferrimagnétiques dépourvues de terres rares présentent également un retournement optique. Nous avons en plus développé le contrôle optique de multicouches ferromagnétiques dont des films granulaires actuellement explorés pour l'enregistrement magnétique ultra-haute densité de demain.

Notre découverte montre que la manipulation de l'aimantation dans des matériaux magnétiques est un phénomène beaucoup plus général que précédemment suspecté et peut avoir un impact majeur sur l'enregistrement magnétique et le stockage de l'information grâce à l'intégration nouvelle de ce type de contrôle optique dans des bits ferromagnétiques.

Mots-Clés : Electronique de spin, Transfert de spin, Magnétisme, Retournement Optique

All-Optical Helicity dependent switching effect in magnetic thin films

The possibilities of modifying magnetization without applied magnetic fields have attracted growing attention over the past fifteen years. The low-power manipulation of magnetization, preferably at ultrashort timescales, has become a fundamental challenge with implications for future magnetic information memory and storage technologies. In particular the interplay of laser and magnetism recently discovered by *Stanciu et al.* opens up new way for light to be used as an excitation and a probe of magnetic materials.

A description of the current models and frameworks developed in the field requires a careful look at the different parameters involved through the interaction of ultrafast lasers and magnetic materials. The specific and complex interplay between heat and angular momentum transfer is highlighted in order to discuss the role of each of them in the phenomena observed. The timescales of the different interactions responsible for the final state of magnetization are presented and will impact the way the system recovery after a laser excitation.

Besides we were interested in exploring the relation between the material parameters such as anisotropy, ordering temperature and exchange coupling on the final state of magnetization obtained with a laser. Indeed thanks to the many different magnetism classes existing the magnetic parameters can be tuned widely and in a controlled manner. Our imaging setup then is able to probe the optical characteristics and domain stability after the laser excitation.

We finally demonstrated that all-optical helicity-dependent switching (AO-HDS) can be observed not only in selected rare earth-transition metal (RE-TM) alloy films but also in a much broader variety of materials, including RE-TM alloys, multilayers and heterostructures. We further show that RE-free Co-Ir-based synthetic ferrimagnetic heterostructures designed to mimic the magnetic properties of RE-TM alloys also exhibit AO-HDS. We further developed the optical control of ferromagnetic materials ranging from magnetic thin films to multilayers and even granular films being explored for ultra-high-density magnetic recording.

Our finding shows that optical control of magnetic materials is a much more general phenomenon than previously assumed and may have a major impact on data memory and storage industries through the integration of optical control of ferromagnetic bits.

Keywords : Spintronics, Spin-Transfer, Magnetism, All-Optical Switching